

2

# WICK-TYPE LIQUID-METAL COMBUSTION

## FINAL REPORT

Grant No. 00014-89-J-1188  
(October 15, 1988 to April 14, 1991)

The Department of The Navy  
Office of Naval Research  
800 North Quincy Street  
Arlington, Virginia 22217-5000

By

L.-D. Chen, H. Y. Lyu, and K. Y. Hsu

The University of Iowa  
College of Engineering  
Department of Mechanical Engineering  
Iowa City, Iowa 52242

May 1991

AD-A236 204



91 5 24 044

91-00521



# WICK-TYPE LIQUID-METAL COMBUSTION

## FINAL REPORT

Grant No. 00014-89-J-1188  
(October 15, 1988 to April 14, 1991)

The Department of The Navy  
Office of Naval Research  
800 North Quincy Street  
Arlington, Virginia 22217-5000

By

L.-D. Chen, H. Y. Lyu, and K. Y. Hsu

The University of Iowa  
College of Engineering  
Department of Mechanical Engineering  
Iowa City, Iowa 52242

May 1991



APPROVAL FOR	
DATE	✓
BY	✓
REVIEW	✓
JUSTIFICATION	
Pec A216019	
APPROVED BY	
DATE	
Dist	Special
A-1	

## ABSTRACT

An experimental and theoretical investigation was conducted to study wick combustion of Li and SF<sub>6</sub>. A single-line laser induced fluorescence thermometry with Li<sub>2</sub> as fluorescence species was developed. The calibration experiments yield promising results; refinements, however, are needed before the technique can be applied to combustion flame measurements. Wick combustion of Li and SF<sub>6</sub> was conducted in a vacuum chamber at sub-atmospheric pressures. The combustion results in a bright pinkish flame. The spontaneous emission spectrum is determined for the first time in the literature. The emission spectrum shows that the flame luminosity is dominated by the resonance-emission line of Li atoms. On analysis, a conserved scalar approach was employed to model the wick flame. A single equation was obtained to describe the interface condition of wick combustion. Numerical solutions were obtained for laminar wick diffusion flames. The prediction yields similarity profiles for planar Li-SF<sub>6</sub> wick diffusion flames although non-similar governing equations were retained in the formulation, but similarity solutions are not obtained for cylindrical wick diffusion flames. The cylindrical wick diffusion flames are found to deviate substantially from the planar geometry. The cylindrical wick has a much higher fuel mass burning rate per unit wick surface area as compared to the planar geometry. The flame stand-off distance was found to increase for both planar and cylindrical wicks as the system pressure was reduced. The effects on mass burning rates due to fuel composition variations were studied employing fuel-rich and product-rich liquids at 0.0035 MPa in the analysis. It was found that the product-rich fuel yields a much lower flame temperature; the mass burning rate, however, was higher than the pure lithium at 0.01 MPa. The findings on fuel mass burning rates are interesting. The results suggest that the wick configuration may achieve a higher fuel utilization than the submerged jet, provided that the surface tension of product-rich liquids is sufficient for capillary transport of fuel. Simultaneous spectrum measurements of the wick combustion of Li and SF<sub>6</sub> are obtained using an image intensified CCD camera. Flame temperature is determined from inversion of the radiance intensity registered by the CCD camera. A peak temperature of 3000 to 3500 K is identified. Further work to refine the measurements and to analyze the data is suggested.

## TABLE OF CONTENTS

	<u>Page</u>
ABSTRACT.....	ii
TABLE OF CONTENTS.....	iii
LIST OF TABLES.....	v
LIST OF FIGURES.....	vi
NOMENCLATURE.....	viii
ACKNOWLEDGEMENT.....	xi
I. INTRODUCTION.....	1
1.1 General Statement of the Problem.....	1
1.2 Previous Related Investigations.....	2
1.3 Specific Objectives.....	3
II. THEORETICAL CONSIDERATION.....	4
2.1 Thermodynamic Properties of $\text{Li}_2\text{S}$ .....	4
2.2 Flow Analysis.....	6
2.3 Numerical Methods.....	10
III. EXPERIMENTAL CONSIDERATION.....	11
3.1 Apparatus.....	11
3.2 LIF Thermometry .....	16
3.3 Emission Spectrum and Temperature Measurements .....	22
3.3.1 Scanning Spectrum .....	22
3.3.2 Simultaneous Spectrum .....	22
IV. RESULTS AND DISCUSSION.....	33
4.1 LIF Thermometry .....	33
4.2 Wick Combustion .....	33
4.3 Theoretical Results.....	39

4.4 Emission Spectrum and Temperature Measurements .....	58
V. SUMMARY AND FUTURE WORK .....	68
REFERENCES .....	70

## LIST OF TABLES

<u>Table</u>	<u>Page</u>
1. Coefficient for $\text{Li}_2\text{S}$ Specific Heat Correlations .....	5
2. Fluorescence Lines of $^7\text{Li}_2$ Molecule Excited by Argon Ion Laser (B-X Transitions) .....	17
3. Assignment of $^7\text{Li}_2$ B(2,31) Fluorescence Excited at 488 nm .....	34
4. Assignment of $^7\text{Li}_2$ B(6,45) Fluorescence Excited at 488 nm .....	34

## LIST OF FIGURES

<u>Figure</u>	<u>Page</u>
1. Coordinate System.....	7
2. Schematic of the Vacuum Chamber .....	12
3. Schematic of the Burner Arrangement.....	13
4. Gas Supply .....	14
5. Experimental Set Up for Wick Combustion Diagnostics .....	15
6. LIF Thermometry Calibration Experimental Set-Up.....	17
7. Experimental Set-up for Modulated LIF/Emission Measurements .....	23
8. Experimental Set-up for Simultaneous LIF/Emission Measurements .....	24
9. Synchronization Circuit for LIF/Emission Measurements .....	26
10. Timing Sequence for Laser Firing and Intensifier Gating.....	27
11. Relative System-Spectral-Response for Spectral Range of 400 to 500 nm .....	29
12. Error of Temperature Measurements vs. Intensity Ratio at 460 nm and 497 nm Lines .....	31
13. Schematic for Intensity Inversion .....	32
14. LIF Thermometry Calibration of $^7\text{Li}_2$ ; B (2, 31)-X(5, 30/32)/B(6,45)-X(8,44/46).....	35
15. LIF Thermometry Calibration of $^7\text{Li}_2$ ; B (2, 31)-X(6, 30/32)/B(6,45)-X(8,44/46).....	36
16. Wick Combustion of Li and $\text{SF}_6$ at 0.01 MPa .....	38
17. Spontaneous Emission Spectrum of Wick Combustion of Li and $\text{SF}_6$ at 0.01 MPa .....	40
18. State Relationship (Temperature and Density) of Ethanol-Air Wick Diffusion Flame .....	41
19. State Relationship (Concentration) of Ethanol-Air Wick Diffusion Flame .....	42
20. Predicted $v_w$ and $\dot{m}''$ of Ethanol-Air Wick Diffusion Flames.....	44
21. Predicted Flame Structure of Ethanol-Air Wick Diffusion Flames.....	45
22. State Relationship of Density and Temperature of Li- $\text{SF}_6$ Wick Combustion.....	46
23. State Relationship of Species Concentration of Li- $\text{SF}_6$ Wick Combustion at 0.01 MPa.....	47
24. State Relationship of Species Concentration of Li- $\text{SF}_6$ Wick Combustion at 0.1 MPa.....	48

25. Similarity Mixture Fraction Profiles of Li-SF <sub>6</sub> Wick Combustion.....	50
26. Similarity Velocity Profiles of Li-SF <sub>6</sub> Wick Combustion.....	51
27. Temperature and Velocity Profiles of Li-SF <sub>6</sub> Wick Combustion at $\xi = 0.22$ .....	52
28. Temperature and Velocity Profiles of Li-SF <sub>6</sub> Wick Combustion at $\xi = 1.0$ .....	53
29. Local Wall Blowing Velocity .....	54
30. Local Fuel Mass Burning Rate .....	54
31. State Relationship of Fuel-Rich and Product Rich Fuels.....	56
32. Li-SF <sub>6</sub> Wick Combustion of Fuel-Rich and Product-Rich Fuel at 0.0035 MPa.....	57
33. Spatial Profiles of Integrated Intensities, Event No. 1 .....	59
34. Spatial Profiles of Integrated Intensities, Event No. 2 .....	60
35. Spatial Profiles of Integrated Intensities, Event No. 3 .....	61
36. Spatial Profiles of Integrated Intensities, Event No. 4 .....	62
37. Spatial Profiles of Integrated Intensities, Event No. 5 .....	63
38. Temperature Profile Calculated from Inversed Intensity; Left-Side of the Wick.....	66
39. Temperature Profile Calculated from Inversed Intensity; Right-Side of the Wick.....	67



## NOMENCLATURE

<u>Symbol</u>	<u>Description</u>
$a_i$	correlation coefficients, Eqs. 2-4
A	spontaneous emission rate
c	speed of light
$C_p$	specific heat
D	binary diffusion coefficient
E	energy
f	dimensionless stream function, Eq. 12
F	Boltzmann fraction
g	acceleration of gravity
$g_i$	degeneracy
h	enthalpy
$h_{fg}$	enthalpy of vaporization
H	plate height
k	thermal conductivity
L	enthalpy of gasification
Le	Lewis number
N	number density of photons
Pr	Prandtl number
Q	collisional quenching rate
R	universal gas constant
Sc	Schmidt number
T	temperature
u	streamwise velocity
v	cross-stream velocity

$V$	detected signal
$W$	laser-induced absorption/stimulated emission
$x$	streamwise direction
$y$	cross-stream direction
$Y_i$	mass fraction of species $i$
$Z$	mixture function
$Z_{Tot}$	total partition function
$\beta$	collection efficiency, Eq. 24
$\eta$	similarity variable, Eq. 15
$\kappa$	Boltzmann constant
$\mu$	dynamic viscosity
$\nu$	frequency
$\omega_i$	source/sink term in Species Equation, Eq. 9
$\Omega_c$	solid angle
$\Phi$	fluorescence signal, Eq. 24
$\xi$	similarity variable, Eq. 15
$\rho$	density
$\psi$	stream function, Eq. 14
$\frac{d\sigma}{d\Omega}$	scattering cross-section

### *Subscripts*

1	ground state
2	excited state
c	collective quantity
e	electronic
f	fluorescence

g	gas phase
l	liquid phase
lin	linear fluorescence model
r	rotational
s	solid phase
sat	saturated fluorescence model
v	vibrational
w	wall condition
$\infty$	ambient condition

## ACKNOWLEDGEMENT

This work was supported by the Office of Naval Research under Grant No. 00014-89-J-1188 with Dr. Gabriel D. Roy serving as Scientific Officer. The authors acknowledge technical assistance of Professors W. C. Stwalley and M. Lyyra on  $\text{Li}_2$  LIF thermometry which was conducted at the Center for Laser Science and Engineering at The University of Iowa.

## I. INTRODUCTION

### 1.1 General Statements of the Problem

A novel liquid-metal combustion system involving the reaction of lithium (Li) and sulfur hexafluoride ( $\text{SF}_6$ ) is studied. The system is unique in that it has a high energy density and a high specific energy and that it yields condensed phase products under normal operation conditions. The high energy density and high specific energy satisfy the volume and weight requirements of propulsion applications and the condensed phase product provides a means of closed system operation as desired by deep-sea propulsion vessels; thus the liquid-metal combustion system is ideal for undersea applications.

Two major system configurations have been identified, i.e. the submerged jet and the reactive heat pipe (or wick-type), e.g. see Hughes et al. (1983). The submerged jet was identified as a practical energy source for submersible vehicles (Parnell, 1987 and 1989); however, the material compatibility of lithium and the high temperature and condensed phase products of Li and  $\text{SF}_6$  combustion makes detailed measurements of the flame structure extremely difficult in submerged jet combustors. The wick configuration, on the other hand, provides an optical access to study the combustion of Li and  $\text{SF}_6$ . The wick configuration also has intrinsic merits as an energy source for surface and under-sea propulsion systems.

When a wick was employed, liquid Li was supplied through the wick action and heat transfer was accomplished by evaporation and condensation of lithium (Hughes et al., 1983 and Faeth et al., 1978). The wick system was shown to operate at a lower power level but with a longer time duration compared to submerged jet systems. A submerged jet combustor requires direct injection of gaseous  $\text{SF}_6$  into the liquid bath (Li) at under-expanded conditions. As a result, the injector was in contact with hot combustion products/lithium and the injector clogging and erosion becomes a problem which needs to be addressed. When the injector clogged, the oxidant flow was stopped and the combustion was terminated. Restart of a submerged-jet combustor, unfortunately, is very difficult. The wick combustor, on the other hand, can be designed free from injector clogging.

This was accomplished by confining the high temperature zones to a region away from the injector (Faeth et al., 1978). It was also noted (e.g., see You and Faeth, 1977) that the wick system can be designed to have a fast response to the load change, to be capable of system restart and to have flexible heat exchanger layout through the heat pipe operation.

## 1.2 Previous Related Investigations

A closed volume liquid-metal combustor utilizing Li and SF<sub>6</sub> as fuel and oxidant has been identified as an energy source for undersea propulsion applications. The liquid-metal combustion system is also known as the SCEPS system (Stored Chemical Energy Propulsion Systems), e.g. see Hughes et al. (1983) and can be operated independent of environmental conditions. The reaction of Li and SF<sub>6</sub> follows the stoichiometry:



The combustion products (LiF and Li<sub>2</sub>S) are soluble in liquid lithium, yielding two immiscible liquids: fuel-rich (or metal rich) and product-rich (or salt rich) liquids. The density of the product-rich liquid is heavier than the fuel rich liquid (and lithium as well), allowing for constant volume operations. A closed system operation based on liquid-metal combustion has been developed for undersea propulsion applications (Hughes et al., 1983 and Parnell, 1989).

As discussed earlier, two system configurations were proposed, e.g. see Faeth, et al. (1978) and Hughes, et al. (1983), the submerged jet and wick-type or reactive heat pipe combustors. A number of investigations relevant to the submerged-jet operation had appeared in the literature; for example, see Loth and Faeth (1989) and Parnell (1989) and references cited therein. Much less work, however, was reported for the wick-type liquid-metal combustion, despite the advantages over the submerged jet as an energy source for propulsion applications. The wick-type liquid metal combustion yields a gaseous diffusion flame near the wick surface as identified by Blakeslee

(1977). The reaction products, however, condensed as they convected and diffused to a low temperature region and eventually dissolved in the liquid bath to form two immiscible liquids (fuel-rich and product-rich liquids). A reactive heat pipe concept based on the wick operation was later developed and reported by You, et al. (1977), Alstadt and Faeth (1977), You and Faeth (1977), Faeth, et al. (1978) and Groff and Faeth (1978b). The fundamentals of wick-type liquid-metal combustion are not well understood; for example, the presence of non-condensable gases was found to drastically reduced the fuel mass burning rate (Blakeslee, 1977). The mechanism, however, was not understood. A better understanding of the mechanism can provide design guidance to reduce the non-condensable gas effects and provide guidance in system preparation.

### 1.3 Specific Objectives

As discussed, the wick-type liquid metal combustion has intrinsic merits as an energy source for surface and under-sea propulsion systems and the wick configuration can provide an optical access to study combustion of Li and SF<sub>6</sub>. The specific objectives of this project are: (1) to document the flame structure of wick-type Li and SF<sub>6</sub> combustion, (2) to obtain a better understanding of wick-type liquid-metal combustion, for example on the effects of fuel compositions on mass burning rates and (3) to develop prediction methods for wick combustion and to assess model predictability.

## II. THEORETICAL CONSIDERATION

The basic phenomena of liquid-metal combustion were discussed in earlier studies; for example, the flowfield of submerged gaseous oxidant jets in liquid metal was discussed by Avery and Faeth (1975), Chen and Faeth (1983) and Loth and Faeth (1989) and the wick-type liquid-metal combustion was studied by Blakeslee (1977) and Faeth, et al. (1978). The combustion of a wick flame was found essentially a gaseous diffusion flame (Blakeslee, 1977) in which the fuel consumption rate was limited by the transport in the gas phase. To model the wick combustion of Li and SF<sub>6</sub>, thermochemical properties of reactants and products were identified and the transport process was modeled.

### 2.1 Thermodynamic Properties of Li<sub>2</sub>S

Thermochemical properties of reactants and products involved in Li-SF<sub>6</sub> combustion are generally available from JANAF Tables (Chase et al., 1985), except for Li<sub>2</sub>S which were taken from Groff (1976). This was done by curve fitting Li<sub>2</sub>S data reported by Groff (1976) to the format employed by the NASA code. The gas phase property was estimated from statistical thermodynamics based on spectroscopic data. Li<sub>2</sub>S was assumed a simple harmonic oscillator and the frequency was estimated from similar molecules; in specific, H<sub>2</sub>N, H<sub>2</sub>O, H<sub>2</sub>S, and Li<sub>2</sub>O. The liquid and solid state properties were estimated from the properties of Na<sub>2</sub>S, Li<sub>2</sub>O, and Na<sub>2</sub>O. Groff (1976) should be consulted in estimating Li<sub>2</sub>S properties. To utilize the NASA equilibrium program (CEC), we need to provide specific heat, enthalpy and entropy of Li<sub>2</sub>S for inclusion in the data bank. This was done by curve fitting the Li<sub>2</sub>S data of Groff (1976) to the format employed in the NASA code.

The specific heat correlations used in the NASA Code (CEC Program; Gordon and McBride, 1976) assumed the following form:

$$\frac{C_p}{R} = a_1 + a_2 T + a_3 T^2 + a_4 T^3 + a_5 T^4 \quad (2)$$



The coefficients  $a_1$ ,  $a_2$ ,  $a_3$ ,  $a_4$  and  $a_5$  were obtained by curve-fitting the specific heat data reported by Groff (1976). A least squares fit of fifteen temperatures, i.e., 300 K to 1600 K at 100 K increments and at the  $\text{Li}_2\text{S}$  normal melting point (1645 K), was made for solid phase specific heats, and 25 temperatures (1645 K and 1700 to 4000 K at 100 K increment) and 41 temperatures (1000 to 5000 K at 100 K increment) were used for the liquid-phase and gas-phase specific heats, respectively. The obtained correlation coefficients are summarized in Table 1.

Table 1. Coefficient for  $\text{Li}_2\text{S}$  Specific Heat Correlations

<u>Coefficients</u>	<u>Solid</u>	<u>Liquid</u>	<u>Gas</u>
$a_1$	0.56732404E+01	0.96966147E+01	0.70533838E+01
$a_2$	0.11686870E-01	0.11409415E-02	0.50293408E-03
$a_3$	-0.19245575E-04	-0.56692271E-06	-0.22771507E-06
$a_4$	0.16212627E-07	0.12559047E-09	0.46648819E-10
$a_5$	-0.47654715E-11	-0.10217635E-13	-0.35727596E-14
$a_6$	-0.61355396E+05	-0.57484191E+05	-0.23660173E+05
$a_7$	-0.26409861E+02	-0.44900746E+02	-0.11219699E+02

Two additional coefficients,  $a_6$  and  $a_7$ , are also summarized in Table 1 which were used in the enthalpy and entropy correlations:

$$\frac{H}{RT} = a_1 + \frac{a_2}{2} T + \frac{a_3}{3} T^2 + \frac{a_4}{4} T^3 + \frac{a_5}{5} T^4 + \frac{a_6}{T} \quad (3)$$

$$\frac{S}{R} = a_1 \ln T + a_2 T + \frac{a_3}{2} T^2 + \frac{a_4}{3} T^3 + \frac{a_5}{4} T^4 + a_7 \quad (4)$$

The two coefficients,  $a_6$  and  $a_7$ , were determined from the enthalpy integration ( $a_6$ ) and from

Clausius-Claperyon equation (a7). In arriving at the above values, the gas-phase enthalpy of formation was determined, from statistical mechanics, -178.06 kJ/mole at 298.15 K and 0.1 MPa. The liquid-phase enthalpy of formation was accordingly determined -451.55 kJ/mole at 298.15 K. The solid-phase enthalpy of formation was determined -492.91 kJ/mole at 298.15 K, based on heat of fusion 49.4 kJ/mole and liquid-phase enthalpy -337.78 kJ/mole at the normal melting point.

## 2.2 Flow Analysis

The wick flame was assumed a diffusion flame with infinitely fast reactions and boundary-layer approximations were invoked. The major assumptions are

- Steady-state two-dimensional boundary layer flow.
- Chapman gas, unity Lewis number, constant Prandtl number and binary diffusion system.
- No radiative heat loss and negligible viscous dissipation.
- Infinitely fast chemical reactions and local equilibrium established in the flow
- Uniform interface condition.

Based on the above assumptions, a conserved scalar approach can be applied (Williams, 1985).

The governing equations of conservation of mass, momentum, energy and species are

### *Continuity*

$$\frac{\partial(\rho u)}{\partial x} + \frac{\partial(\rho v)}{\partial y} = 0 \quad (5)$$

### *Momentum*

$$\rho u \frac{\partial u}{\partial x} + \rho v \frac{\partial u}{\partial y} = \frac{\partial}{\partial y} \left( \mu \frac{\partial u}{\partial y} \right) + g (\rho_{\infty} - \rho) \quad (6)$$

### *Mixture Fraction*

$$\rho u \frac{\partial Z}{\partial x} + \rho v \frac{\partial Z}{\partial y} = \frac{\partial}{\partial y} \left( \rho D \frac{\partial Z}{\partial y} \right) \quad (7)$$

where the coordinate system is summarized in Fig. 1 and the mixture fraction,  $Z$ , is a Shvab-Zeldovich variable, combining the energy and species equations. The energy and species equations are

*Energy*

$$\rho u \frac{\partial h}{\partial x} + \rho v \frac{\partial h}{\partial y} = \frac{\partial}{\partial y} \left( \frac{k}{C_p} \frac{\partial h}{\partial y} \right) \quad (8)$$

*Species*

$$\rho u \frac{\partial Y_i}{\partial x} + \rho v \frac{\partial Y_i}{\partial y} = \frac{\partial}{\partial y} \left( \rho D \frac{\partial Y_i}{\partial y} \right) + \omega_i \quad (9)$$

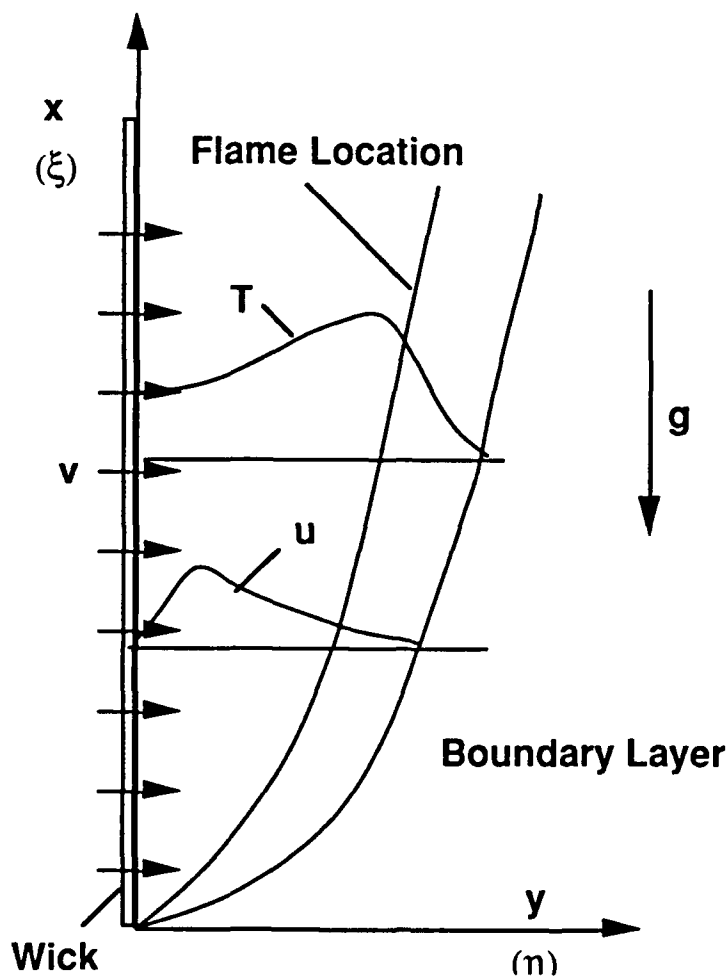


Figure 1. Coordinate System

where  $h$  is the total enthalpy, including enthalpy of formation, and  $Y_i$  is the mass fraction of species  $i$  and  $\omega_i$  is the source/sink term due to chemical reactions. The governing equations were further cast into a dimensionless form in terms of stream function and similarity variables (Chen and Faeth, 1982). The transformed equations are

#### Momentum

$$\frac{\partial}{\partial \eta} \left( \frac{\rho}{\rho_\infty} \frac{\mu}{\mu_\infty} f'' \right) + 3 f f'' - 2 (f')^2 + \frac{\rho_\infty/\rho - 1}{\rho_\infty/\rho_w - 1} = 4 \xi \left( f' \frac{\partial f'}{\partial \xi} - \frac{\partial f}{\partial \xi} f'' \right) \quad (10)$$

#### Mixture Fraction

$$\frac{\partial}{\partial \eta} \left( \frac{\rho}{\rho_\infty} \frac{\mu}{\mu_\infty} \frac{1}{Pr} \frac{\partial Z}{\partial \eta} \right) + 3 f \frac{\partial Z}{\partial \eta} = 4 \xi \left( f \frac{\partial Z}{\partial \xi} - \frac{\partial f}{\partial \xi} \frac{\partial Z}{\partial \eta} \right) \quad (11)$$

The continuity is automatically satisfied in the stream function formulation. The momentum equation employs a dimensionless stream function:

$$f(\xi, \eta) = \frac{\psi}{4 v_\infty c (\xi H)^{1/4}} \quad (12)$$

where

$$c = \left[ \frac{g (\rho_\infty/\rho_w - 1)}{4 v_\infty^2} \right]^{1/4} \quad (13)$$

and the dimensional stream function  $\psi$  was defined as

$$\frac{\partial \psi}{\partial y} = \frac{\rho u}{\rho_\infty}, \quad \frac{\partial \psi}{\partial x} = - \frac{\rho v}{\rho_\infty} \quad (14)$$

The similarity variables are defined in the following

$$\xi = \frac{x}{H}, \quad \eta = cx^{-1/4} \int_0^y \left( \frac{\rho}{\rho_\infty} \right) dy; \quad (15)$$

The boundary conditions were specified to satisfy the non-slip wall and quiescent ambient conditions:

$$\eta = 0; \quad f = f_w, \quad f' = 0, \quad Z = 1, \quad \text{and}$$

$$\eta = \infty; \quad f' = 0, \quad Z = 0. \quad (16)$$

To describe the interface thermodynamic state, a single equation was obtained for  $Z = 1$ . The equation is shown below

$$Y_{F,w} = 1 + \frac{1}{Le} \frac{L}{Cp_w} \frac{\left( \frac{\partial Y_F}{\partial Z} \right)_w}{\left( \frac{\partial T}{\partial Z} \right)_w} \quad (17)$$

where  $Le$ ,  $L$  and  $Cp_w$  are respectively the Lewis number, enthalpy of gasification and specific heat at the interface. Equation (17) was obtained considering the conservation of mass and energy at the interface, i.e.

*Mass*

$$\rho_w v_w (1 - Y_{F,w}) = - \rho D \left( \frac{\partial Y_F}{\partial y} \right)_w \quad (18)$$

*Energy*

$$\rho_w v_w L = k \left( \frac{\partial T}{\partial y} \right)_w \quad (19)$$

The significance of Eq. (17) is that the interface condition is dictated by the flame structure within the context of the conserved scalar approach. Eq. (17) yields an interface fuel mass fraction is less than one under normal condition. This can be seen as the fuel vapor decreases and the temperature increases as  $Z$  is decreased (or moving away from the interface). It is noted that the interface fuel vapor mass fraction may approach unity near the mixture thermodynamic critical point at that condition the interface fuel mass fraction is equal to one. An interface analysis is established which allows for polymerization of fuel and products and the presence of condensed phase products at the interface. The analysis has been detailed by Lyu (1991) and to a lesser degree by Lyu et al. (1991).

### 2.3 Numerical Methods

As stated earlier, local equilibrium was assumed for the flow. The state relationship was constructed from the equilibrium calculation. The equilibrium calculation employed the NASA equilibrium code, i.e. NASA CEC Program by Gordon and McBride (1976). The CEC program utilized a Newton-Raphson iterative scheme in minimizing the Gibbs free energy to obtain equilibrium species and temperature.

The flow calculation employed a finite difference scheme (Keller box method) to obtain numerical solutions to the governing equations, Eqs. 10 and 11, at specified boundary and interface conditions, Eqs. 16 and 17. The numerical code was modified, allowing for wall blowing effects, from the computer program developed by Chen and Faeth (1982). The modified program was tested satisfactory for non-reactive flows (i.e., evaporative cooling) before adopting it for reactive flow computations.

### III. EXPERIMENTAL CONSIDERATION

#### 3.1 Apparatus

It is known that Li-SF<sub>6</sub> liquid-metal combustors were operated at sub-atmospheric pressures. Experiments were conducted in the vacuum chamber shown in Fig. 2 which was modified from a commercial product Vacuum/Atmospheres Model HE-133-5. The chamber was constructed with corrosion-resistant aluminum alloy (Type 6061), having an interior volume 0.43 m<sup>3</sup> (30" I.D. x 36" long) and equipped with an ante-chamber (0.044 m<sup>3</sup>; 12" I.D. x 24" long).

The chamber interior design was illustrated in Fig. 3 in which a wick burner was placed inside. A stainless steel wick burner (316 Stainless Steel and 100x100 mesh) was placed inside the chamber. Different burner diameters (32 mm for Li-SF<sub>6</sub> and 25 mm for other experiments) and burner heights (25 to 89 mm) were used in the experiments. The wick screen was spot-welded on two stainless steel caps. An ANSI K-type (chromel-alumel) sheathed (stainless steel sheath) thermocouple was used to monitor the liquid bath temperature and a thermocouple indicator (Omega DP-80) was used for temperature readout. The thermocouple output was also interfaced with a Mac IIx work station using an A/D converter (National Instrument MIO-16-9). A stainless steel plate was placed above the burner to quench the hot plume rising from the wick burner. A well insulated (Cole Palmer N-03116-40) brass heater block (25 mm in diameter and 60 mm long) heated by nichrome wires (AWG Gauge 20) was placed below the wick burner and the heating was controlled by a Variac (Fisher Model 09-521-22) and monitored by a Watt meter (Ohio Samitronics EM-5). It required 150 W to heat the lithium inside the wick burner to a molten state (around 400 °C) prior to combustion experiments. Coiled nichrome wires (AWG Gauge 20) with a small lithium solid were used as the ignitor. The ignitor wire was heated by a Variac (Research LabVac 30-12).

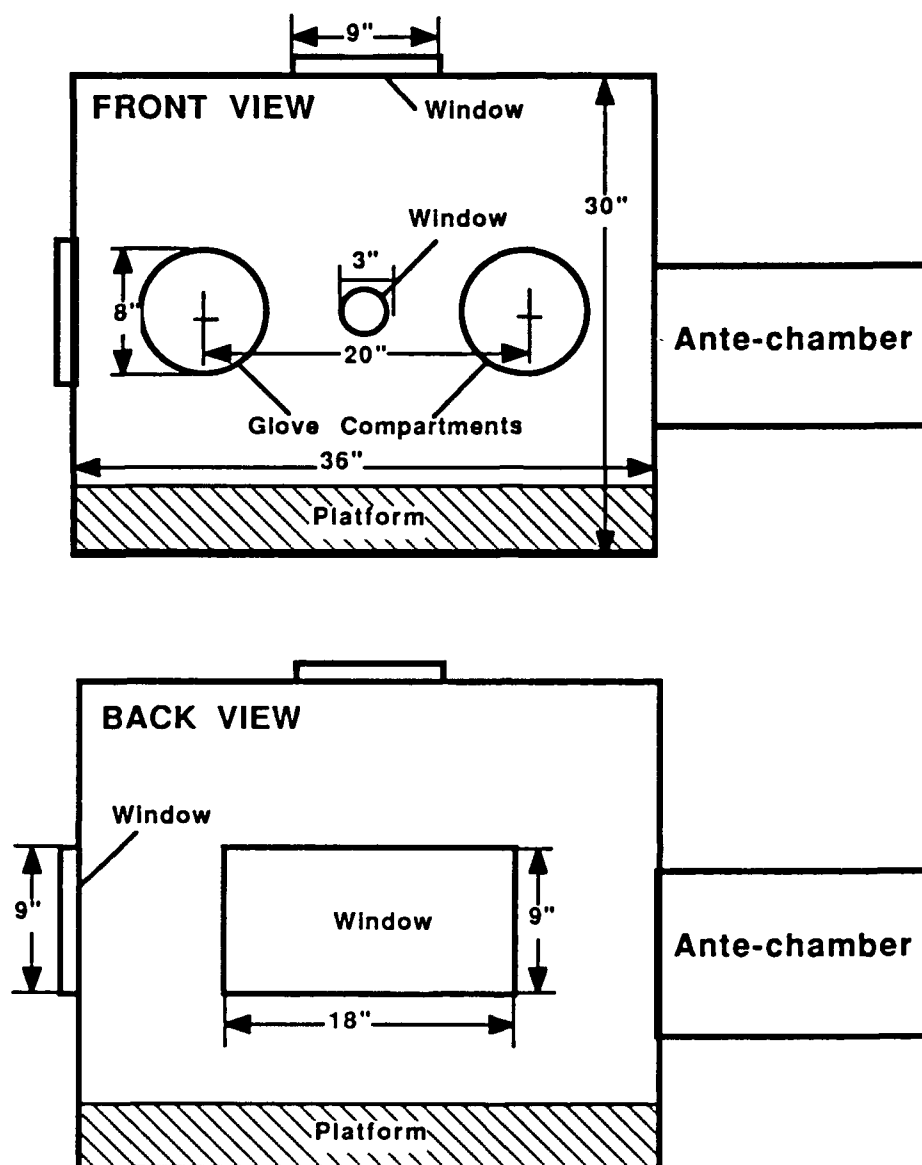


Figure 2. Schematic of the Vacuum Chamber



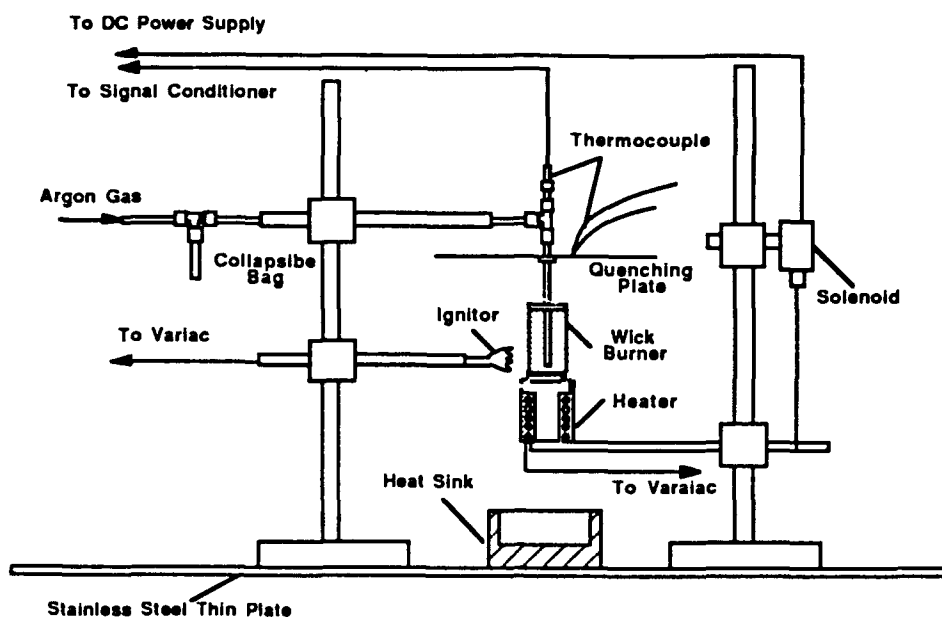


Figure 3. Schematic of the Burner Arrangement

The gas supply to the chamber was illustrated in Fig. 4. To prepare the wick burner, the chamber was first evacuated to  $<0.2$  torrs using a chemical pump (Alcatel Model 2020CP1) and back filled with the zero-gas grade argon gas (Matheson 99.998% purity) to atmospheric pressure. A "purge" argon gas (Air Products zero-gas grade, 99.99% purity) was also plumbed to the vacuum chamber intended for fast delivery of argon gas in case of emergencies. The pressure of the purge gas was regulated slightly above 0.1 MPa (1 atm). The chamber pressure was monitored by two vacuum gauges (Wika, -30"/30" Hg) and one pressure transducer (Wallace & Tiernan Model 66-100, 0.005 psia precision). High purity  $\text{SF}_6$  (Matheson, Instrument Purity 99.99% purity) was used as oxidant and technical grade  $^7\text{Li}$  (99.9 % purity, Lithium America; 12.7 mm lithium rods packed in mineral oil or argon gas) was used as fuel.

The lithium sample was cleaned with hexane and methanol and carefully prepared to obtain contamination free samples for combustion experiments. Prior to each experiment, the wick burner was cleaned with methanol and baked at low pressures (inside the vacuum chamber) to remove contaminants. The entire chamber (including the ante-chamber) was evacuated to  $<0.2$  torr

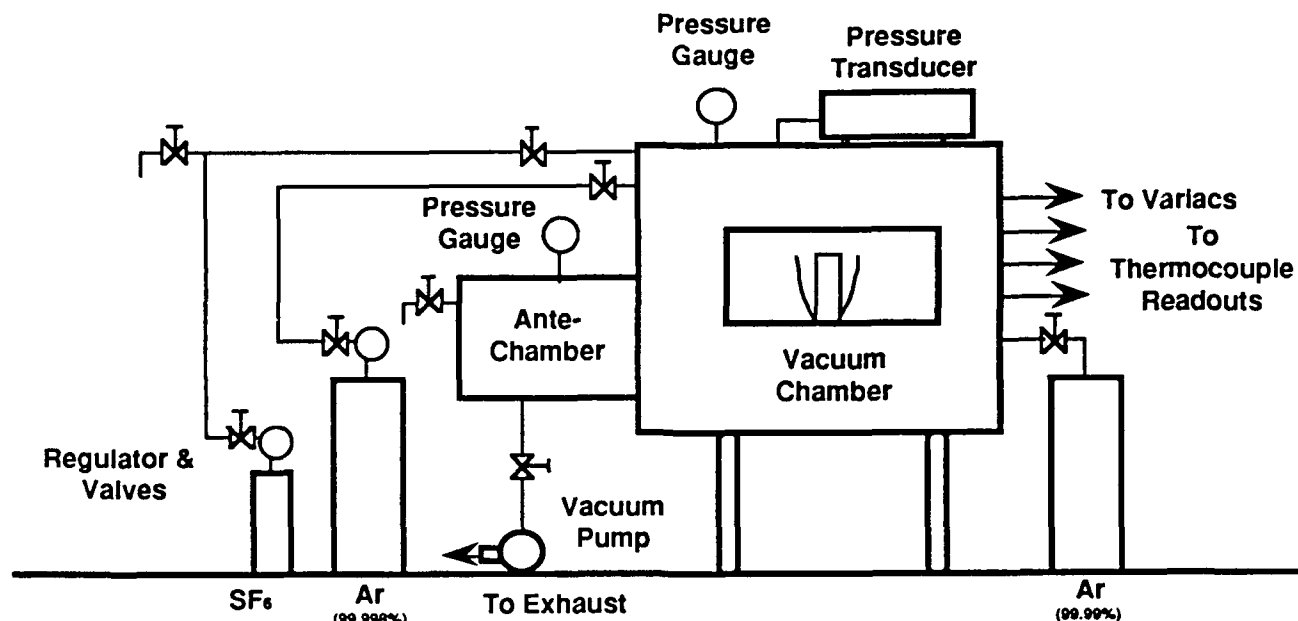


Figure 4. Gas Supply

and back-filled to one atmospheric pressure with argon gas. This step was repeated at least once. The inner door of the ante-chamber was then closed manually (through the glove port). An untreated lithium sample (covered with mineral oil) was placed inside the ante-chamber through the outer door of the ante-chamber. The ante-chamber was then evacuated and back-filled to one atmospheric pressure with argon gas. The lithium sample was moved to the main chamber from the ante-chamber through the inner door of the ante-chamber. Reagent grade Hexane (99.9 % purity) was used to remove mineral oil from the lithium sample and methanol (Reagent Grade; 99.9 % purity) was used to remove hexane and oxidized layer from the lithium sample. Following the preparation procedure outlined above, cleaned lithium samples were obtained. The cleaned lithium sample was placed inside the wick burner. The chamber was evacuated and the lithium sample was heated. The lithium sample was heated to 400 °C (or above) to wet the wick surface. The chamber was then back-filled with  $\text{SF}_6$  for subsequent combustion experiments. The combustion process was monitored and recorded using a VHS format video camera (Panasonic WV3110-DX)

for subsequent review and analysis. A 35 mm camera (Canon AE-1) was used to take photographs of the video directly off a TV screen.

The optical arrangement of the diagnostics is shown in Fig. 5 in which a top view of vacuum

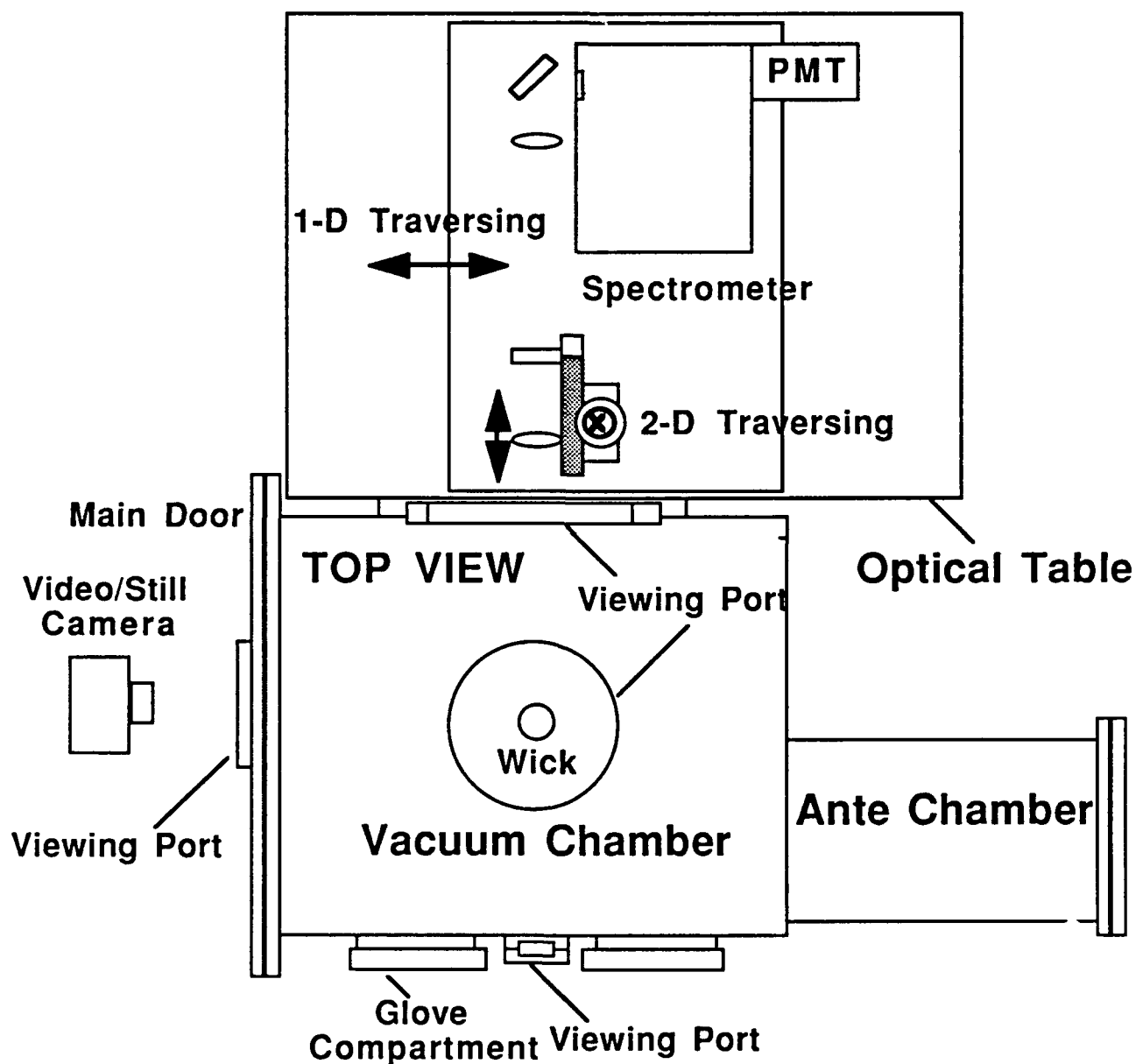


Figure 5. Experimental Set Up for Wick Combustion Diagnostics

chamber was illustrated. A three dimensional traversing mechanism which consists of linear bearings and uni-slides was designed, acquired (from commercial products) and assembled with in-house made components. The design provides a fixed optical axis (focusing lenses and spectrometer) for laser induced fluorescence (LIF) measurements; the variation in vertical heights was accounted for by a pair of periscopes. Similar to that employed in the layout of LIF measurements, another traversing mechanism was also designed and assembled for laser Doppler velocity measurements using a back scattering mode operation.

### 3.2 LIF Thermometry

To develop the laser induced fluorescence (LIF) thermometry using  $^7\text{Li}_2$  (Lithium America, 99.9 % purity) as fluorescence species, experiments were conducted with the apparatus shown in Fig. 6. The major components of the apparatus include a heat-pipe oven, an argon-ion laser, optics and photodetectors. The heat pipe was configured with five arms. Each arm has an optical window at its end. The heat pipe was operated to maintain a uniform inside temperature and was used for LIF thermometry calibration experiments. The oven temperature was determined from thermocouples (ANSI K-type) located at the center of the heat pipe. In the experiments, the central portion of the heat pipe was electrically heated and the far end was water cooled to protect the windows from attack by Li vapor. In preparing calibration experiments, lithium was placed inside the heat pipe and followed by evacuation and heating to remove contaminants from lithium. Argon gas was introduced to confine Li vapor in the central portion of the heat pipe, to protect the window from direct contact with lithium vapor and to control the system pressure. Adjusting heater and vacuum pump operation, steady-state conditions of desired temperature and pressure can be reached for LIF thermometry experiments.

An argon ion laser (Coherent CR-6, 6 W) was used to excite  $^7\text{Li}_2$ . The coincidence lines of argon ion laser output and  $^7\text{Li}_2$  spectrum are well-documented (e.g., Luh, Bahns and Stwalley, 1988), the values are summarized in Table 2. In the present study, the single line excitation was

Table 2. Fluorescence Lines of  $^7\text{Li}_2$  Molecule Excited by Argon Ion Laser (B-X Transitions)

Laser Wavelength (nm)	B-X ( $v', J' - v'', J''$ )	LIF Wavelength (nm)
457.9	(9,9 - 2,8) (9,5 - 2,5)	533.9-567.2 550.3-564.9
472.7	(8,32-3,31)	550.0-568.6
476.5	(4,24-1,24) (9,61-2,62) (11,34-5,34)	525.1-551.0 582.7-586.4 551.0-588.9
488.0	(2,31-1,30) (6,45-3,46) (4,73-0,74) (9,19-6,18) (12,36-7,36)	514.7-540.7 548.4-559.6 552.3-564.7 566.8-568.1 584.1-591.3
514.5	(8,61-7,61) (3,30-5,29) (9,38-9,37)	574.6-582.1

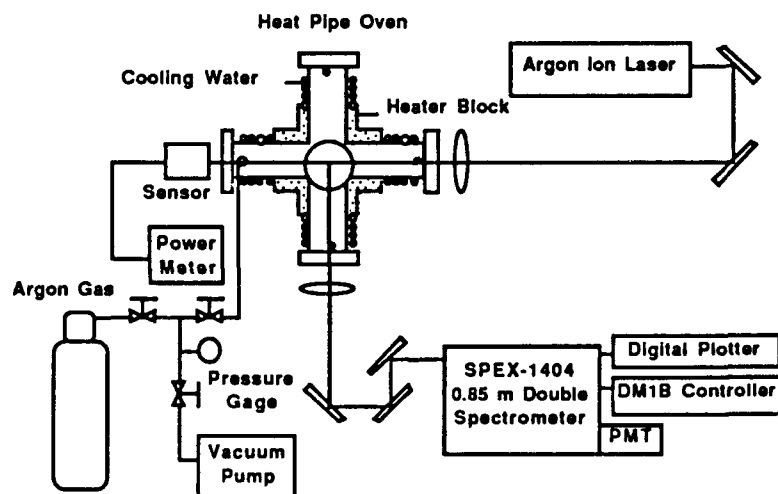


Figure 6. LIF Thermometry Calibration Experimental Set Up

employed. In the discussion herein the temperature was obtained from a single line excitation (488 nm), assuming that the two closely-spaced fluorescence lines excited by a single-laser line have constant collection volume, detection efficiency and same quenching effects. The fluorescence signal was collected at a right angle from the excitation laser beam. A 0.85 m double spectrometer (SPEX-1404) was used to obtain the fluorescence spectrum. The height of the spectrometer entrance slit was 20 mm and the width was adjusted in the range 20 to 50  $\mu\text{m}$  to obtain good spectral resolutions. The measured fluorescence spectrum was analyzed, comparing with the theoretical spectrum. A Xe-lamp was used as reference to ensure the wavelength assignments.

To examine the fluorescence spectrum in a quantitative manner, the theoretical frequency and corresponding intensity distribution must be calculated from the theory to confirm the assigned fluorescence spectrum. The molecular constants of  $B^1\Pi_u$  and  $X^1\Sigma_+$  states of  $^7\text{Li}_2$  were taken from Hessel and Vidal (1978) to calculate theoretical fluorescence line frequencies from specified excited states:

$$\nu = T'(v', J') - T''(v'', J'') + \Delta T'(v', J') \quad (20)$$

where  $\nu$  is the fluorescence frequency resulting from the difference in term energies between the excited state  $T'(v', J')$  and the ground state  $T''(v'', J'')$ . The  $\nu$  and  $J$  are the vibrational and rotational quantum number of each respective state. The term energy of the excited B level ( $v', J'$ ) is

$$T(v', J') = \sum_{ij} A'_{ij} (v' + \frac{1}{2})^i [J' (J'+1) - 1] j \quad (21)$$

and the corresponding term value of the ground state is given by

$$T(v'', J'') = \sum_{ij} A''_{ij} (v'' + \frac{1}{2})^i [J'' (J''+1)] j \quad (22)$$

The lambda-doubling  $\Delta T(v',J')$  of  $B^1\Pi_u$  state is as follows

$$\Delta T(v',J') = \delta \left( \sum_{lk} a'_{lk} \left(v' + \frac{1}{2}\right)^i (J' (J'+1) - 1) j \right) \quad (23)$$

where  $\delta = 0$  for the Q series ( $\Delta J = 0$ ) and  $\delta = 1$  for P and R series ( $\Delta J = \pm 1$ ). The Dunham-type molecular constants are denoted as  $A'_{ij}$ ,  $A''_{ij}$  and  $a'_{lk}$  (Hessel and Vidal, 1978). The theoretical intensities of fluorescence spectrum were calculated following Luh (1985) in which a computer program known as Intensity (Zemke and Stwalley, 1984) was used to solve the Schrodinger equation for theoretical transition frequencies and the corresponding intensities.

In  $\text{Li}_2$  LIF thermometry calibration, the 488.0 nm output of the Argon-ion laser was used as the excitation source. The resultant fluorescence spectrum is a collection of  $^7\text{Li}_2$ ,  $^6\text{Li}_2$  and  $^7\text{Li}^6\text{Li}$  molecules. The fluorescence of  $^7\text{Li}_2$  resulted in two stronger series from the excited states B(2,31) and B(6,45). The ratio of spectrally resolved fluorescence lines from B(2,31) and B(6,45) was used to obtain the temperature information. Two models, linear fluorescence and saturated fluorescence, were considered in analyzing the spectroscopy data. The measured fluorescence signal can be expressed as

$$\Phi = \beta \Omega_c V_c \left(\frac{d\sigma}{d\Omega}\right) N_j I_L \quad (24)$$

where  $\beta$  denotes the collecting efficiency,  $\Omega_c$  the solid angle,  $V_c$  the collection volume,  $\left(\frac{d\sigma}{d\Omega}\right)$  the scattering cross section,  $N_j$  the number density at the excited state and  $I_L$  the laser flux.

Linear Fluorescence. A three-level model was employed to describe the fluorescence signal resulting from transitions due to laser excitation. The linear fluorescence is

$$\Phi = \beta \Omega_c V_c h \nu_{jk} A_{jk} N_j \quad (25)$$

where  $h$  is the Planck's constant,  $\nu_{jk}$  and  $A_{jk}$  are the frequency and Einstein coefficient of the fluorescence transition between the excited state  $j$  and ground state  $k$ . The population of the excited state under the steady state assumption can be expressed as a function of absorption  $W_{ij}$ , Einstein coefficient  $A$  and quenching rate  $Q$ :

$$N_j = \frac{W_{ij}}{W_{ji} + A + Q} \quad (26)$$

The absorption  $W_{ij}$  is related to Einstein coefficient  $A_{ij}$ :

$$W_{ij} = \frac{2 B_{ij} I_L(\nu_{ij})}{\pi c \Delta \nu} \quad (27)$$

where  $\Delta \nu$  is the spectral width of the laser line and the absorption coefficient  $B_{ij}$  is defined as

$$B_{ij} = \frac{c^3}{8\pi h \nu_{ij}^3} A_{ij}. \quad (28)$$

The above equation was obtained assuming negligible quenching effects ( $Q = 0$ ) which is typical at low pressures and negligible stimulated emission ( $W_{ji} = 0$ ) compared to the absorption  $W_{ij}$ . In fact, the stimulated emission can be eliminated when the fluorescence signal was collected at a right angle from the laser beam. It was further assumed that the population follows a Boltzmann distribution, yielding a linear equation for fluorescence

$$\Phi_{lin} = \left( \frac{\beta \Omega_c V_c}{16\pi^3 c} \right) \left( \frac{I_L(\nu_{ij}) A_{ji} \lambda_{ij}^3}{\Delta \nu} \right) \nu_{jk} \left( \frac{A_{jk}}{\Sigma A_{jk}} \right) N_T \frac{g_j}{Z_{Tot}} \exp \left( \frac{hc E_j}{kT} \right) \quad (29)$$

Where  $\Delta \nu$  is the laser spectral width,  $N_T$  the total number density of laser coupled states,  $g_j$  the degeneracy of the excited state ( $2J_j + 1$ ),  $Z_{Tot}$  the total partition function and  $E_j$  the energy of the



initial state.

Considering two fluorescence lines resulting from two different series excited by the same laser line, one can extract the temperature from the ratio of the two fluorescence signal  $\Phi_{lin1}$  and  $\Phi_{lin2}$ :

$$T = \frac{h c \Delta E}{K \ln \left( \frac{\Phi_{lin1} A_2 v_2 g_2 I_L(v_2)}{\Phi_{lin2} A_1 v_1 g_1 I_L(v_1)} \right) \frac{B_2}{B_1}} \quad (30)$$

where  $\Delta E$  is the ground state energy difference ( $\text{cm}^{-1}$ ) between the two fluorescences lines of different series. Since the laser intensity is likely to vary over the two excitation frequencies,  $v_1$  and  $v_2$ , the difference in  $I_L(v_1)$  and  $I_L(v_2)$  must be considered when the linear fluorescence model is employed for temperature measurements.

Saturated Fluorescence. At saturated states, the fluorescence signal is independent of laser power and absorption coefficients. The saturated fluorescence signal is (Lucht, 1982):

$$\Phi_{sat} \propto A_{jk} v_{jk} \frac{g_i g_j}{g_i + g_j} \exp \left( \frac{h c E_i}{k T} \right) \quad (31)$$

where  $g_i$  and  $g_j$  are the degeneracies of the ground and excited states, respectively. The above equation also assumes negligible quenching effects. Taking the ratio of two saturated fluorescence line signals,  $\Phi_{sat,1}$  and  $\Phi_{sat,2}$ , one obtains

$$T = \frac{h c \Delta E}{k \ln \left( \frac{\Phi_{sat1} A_2 v_2 \frac{g_{2i} g_{2j}}{g_{2i} + g_{2j}}}{\Phi_{sat2} A_1 v_1 \frac{g_{1i} g_{1j}}{g_{1i} + g_{1j}}} \right)} \quad (32)$$

where temperature is expressed in terms of ground state energy difference ( $\Delta E$ ), saturated fluorescence intensities ( $\Phi_{sat}$ ), frequencies ( $v$ ), Einstein coefficients ( $A$ ) and degeneracies ( $g$ ).

### 3.3 Emission Spectrum and Temperature Measurements

#### 3.3.1 Scanning Spectrum Measurements

An optical system shown by Fig. 7 is constructed to measure the emission spectrum of wick combustion of Li and SF<sub>6</sub>. A scanning monochromator (0.35-m; McPherson 270) is used. The scanning speed of the grating element was set at 20 Å/s, controlled by a McPherson 700-51 scanner. A spectral range of 400 to 700 nm was investigated. A cooled photomultiplier tube (PMT; EMI 9659QB) is used as detector. The PMT was cooled to -22 C by a temperature controller (EMI FACT 50 MK III). A negative voltage of -800 volts was applied to the cathode of the PMT by a high-voltage power supply (Fluke 412B). The PMT output was modulated by a mechanical chopper and a lock-in amplifier (Stanford Research, SR-530), cf. Fig. 7. The output of the PMT is interfaced to a Mac IIx microcomputer; a 12-bit multichannel data acquisition board (National Instruments MIO-16-H) in conjunction with a direct memory access board (National Instruments DMA-8-G boards) is used. The data acquisition was controlled by a software driver LabView (National Instruments). The A/D rate was set at 1000 samples/s.

#### 3.3.2 Simultaneous Emission Spectrum Measurements

The strong Li atomic emission was observed from the measurements employing the scanning monochromator. To remedy the uncertainties in temperature measurements due to temporal variations in flame emission, a two-dimensional CCD camera (384 x 576 pixels; Photometrics camera with a TH7882 CCD element) with a gated image intensifier (ITT F4111 intensifier) is used for simultaneous spectral measurements, e.g. see the schematics shown in Figure 8. The flame image is focused (with a magnification factor of 0.17) onto the entrance slit of a grating monochromator (0.125-m; ORIEL Model 77250). The 1200 lines/mm ruled grating (ORIEL 77298, blazed at 500 nm) of the monochromator allows a band pass of 300 to 1000 nm with a reciprocal dispersion of 6.4 nm/mm at the exit slit plane. The entrance slit (200 µm width) is oriented horizontally to pass a portion of the image in radial direction. A refocusing lens ( $f = 100$  mm) is used to image the spectrum at the exit plane onto the intensifier head. The spatially-

distributed spectrum measured by the CCD has a spectral range of 100 nm and an averaged spectral resolution of 0.2 nm/pixel. The spatial resolution of the CCD camera is 185  $\mu\text{m}$ /pixel.

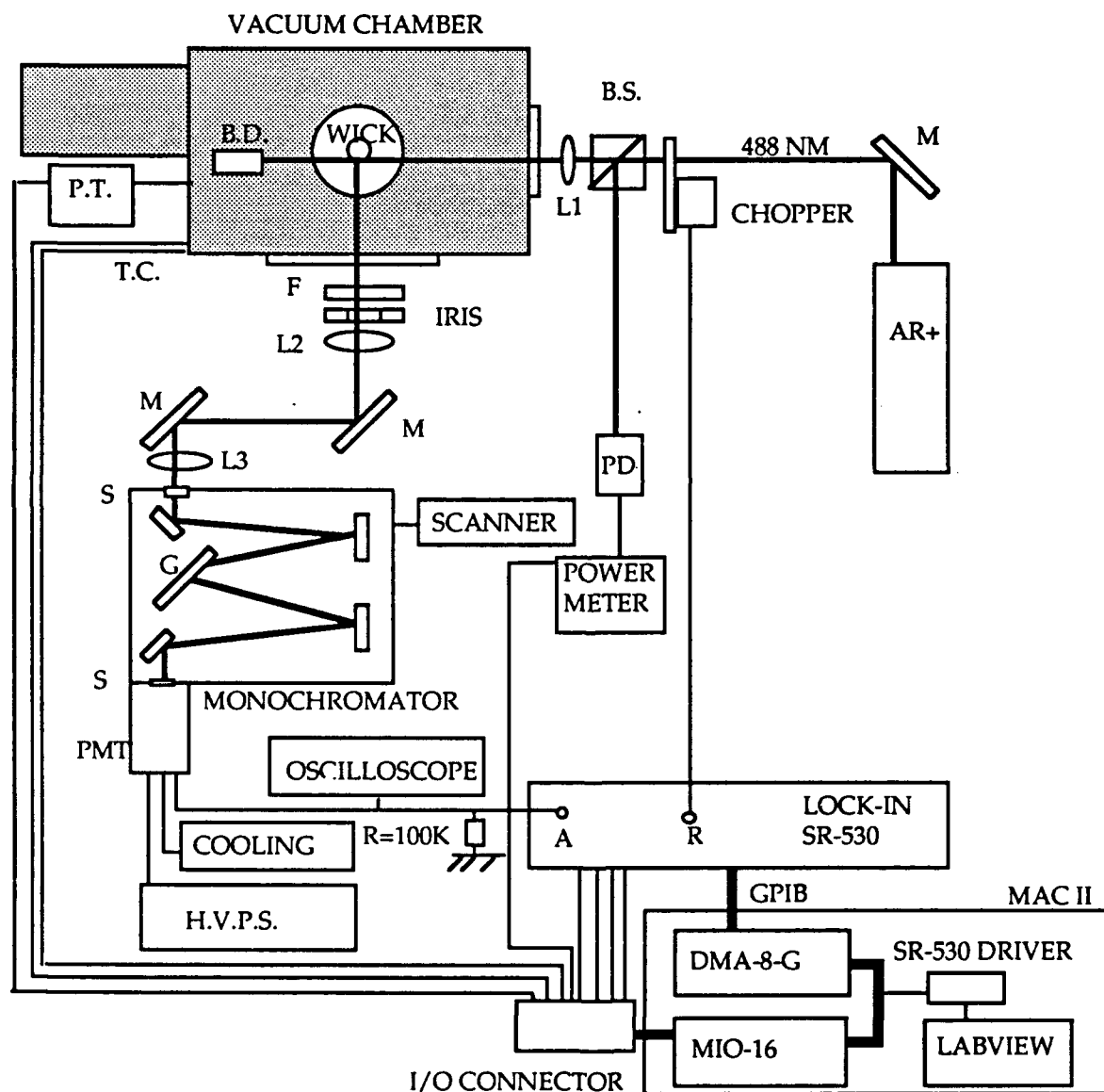


Figure 7. Experimental Set-up for Modulated LIF/Emission Measurements.

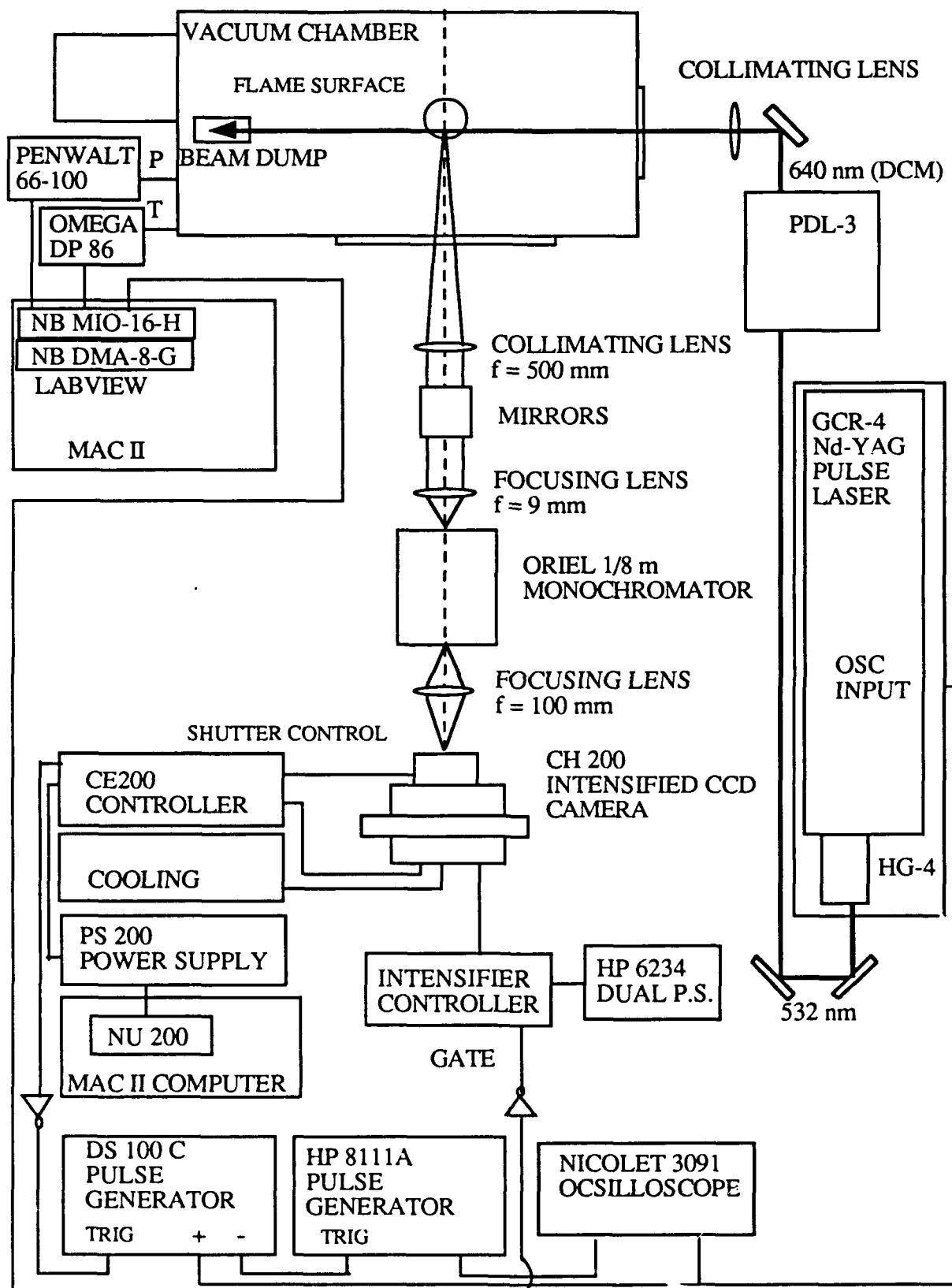


Figure 8. Experimental Set-up for Simultaneous LIF/Emission Measurements.

The intensifier is gated externally to ensure a fully opened shutter and a well controlled gate duration. The instrumentation set up also allows for thermally assisted two-photon laser induced fluorescence measurements of Li atoms. The experimental set up is designed for sequential measurements of two images, separated by 800 ms with a pre-determined exposure time. The synchronization of the laser and intensifier is achieved by the circuit shown in Figure 9. The TTL signal used to control the shutter of the CCD camera is used to trigger the pulsed dye laser and the intensifier. The TTL signal duration was measured, showing the delay time being linearly proportional to the exposure time specified by the controller. A pulse generator (Systron Donner 100C) is used to trigger the pulsed dye laser through an oscillator external input, a delay from the rising edge of the shutter TTL signal is set to ensure a fully opened CCD camera. The intensifier is gated by a pulse generator (HP8111A), triggered by the "falling edge" of the pulse for laser triggering, cf. Fig. 10. The synchronization circuit allows only one laser firing among two sequential exposures. The double images for each laser firing will have the spectral measurements of the two-photon LIF and the flame spontaneous emission. The time sequence of laser and intensifier trigger signals is shown in Figure 10. The intensifier is gated to open for 2 ms with a 3 ms delay to account for the laser firing delay. It should be noted that a shorter gated time for the intensifier, e.g., 10  $\mu$ s, has been established and the two-photon LIF technique is being developed (Hsu, 1991). The spectral data and analysis presented in this report are based on the spontaneous emission measurements.

The detection optics are aligned to avoid distortion of the spectrum image. A He-Ne laser (632.8 nm) placed inside the vacuum chamber is used for optical alignment. The CCD camera head is mounted on a traversing optical rail. The spectral location of the 632.8 nm of the CCD camera is set at the center of the image by adjusting the monochromator. A pencil mercury lamp (Oriol C-73-14) set at 10 mA is placed at the optical path of the He-Ne laser beam. The mercury lamp output is used for wavelength calibration for the spectral range of 400 to 500 nm.

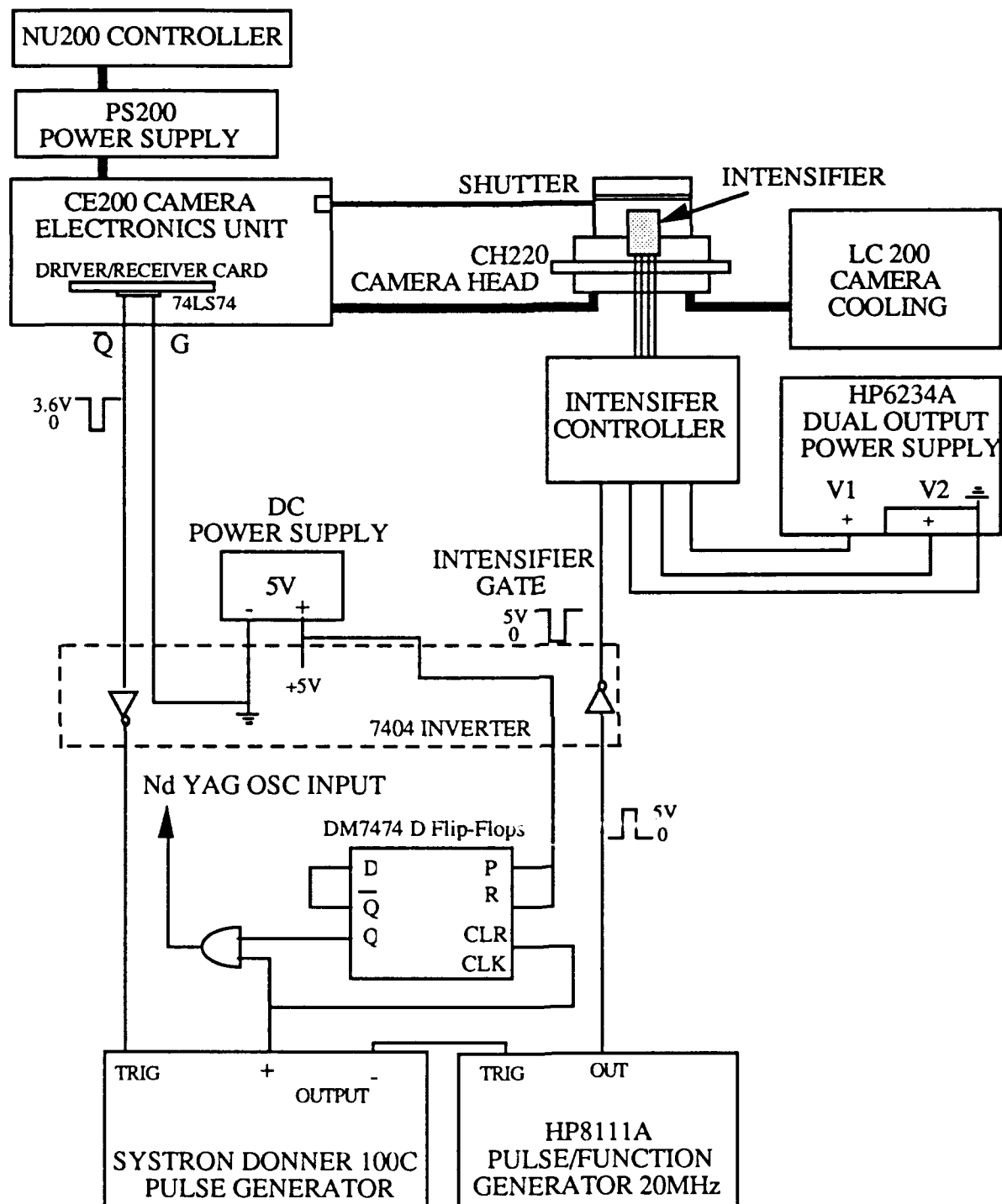


Figure 9. Synchronization Circuit for LIF/Emission Measurements.

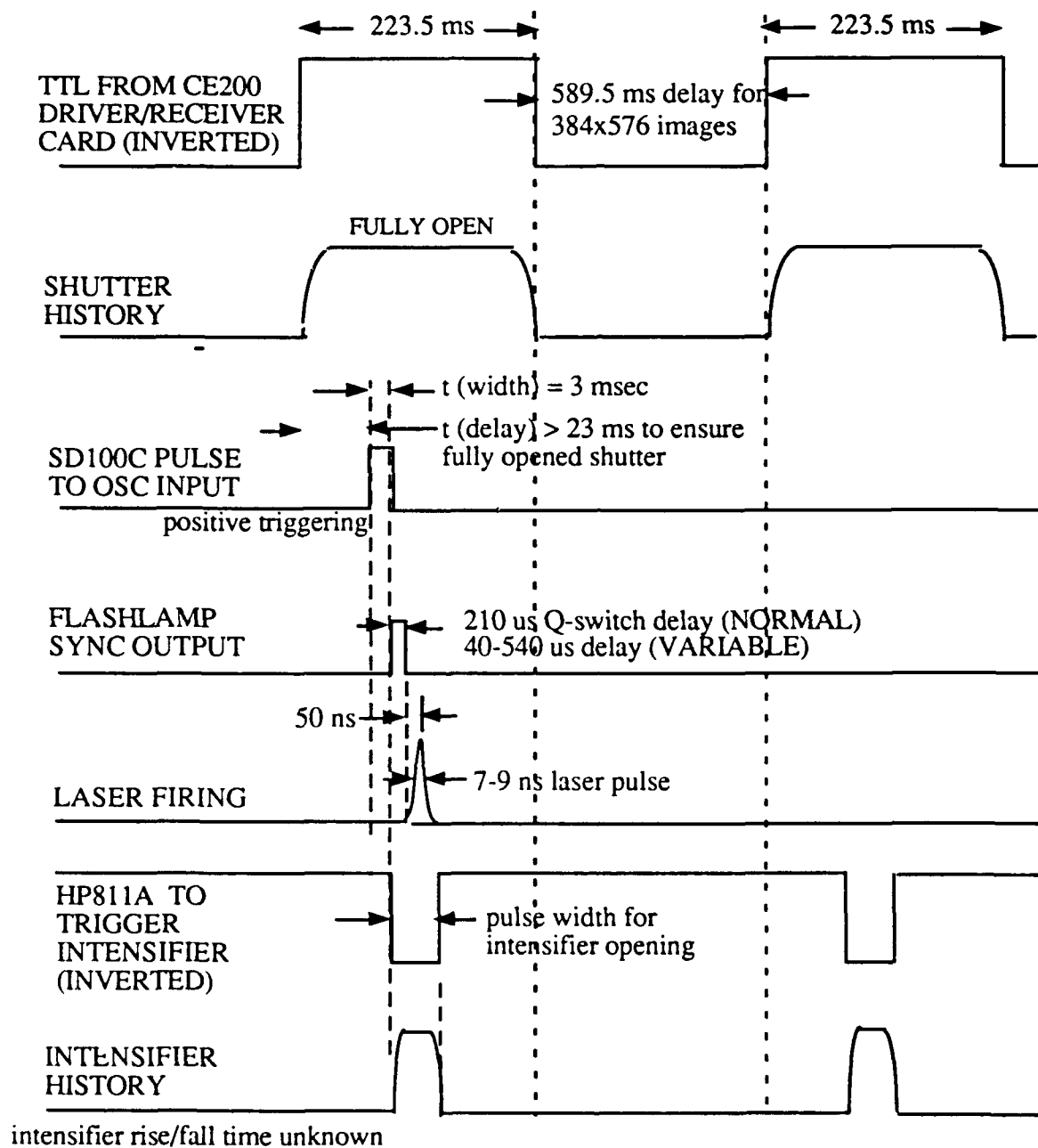


Figure 10. Timing Sequence for Laser Firing and Intensifier Gating.

The spectral response of the system is calibrated by a radiation reference source (BARNES Model 11-210; maximum temperature of 1000 C) which has an aperture of 12.7 mm (0.5 in.) in diameter. The radiation source requires about two hours of operation to reach 1000 C for steady operation. The accuracy of the temperature is within 5 C at 1000 C. Following the Planck's law, the spectral intensity of a blackbody is

$$W(\lambda) = \frac{C_1 \lambda^{-5}}{\text{Exp}(-C_2/\lambda T) - 1} \quad (33)$$

where  $W(\lambda)$  is spectral emissive power and  $C_1$  and  $C_2$  are constants. The spectral intensity distribution is obtained by integrating the intensity in spatial direction at the center wavelength from different images. The corresponding theoretical intensity at different wavelengths are calculated. The collection angle and the spectral response of each pixel are assumed to be constant. The spectral response  $\beta(\lambda)$  of the system is obtained by the ratio of normalized experimental and theoretical values

$$\beta(\lambda) = \frac{W_{\text{Theory}}(\lambda)}{W_{\text{CCD}}(\lambda)} \quad (34)$$

The spectral response of the system in the spectral range of 400 nm to 500 nm is summarized in Figure. 11. A 7 % error is found for the spectral range of 450 nm to 500 nm.



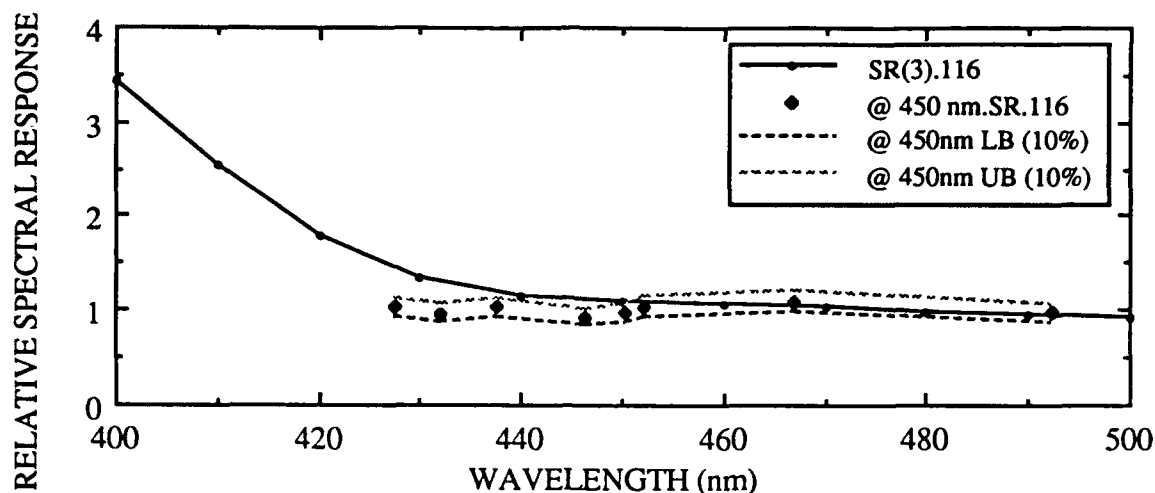


Figure 11. Relative System-Spectral-Response for Spectral Range of 400 to 500 nm.

The data from the two-dimensional images of flame emission were used to calculate the flame temperature at each spatial location. Each image consists of 384 pixels in spatial direction and 576 pixels in spectral direction. Each pixel has a 12-bit resolution for intensity measurements. A virtual instrument (VI) supported by LabView (National Instruments) has been constructed to analyze the spectral data. The intensity of each spectral line is integrated employing the Simpson rule. The integration range extends to 2 % of the base-line intensity on both wings of the line profile. The curve-fitted relative spectral response was taken into account in intensity integration.

The flame temperature can be estimated from the emission spectrum employing the two-line method. The self absorption (by lithium atoms) is neglected. This assumption is generally true for non-resonance lines. The collection volume is assumed to be uniform over the spectral range. The two-line method calculates the flame temperature from the intensity ratio of two emission lines, i.e.,

$$T = \frac{hc \Delta E}{k \ln(R/W)}, \text{ and} \quad (36)$$

$$R = \frac{I_1/\beta(\lambda_1)}{I_2/\beta(\lambda_2)} \quad (37)$$

$$W = \frac{A_2 g_{j2} / g_{i2} \lambda_2}{A_1 g_{j1} / g_{i1} \lambda_1} \quad (38)$$

where the  $\Delta E$  (in  $\text{cm}^{-1}$ ) is the energy difference (in  $\text{cm}^{-1}$ ) of the two excited states,  $A$  (in  $\text{s}^{-1}$ ) is the Einstein coefficient of spontaneous emission,  $g_j$  and  $g_i$  are respectively the degeneracy of the excited and ground states,  $\beta(\lambda)$  is the relative spectral response, and  $\lambda$  (nm) is the center wavelength resulted from the transition between the excited and ground states.

The sensitivity of the flame temperature calculated by the two-line method can be obtained by differentiating Eq. (35), yielding

$$\frac{dT}{T} = \frac{kT}{hc \Delta E} \frac{d(RW)}{RW} \quad (38)$$

Equation (38) states that the sensitivity increases as the flame temperature is increased and decreases as the energy difference ( $\Delta E$ ) is increased. The accuracy of the flame temperature also depends on the atomic transition constants, i.e.,  $A$ ,  $g$  and  $\lambda$ . The error in temperature calculations resulted from a 10 % error in the constants and intensity ratio is plotted in Figure 12 for the transition pairs centered at 460 nm and 497 nm.

The measured intensity is an integrated quantity along the optical path. To obtain the spatial profile of the intensity, a numerical method is employed. An axisymmetric flame is assumed; the emission intensity, thus, is a function of radius ( $r$ ) and height ( $z$ ), e.g., see the schematic shown in Figure 13. The integrated intensity  $I(x_j)$  at location  $x_j$  from the measurement can be expressed in terms of radial intensity  $I(r)$  being integrated along the optical path, i.e.,

$$I(x_j) = 2 \int_x^{r_0} I(r) dy, \text{ or} \quad (39)$$

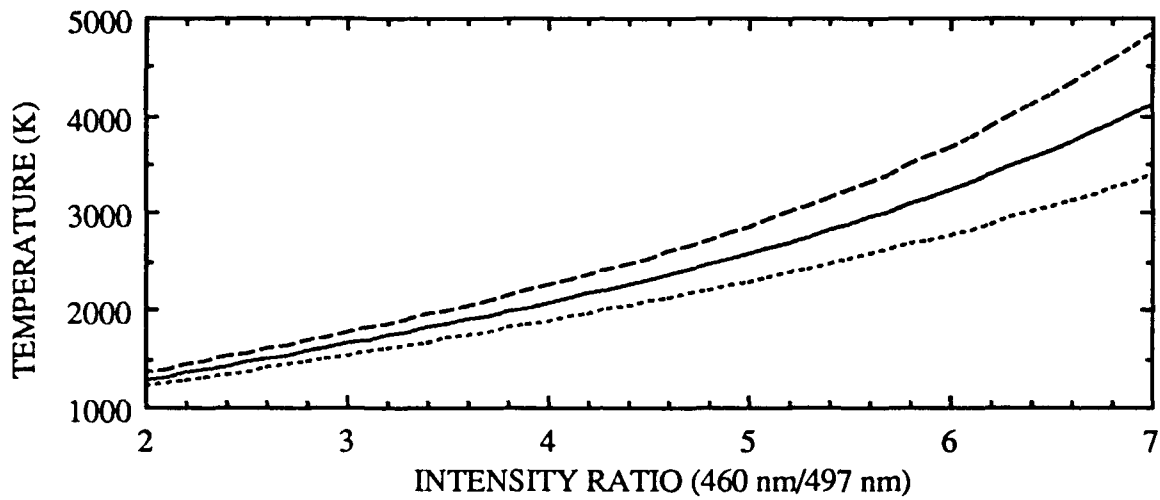


Figure 12. Error of Temperature Measurements vs. Intensity Ratio at 460 nm and 497 nm Lines.

$$I(x_j) = 2 \sum_{i=1}^n I(r_i) dy_i \quad (40)$$

where  $r_o$  is the boundary of the integration,  $dy_i$  is the integration path between adjacent rings, and  $dy_i$  is

$$dy_i = \sqrt{r_i^2 - x_j^2} \quad (41)$$

Equation (40) is solved numerically employing a backward substitution scheme. It is noted that the collection angle is considered to be constant due to a small solid angle resulting from the large  $f$ -number employed in the experiments.

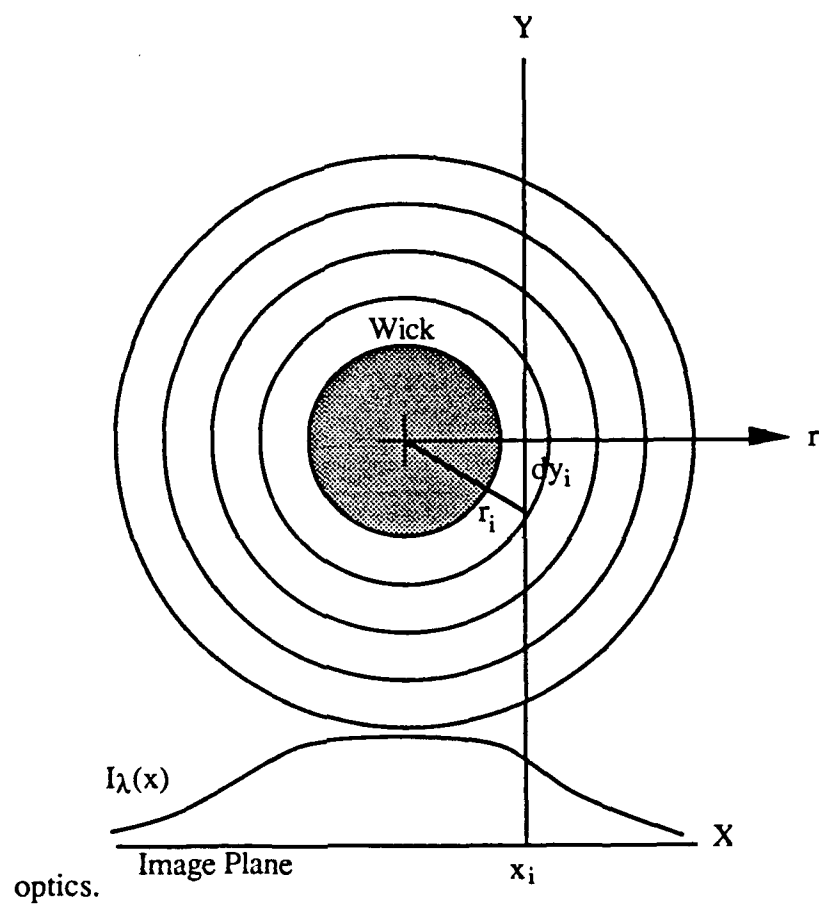


Figure 13. Schematic for Intensity Inversion.

## IV. RESULTS AND DISCUSSION

### 4.1 LIF Thermometry

The fluorescence spectrum of  ${}^7\text{Li}_2$  excited by an Argon ion laser at 488 nm was analyzed. The assignments of the spectrum were confirmed with theoretical calculations in terms of fluorescence-line wave numbers and relative intensities. The spectral assignments are summarized in Tables 3 and 4 where  $\lambda$  is the wavelength in Å and  $\omega$  is the vacuum wavenumber. The comparison of relative intensity between experimental data and theoretical predictions was summarized by Hsu (1991). The uncertainty of intensity measurements was improved by reducing the spectrometer scanning speed and spectrometer entrance slit width. Setting the scanning speed at 5 Å/s and the entrance slit at 25  $\mu\text{m}$ , the measured fluorescence intensity at 507 °C was in good agreement with theoretical prediction, cf. Hsu (1991). The measured fluorescence ratios of three different transition series in the temperature range 850 to 1050 K were compared to theoretical calculations. The experimental data were bounded by the calculations employing linear and saturated fluorescence models, for example, see Figs. 14-15; a more detailed discussion will appear in Hsu (1991). Refinements, however, are needed to implement LIF thermometry techniques to combustion studies. In specific, the effects of excitation laser intensity on measured fluorescence signals need to be evaluated.

### 4.2 Wick Combustion

Prior to Li-SF<sub>6</sub> combustion experiments, the vacuum chamber was tested with combustion experiments of ethanol and hexane burning in the air. A vertical cylindrical wick (25 mm I. D. and 50 to 89 mm long) in which nonflammable fiberglass was packed was placed inside the chamber. The fiberglass was used to retain the liquid fuel inside the wick. Reagent grade ethanol (99.9 % purity) or hexane (99.9 % purity) was used. The wick combustion yields a non-luminous gaseous diffusion flame for ethanol at low pressures (0.03 and 0.05 MPa) and a luminous flame for ethanol and hexane at atmospheric pressure (0.1 MPa). The combustion process can be divided in three

stages: ignition, stable burning and extinction. After the ignitor was activated, a stable axisymmetric diffusion flame around the wick was established following a transient ignition stage. During the ignition stage, the flame spread over the wick surface, it usually started from the upper portion of the wick and propagated down to the leading edge of the cylinder. Near the fuel burn-out, the flame became unstable. Local extinction from the leading edge of the wick was seen, yielding an oscillating flame surface in longitudinal direction until extinction was observed.

Table 3. Assignment of  $^7\text{Li}_2$  B(2,31) Fluorescence Excited at 488 nm

$v''$	R-BRANCH			P-BRANCH		
	Experiment	Theory		Experiment	Theory	
	$\lambda$ (Å)	$\omega$ (1/cm)	$\omega$ (1/cm)	$\lambda$ (Å)	$\omega$ (1/cm)	$\omega$ (1/cm)
0	4800.25	20826.43	20826.11	4819.30	20744.11	20744.22
1	4879.95	20486.30	20486.52	4899.20	20405.80	20405.54
2	4960.90	20152.01	20152.24	4980.45	20072.91	20072.17
3	-	-	-	5083.30	19666.78	19744.15
4	5126.75	19500.10	19499.75	5147.55	19421.31	19421.55
5	5211.90	19181.52	19181.66	5232.90	19104.55	19104.41
6	5298.20	18869.09	18869.10	5319.55	18793.36	18792.82
7	5385.65	18562.70	18562.12	5407.80	18486.67	18486.86
8	5474.75	18260.60	18260.91	5497.05	18186.53	18186.82

Table 4. Assignment of  $^7\text{Li}_2$  B(6,45) Fluorescence Excited at 488 nm

$v''$	R-BRANCH			P-BRANCH		
	Experiment	Theory		Experiment	Theory	
	$\lambda$ (Å)	$\omega$ (1/cm)	$\omega$ (1/cm)	$\lambda$ (Å)	$\omega$ (1/cm)	$\omega$ (1/cm)
0	-	-	21576.66	-	-	21461.99
1	4705.50	21245.79	21244.67	4730.75	21132.39	21131.32
2	4778.95	20919.25	20918.06	4804.85	20806.49	20806.05
3	-	-	20596.88	4879.95	20486.30	20486.23
4	4929.15	20281.82	20281.20	4955.95	20172.14	20171.93
5	5005.75	19971.46	19971.11	-	-	19863.23
6	5083.30	19666.78	19666.67	5110.75	19561.15	19560.22
7	-	-	19368.00	-	-	19263.00
8	5240.80	19075.75	19075.19	5269.50	18971.86	18971.67
9	-	-	18788.36	-	-	18686.35
10	5401.60	18507.89	18507.64	5431.20	18407.02	18407.18
11	5483.05	18232.96	18233.17	5512.65	18135.06	18134.30
12	5564.75	17965.27	17965.10	5595.00	17868.14	17867.88
13	5646.45	17705.33	17703.62	5677.70	17607.88	17608.09

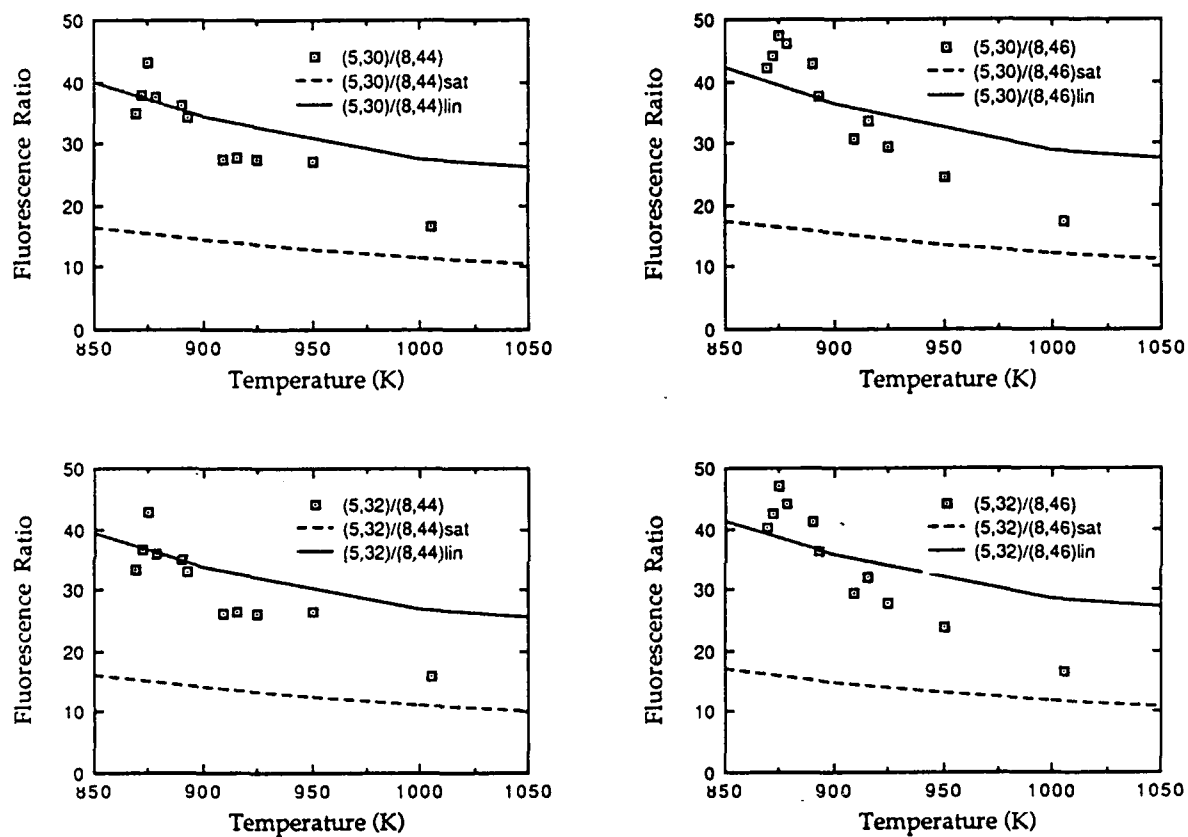


Figure 14. LIF Thermometry Calibration of  $^7\text{Li}_2$ ; B (2, 31)-X(5, 30/32)/B(6,45)-X(8,44/46)

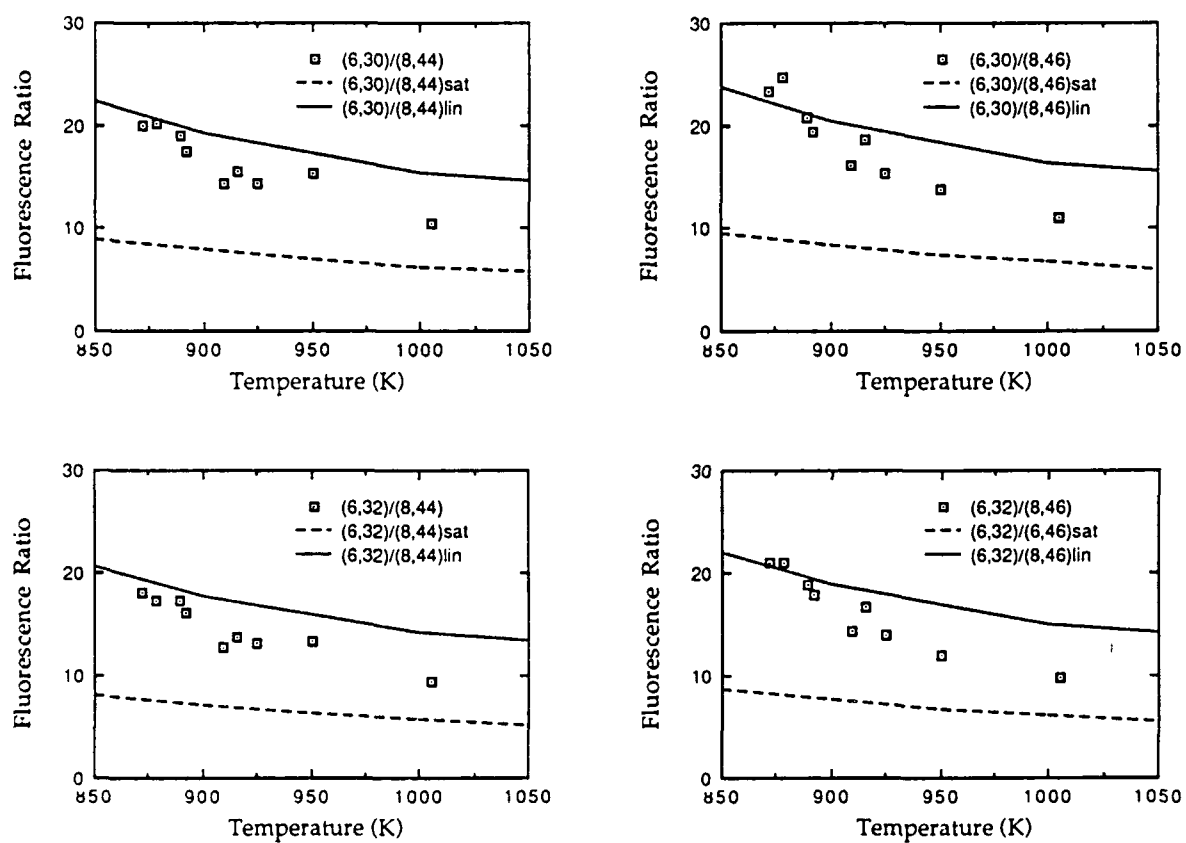


Figure 15. LIF Thermometry Calibration of  $^7\text{Li}_2$ ; B (2, 31)-X(6, 30/32)/B(6,45)-X(8,44/46)



Spatial and temporal periodicities were observed in wick diffusion flames. The oscillation frequency was estimated in the range 5 to 8 Hz. The oscillation frequency of ethanol diffusion flames decreased when the system pressure was increased. Ethanol and hexane were found to have similar oscillation frequencies at 0.1 MPa. The spatial wavelength (e.g. 30 to 80 mm in the present experiments) increased as the system pressure was decreased. It is also noted that the oscillation in wick diffusion flames is similar to flame flickers in buoyant jet diffusion flames (Chen et al, 1989b), suggesting the existence of buoyancy driven vortical structures in a vertical boundary-layer diffusion flame. The flame stand-off distance increased as the system pressure was decreased (around 5 mm at 0.1 MPa and 10 mm at 0.03 MPa at a location 25 mm from the leading edge), in qualitative agreement with theoretical predictions.

Li-SF<sub>6</sub> Combustion. Combustion of lithium solids (in flake form, i.e. 2 to 3 mm thickness and 12 mm in diameter) in SF<sub>6</sub> (0.01 MPa) was successfully accomplished using Nichrome wires (AWG Gauge 20) as an ignitor. Following a transient stage (ejection of lithium) after the ignitor was activated, a very bright flame covered the lithium solid. A lithium "droplet" (molten lithium) was subsequently formed on the stainless steel plate inside the combustion chamber. Lithium was seen to wet the stainless steel (spreading on the surface in a dome or bell shape). The burning of the Li drop continued for a few seconds before the extinction and solidification of the melt occurred. The sequential events of Li-solid combustion were summarized by Hsu (1991).

Wick combustion of Li and SF<sub>6</sub> was studied. In the experiments conducted up-to-date, the chamber was filled with SF<sub>6</sub> at 0.01 MPa. The diameter of the wick was 32 mm and the height, excluding the end caps, was around 25 mm. Only one layer stainless steel screen was used to construct the wick cylinder. Heating the lithium to a temperature above 400 °C was necessary to wet the wick surface. A long nichrome wire coil (about 200 mm long) sided with the wick cylinder was used as the ignitor in the experiment shown in Fig. 16. Photographs shown in Fig. 17 were taken from the video at six different times after the ignitor was actuated, i.e. 2, 4, 17, 29, 32 and 33 seconds (cf. Fig. 16, from left to right and top to bottom). Once successful ignition was

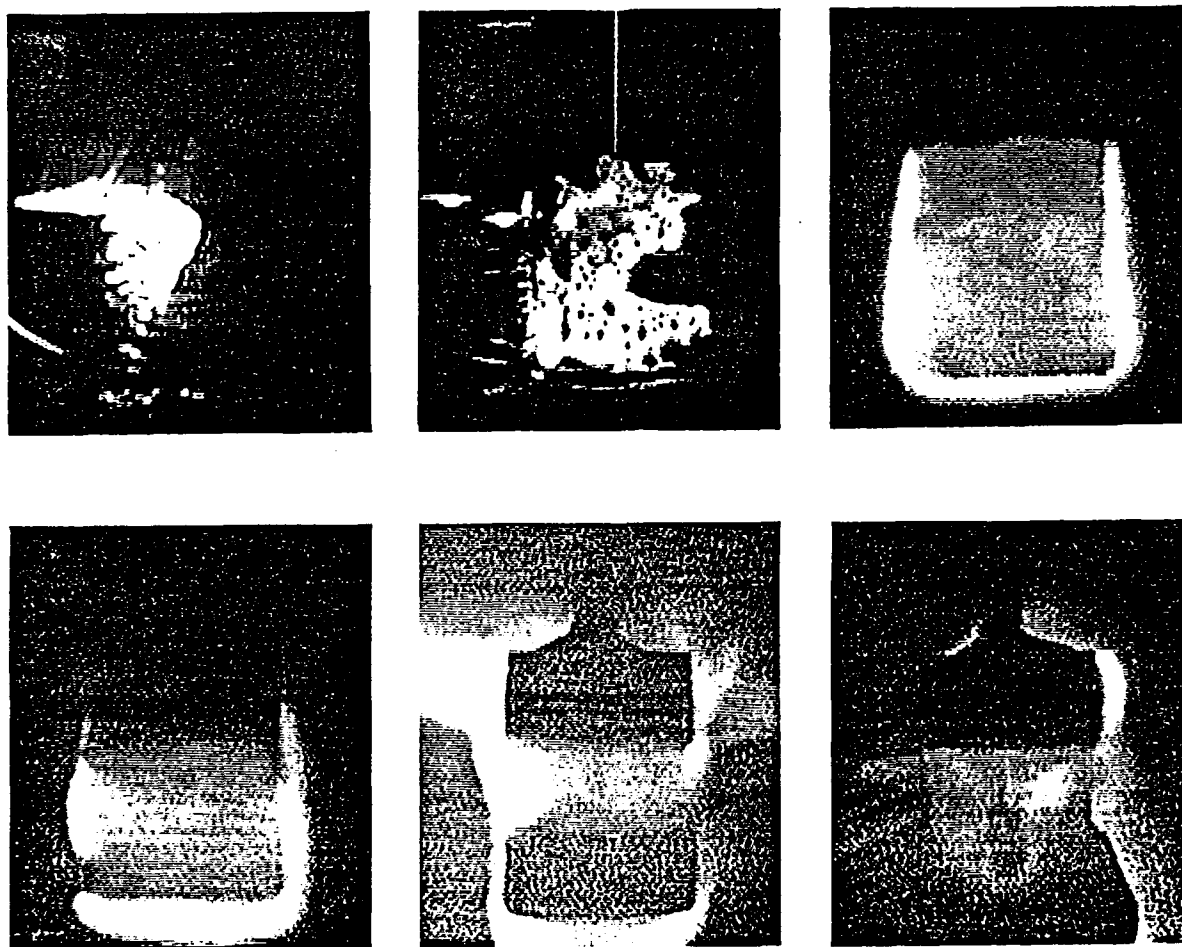


Figure 16. Wick Combustion of Li and SF<sub>6</sub> at 0.01 MPa

achieved, the flame sustained itself until the wick was burnt out. During combustion the chamber interior showed a glowing pinkish color. A bright pinkish flame around the wick was recorded in the video tape. The aperture of the video camera was partially closed. Immediately after ignition, the flame spread over the wick surface and dark spots inside the luminous flame were observed. The flame then covered the side (wick) and bottom (cap) surfaces of the cylinder, showing a "uniform" flame (bright) surface. The flame surface (bright luminous layer) appeared quite close to the wick surface, the stand-off distance was only a few mm away from the wick surface. Near burn out, local extinction first appeared at the bottom surface and the upper portion of the wick. The extinction of the flame at the upper wick surface probably was a result of non-wetted wick surface near "complete consumption" of lithium fuel. Shortly after local extinction at the upper wick surface, the wick was burned out. The bright pinkish flame luminosity is due to the resonance-line emission of Li atoms as determined by the scanning spectrum measurements, cf. Fig. 17. The emission spectrum is discussed in Section 4.4.

### 4.3 Theoretical Results

Ethanol-Air Wick Diffusion Flame. The results of ethanol-air wick diffusion flames are reported by Lyu and Chen (1991) and Lyu (1991). A summary is provided in this report. The conserved scalar approach yields a single equation for the interface condition, Eq. (17), dictated by the flame structure. One immediate observation is that the interface fuel vapor mass fraction is less than one under normal condition. This can be seen as the fuel vapor mass fraction decreases and the temperature increases as  $Z$  is decreased (or moving away from the interface). It is noted that the interface fuel vapor mass fraction may approach unity near the mixture thermodynamic critical point. Two system pressures, 0.03 and 0.1 MPa, were considered for ethanol-air wick combustion. The interface temperatures were determined 310 K and 336 K and the interface fuel vapor mass fractions were 0.6289 and 0.6382 for 0.03 and 0.1 MPa, respectively. The interface condition was obtained employing an iterative procedure to solve Eq. (17). Up to ten iterations

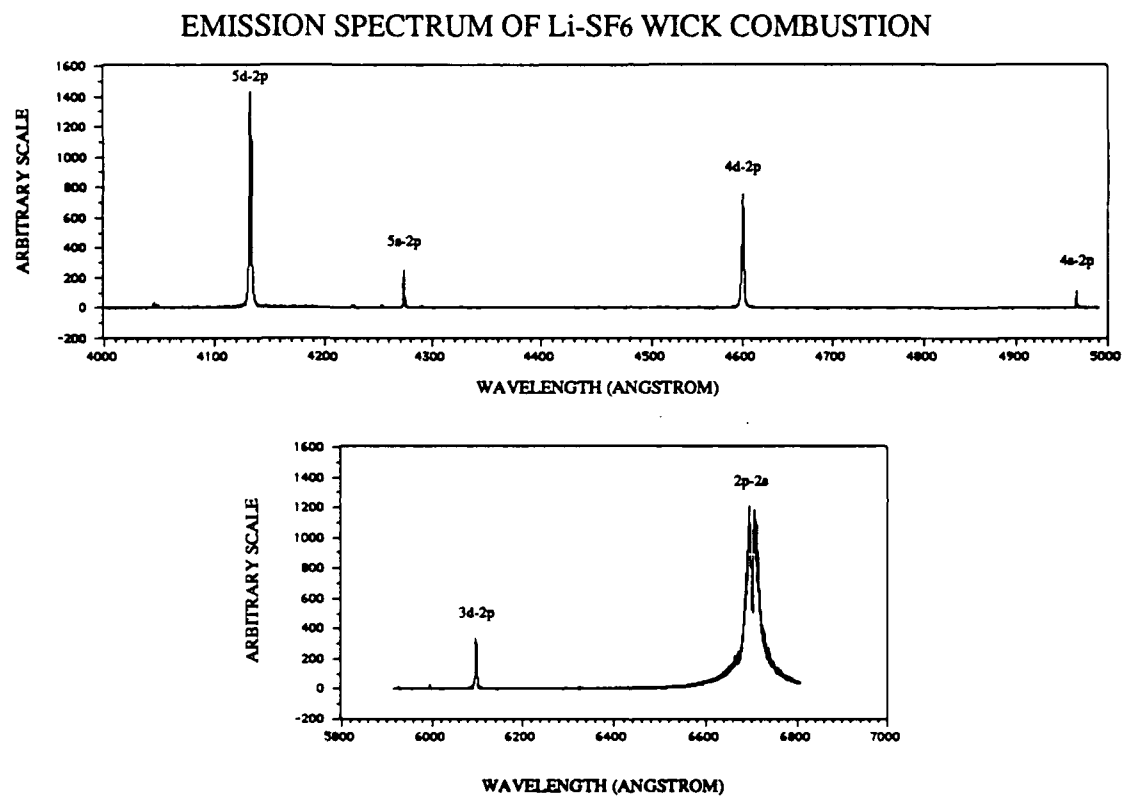


Figure 17. Spontaneous Emission Spectrum of Wick Combustion of Li and SF<sub>6</sub> at 0.01 MPa

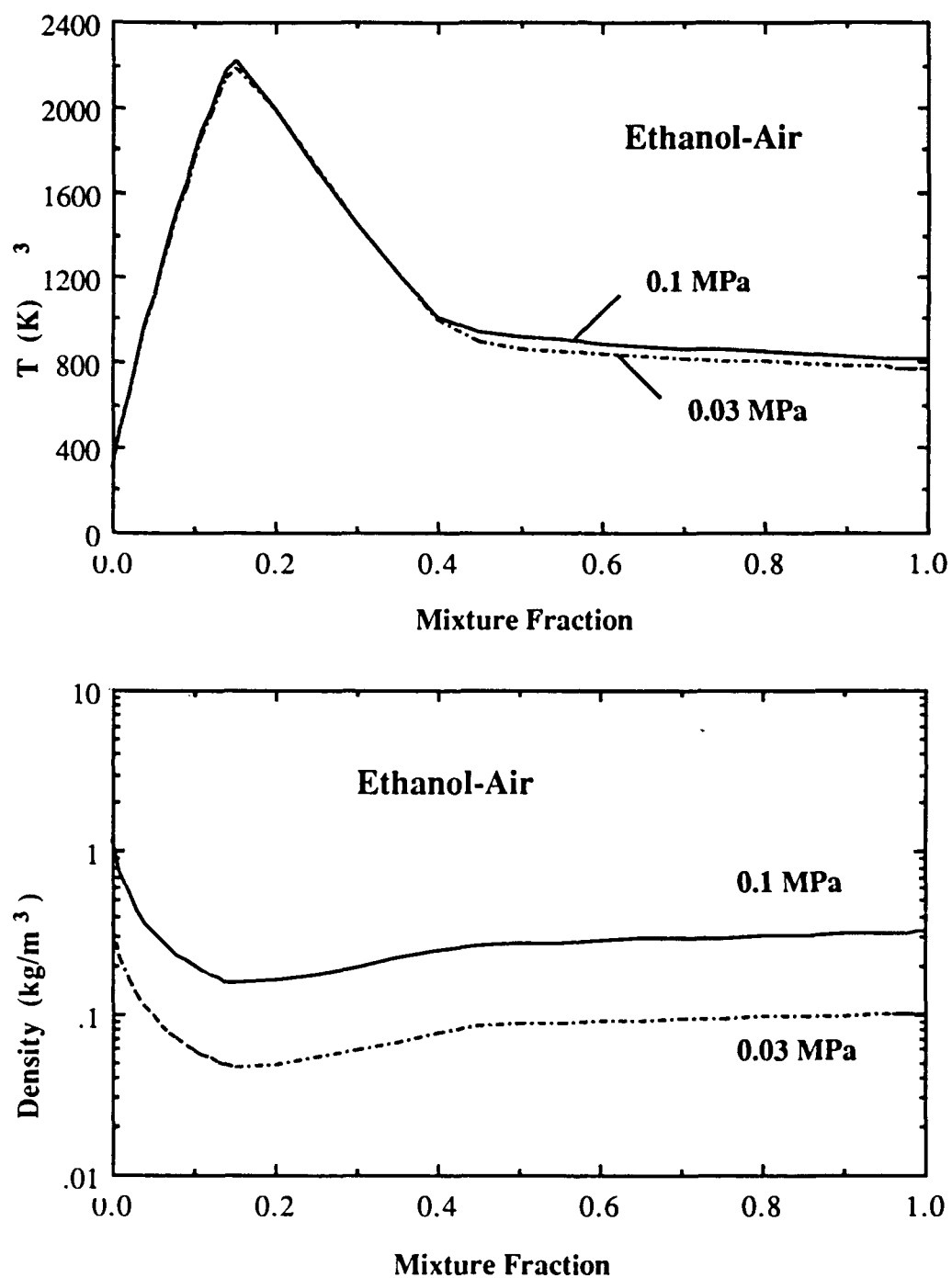


Figure 18. State Relationship (Temperature and Density) of Ethanol-Air Wick Diffusion Flame

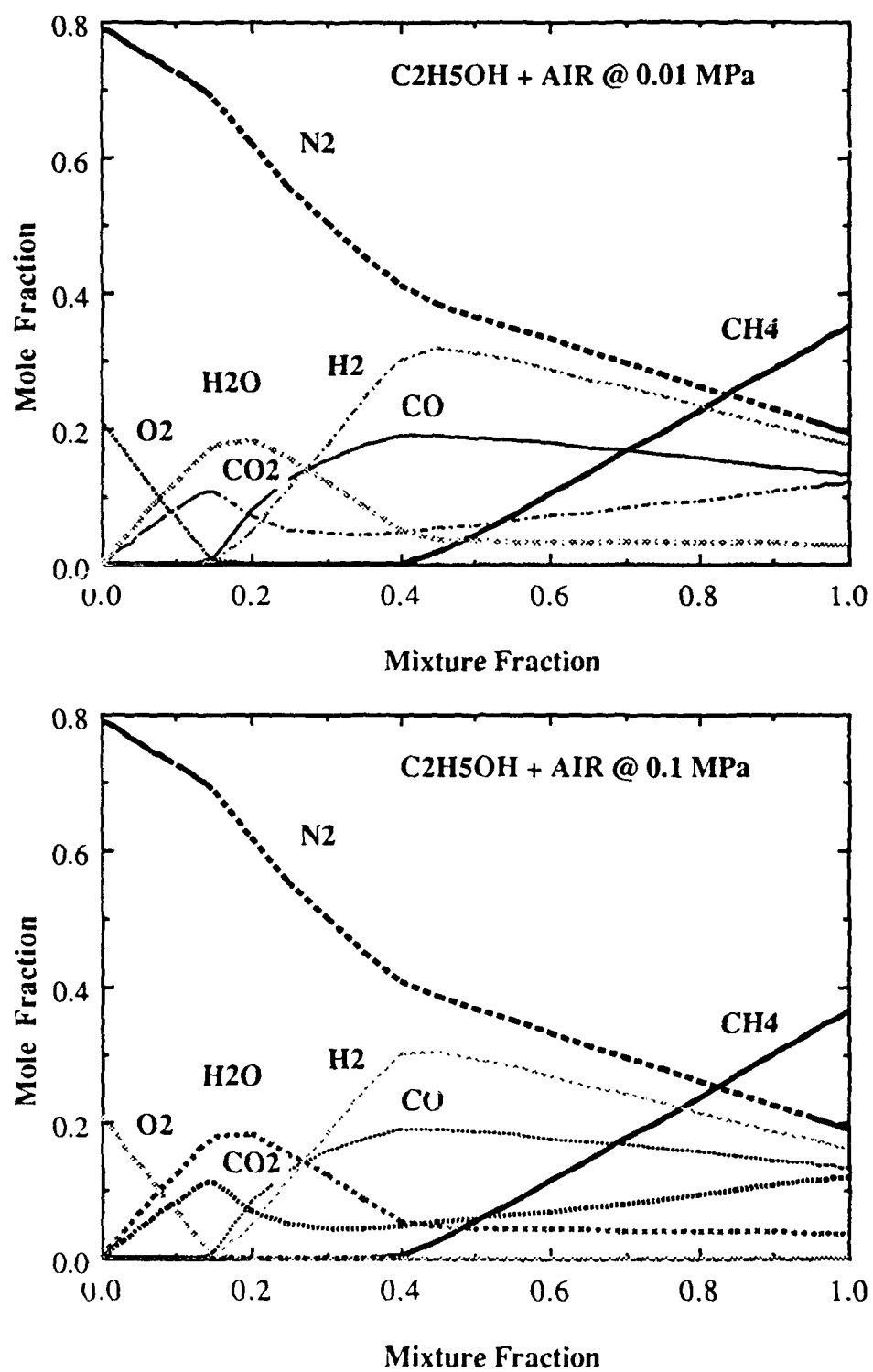


Figure 19. State Relationship (Concentration) of Ethanol-Air Wick Diffusion Flame

were required for the two pressures considered. The state relationships of ethanol-air wick diffusion flames at 0.03 MPa and 0.1 MPa are illustrated in Figs. 18 and 19, respectively. The higher flame temperature at 0.1 MPa is a result of the equilibrium shift due to reduced dissociation at higher pressures.

In the computation reported herein, a flat-plate 100 mm wick was considered. The computation showed that similarity solutions were maintained for the conditions examined although non-similar governing equations were retained in the analysis. The solution yields similar profiles for  $f$ ,  $f'$ ,  $f''$ ,  $Z$  and  $Z'$  at different streamwise locations when similarity variables were employed. The calculated mass burning rates yields a  $\xi^{-0.25}$  dependence, typical of laminar boundary layer diffusion flames. The calculated mass burning rates are illustrated in Fig. 20. The predicted mass burning rates also showed a pressure dependence of  $p^{0.64}$ .

To illustrate the pressure effects on the flame stand-off distance from the wick surface, the predicted temperature and streamwise velocity profiles at the trailing edge of the 100 mm wick were shown in Fig. 21. As shown in the figure, the stand-off distance increased as the system pressure was decreased. This is in qualitative agreement with the experiments conducted, although the analysis over-estimated the stand-off distance by 50 %. The maximum streamwise velocities are comparable for the two pressures considered, with a higher maximum velocity at 0.1 MPa. This is not surprising as the momentum source term in dimensionless form is similar for the two pressures considered.

Li-SF<sub>6</sub> Wick Diffusion Flame. Equilibrium computation was made to estimate the flame structure of the wick combustion, to estimate the pressure effects on wick combustion and to estimate the fuel composition effects on lithium combustion. The state relationships of Li-SF<sub>6</sub> wick flame at 0.01 and 0.1 MPa, assuming  $Y_{Li} = 1$  at the interface, are illustrated in Figs. 22-24. At the interface ( $Z = 1$ ), the fuel vapor was set at 1339 K and 1609 K (saturation temperatures) for 0.01 and 0.1 MPa, respectively. The equilibrium computation yields similar state relationships for 0.01 and 0.1 MPa. The 0.1 MPa case, however, has a higher temperature (4360 K versus 3884 K at

0.01 MPa) and a higher density as shown in Fig. 21. Fuel vapor was the major species at  $Z \approx 1$  either as lithium atoms (Li) or lithium dimers ( $\text{Li}_2$ ), e.g. see Figs. 23 and 24. The oxidant appeared as  $\text{SF}_6$  or  $\text{SF}_4$  at  $Z \approx 0$ ; however,  $\text{SF}_6$  decreased but  $\text{SF}_4$  increased as  $Z$  increased from zero. From the equilibrium prediction, LiF is the major combustion product. Gas-phase LiF

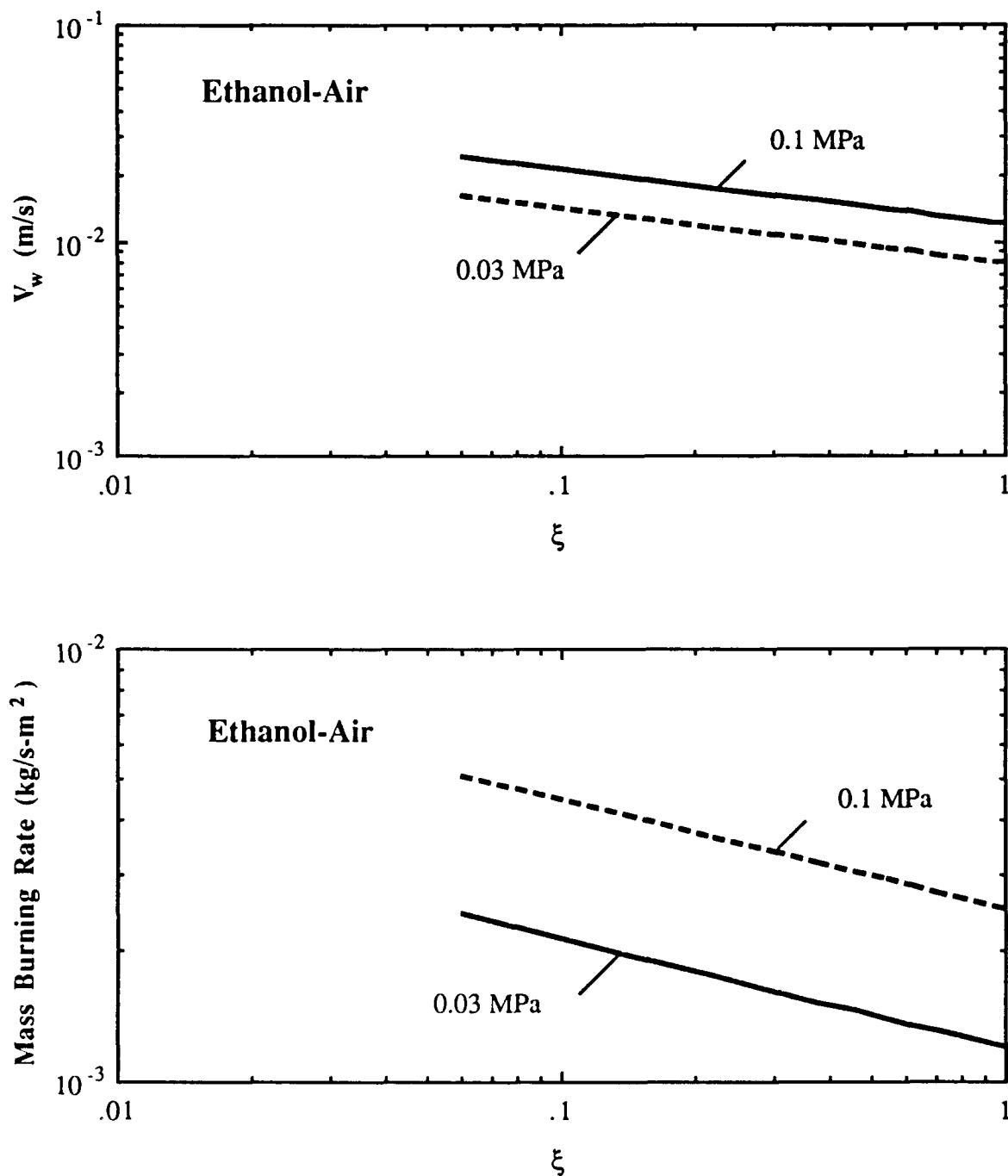


Figure 20. Predicted  $v_w$  and  $\dot{m}''$  of Ethanol-Air Wick Diffusion Flames



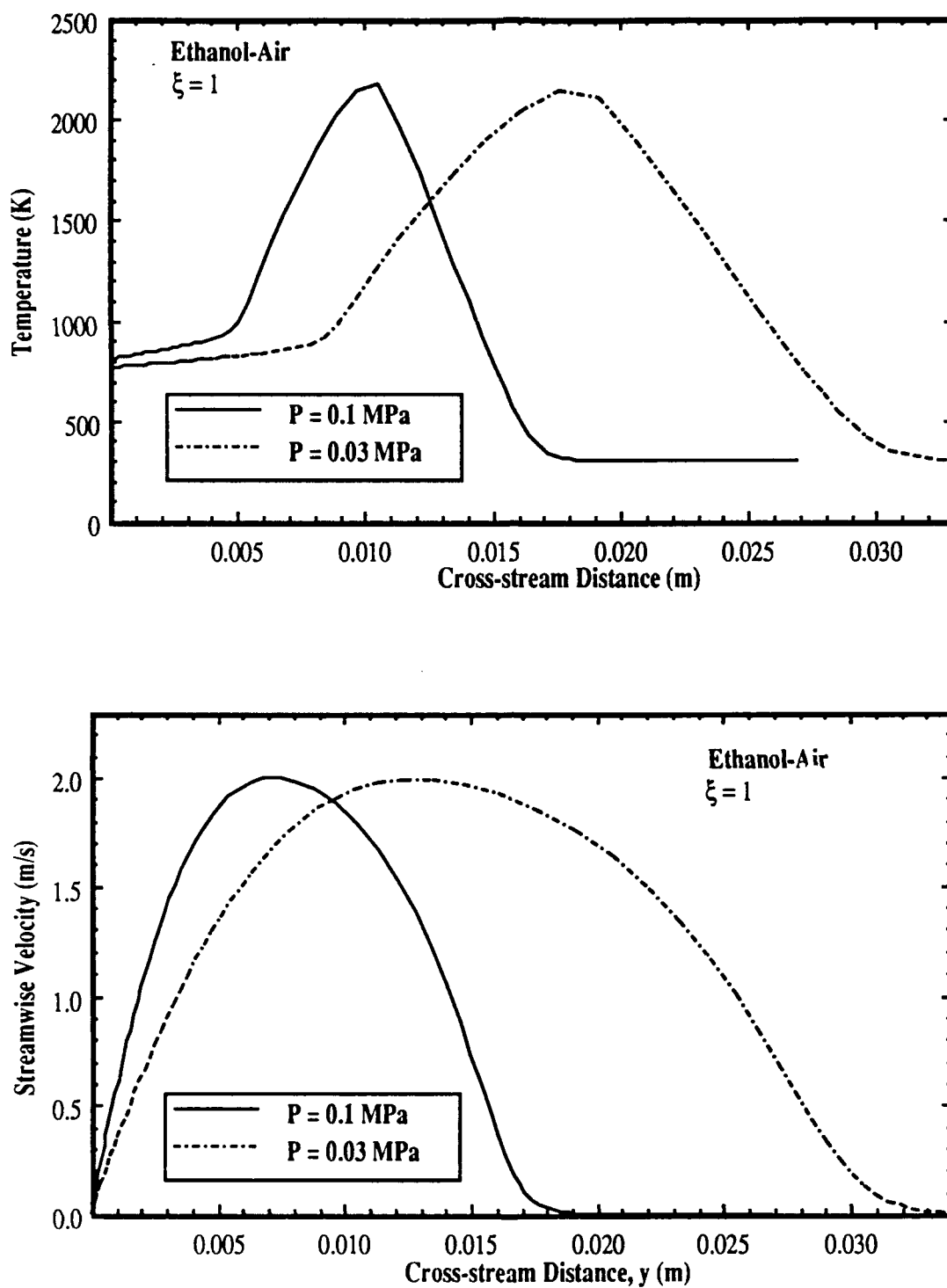


Figure 21. Predicted Flame Structure of Ethanol-Air Wick Diffusion Flames

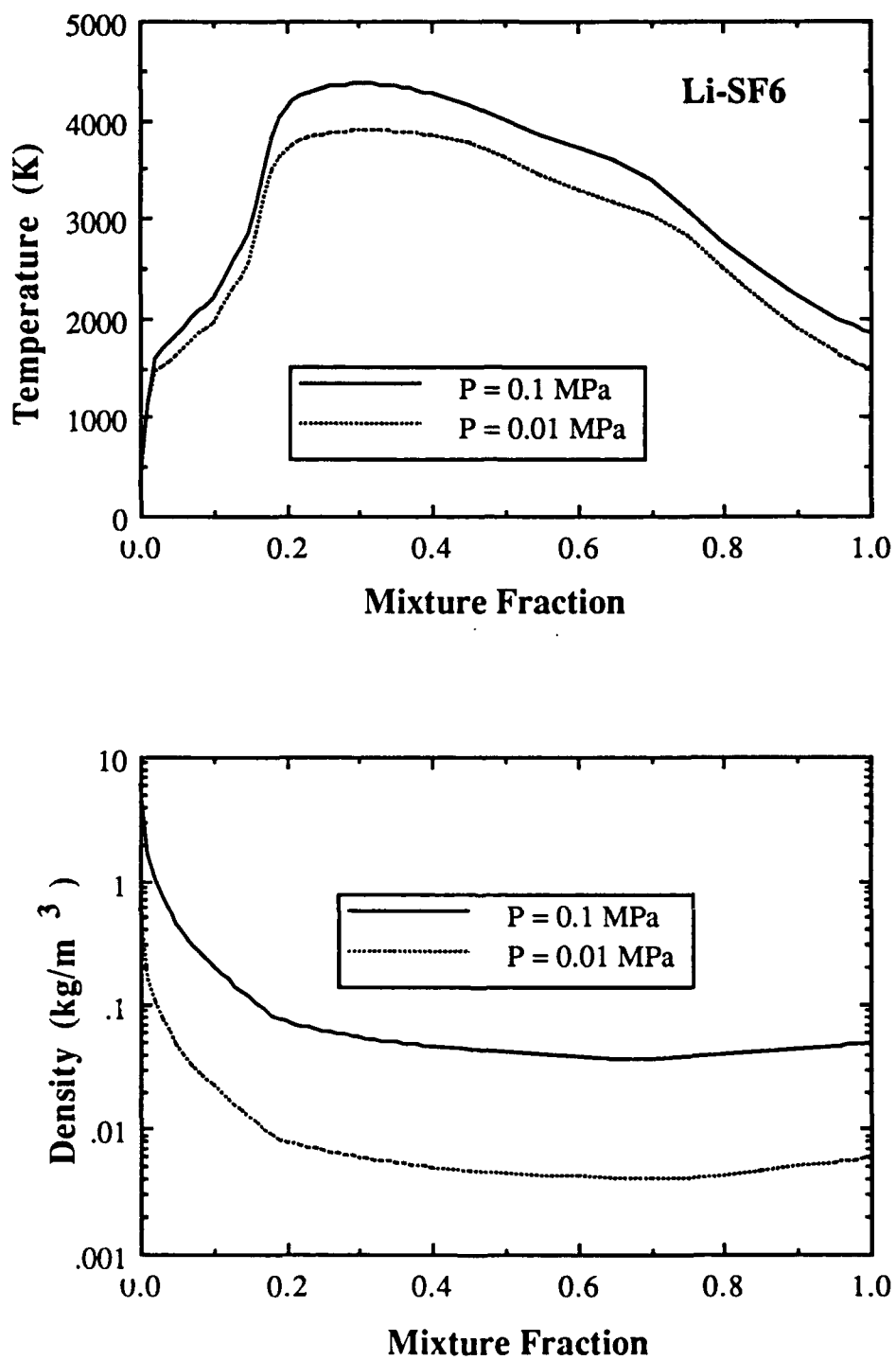


Figure 22. State Relationship of Density and Temperature of Li-SF<sub>6</sub> Wick Combustion

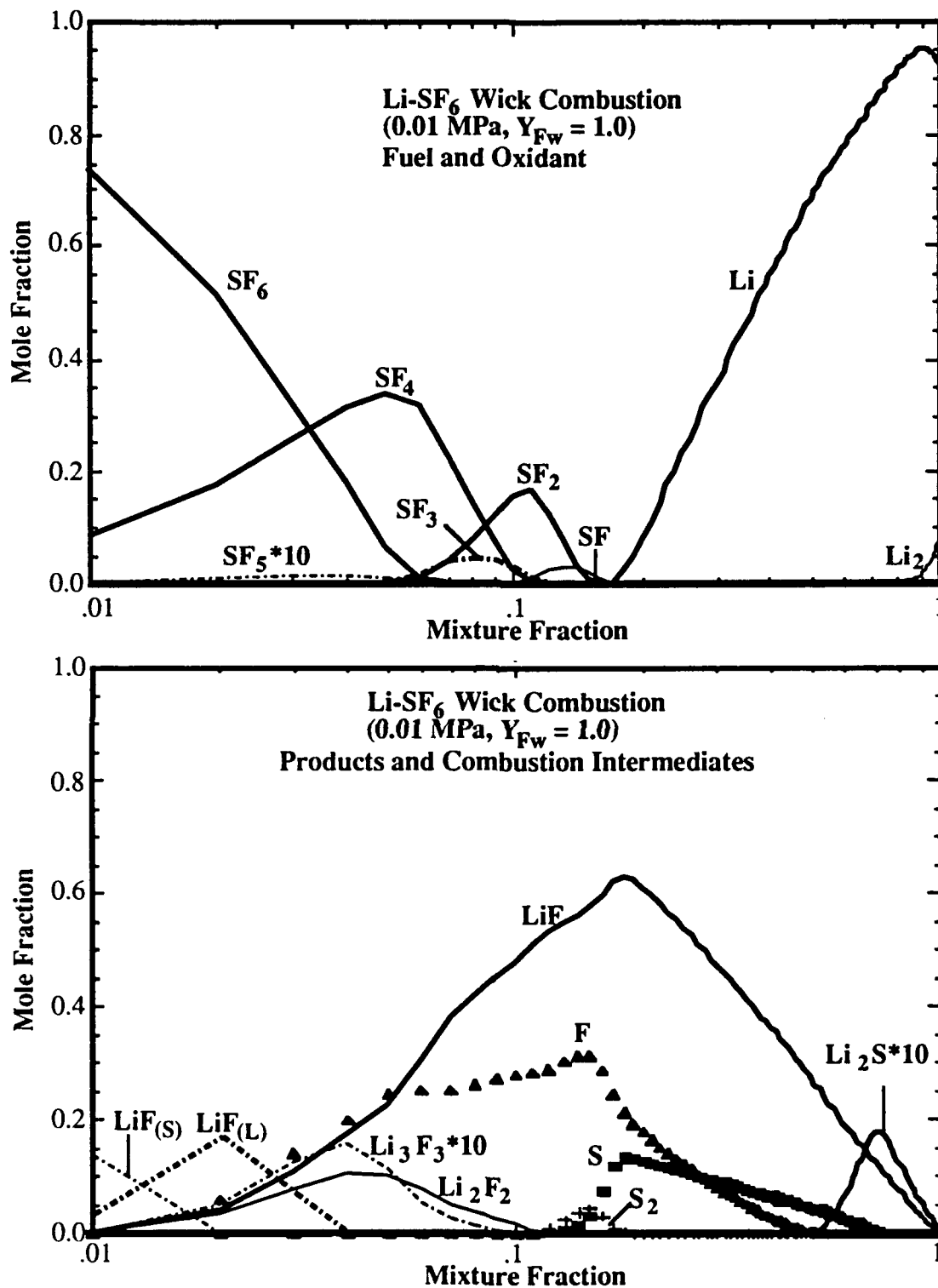


Figure 23. State Relationship of Species Concentration of Li-SF<sub>6</sub> Wick Combustion at 0.01 MPa.

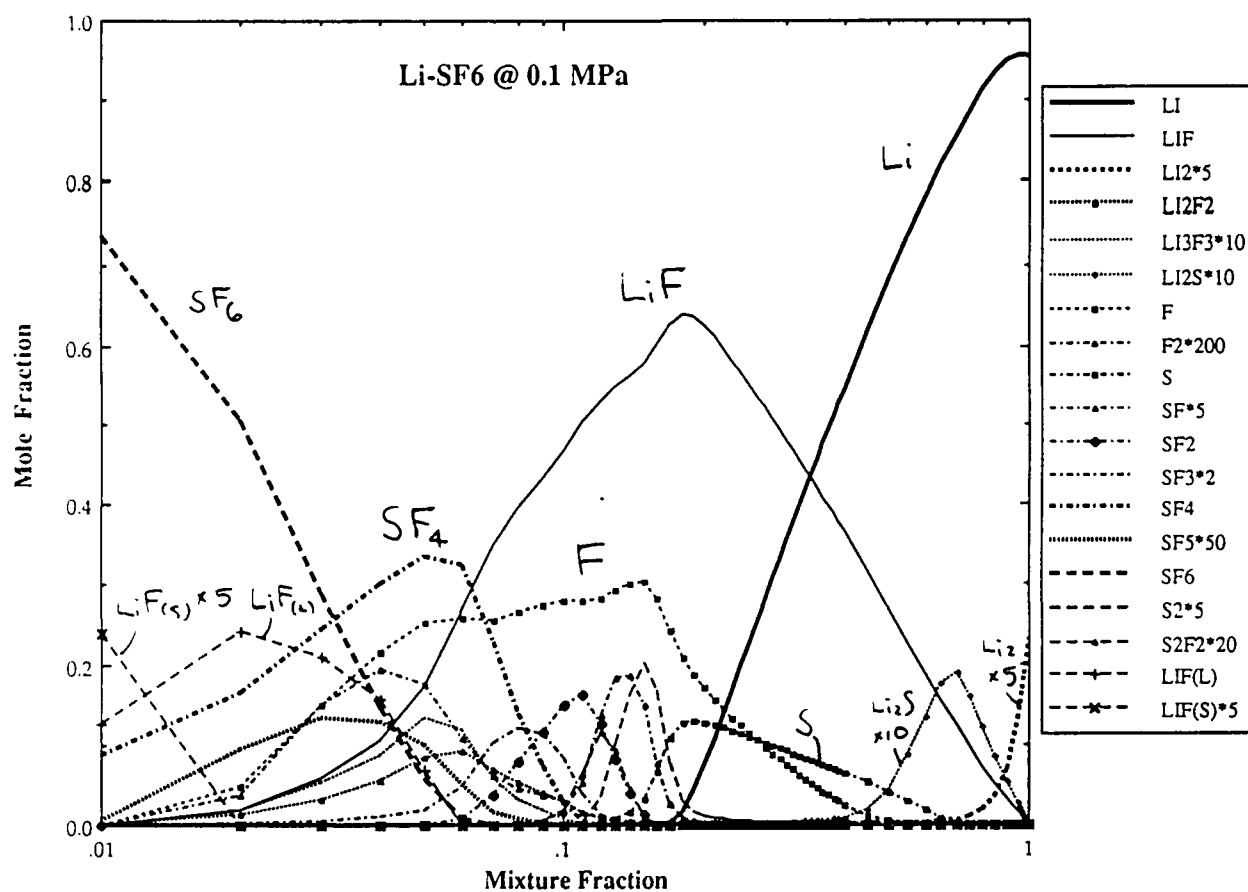


Figure 24. State Relationship of Species Concentration of Li-SF<sub>6</sub> Wick Combustion at 0.1 MPa.

appeared over much of the mixture fraction space while liquid- and solid-phase LiF appeared in the oxidant rich regime. Only gaseous  $\text{Li}_2\text{S}$  in the fuel rich regime was predicted from the equilibrium calculation. The S species appeared as elemental sulfur (S) or  $\text{SF}_x$  ( $x = 1, 2, \dots$ , or 6) in the oxidant-rich regime.

The flowfield solution of Li-SF<sub>6</sub> wick combustion at 0.01 and 0.1 MPa was summarized in Figs. 25 and 26, employing the state relationships shown in Fig. 22. Similar to ethanol-air wick combustion, the prediction showed that similarity profiles prevailed in the flow. For example, nearly identical mixture fraction profiles ( $Z$ ) and dimensionless velocity ( $f$ ) were found at different streamwise locations, cf. Figs. 25 and 26. The pressure was also found to have negligible effects on predicted mixture fraction and dimensionless velocity profiles as one compared the results of 0.01 MPa and 0.1 MPa. The peak dimensionless velocity appeared at  $\eta \approx 1$ , corresponding to the maximum temperature location at which  $Z \approx 0.3$ . The lower pressure condition, i.e. 0.01 MPa, has a higher maximum dimensionless velocity ( $f \approx 0.40$ ) than the 0.1 MPa condition ( $f \approx 0.38$ ). The streamwise flow development was summarized in Figs. 27 and 28. The maximum streamwise velocity increased from 3.8 m/s at  $\xi = 0.22$  ( $x = 0.022$  m) to 8.1 m/s at  $\xi = 1$  ( $x = 0.1$  m) for the condition at 0.01 MPa while the maximum velocity increased from 4.0 m/s ( $\xi = 0.22$ ) to 8.5 m/s ( $\xi = 1.0$ ) for the condition at 0.1 MPa.; it is note that the 0.1 MPa condition had a lower maximum dimensionless velocity (cf. Fig. 26).

The boundary layer thickness grows in the streamwise direction, roughly following a  $x^{0.25}$  dependence similar to that expected for natural convection laminar boundary layer flows. The flame stand-off distance increased as the system pressure was decreased; for example, the stand-off distance at 0.01 MPa was predicted three to four times the value at 0.1 MPa, cf. Figs. 27 and 28. The stand-off distance, however, remained constant over the entire plate in the transformed domain. This confirms the proper similarity transformation used in the analysis. The local wall blowing velocity due to gasification of the liquid was shown in Fig. 29 and the local fuel mass burning rate per unit surface area was summarized in Fig. 30. The wall blowing velocity ( $v_w$ ) was

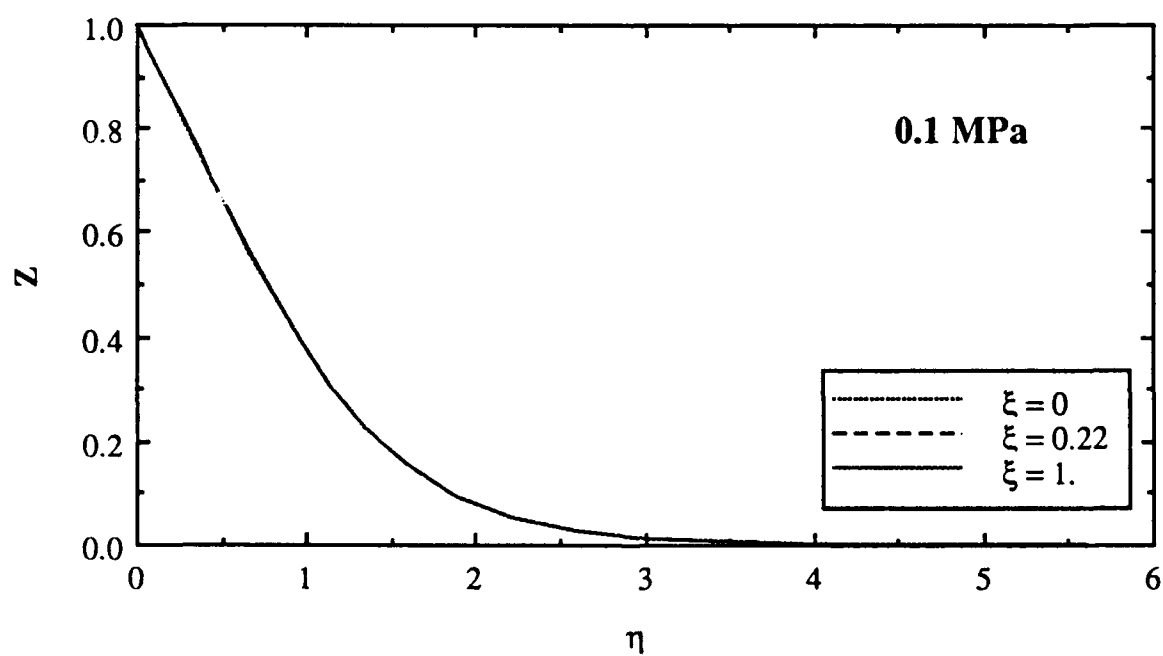
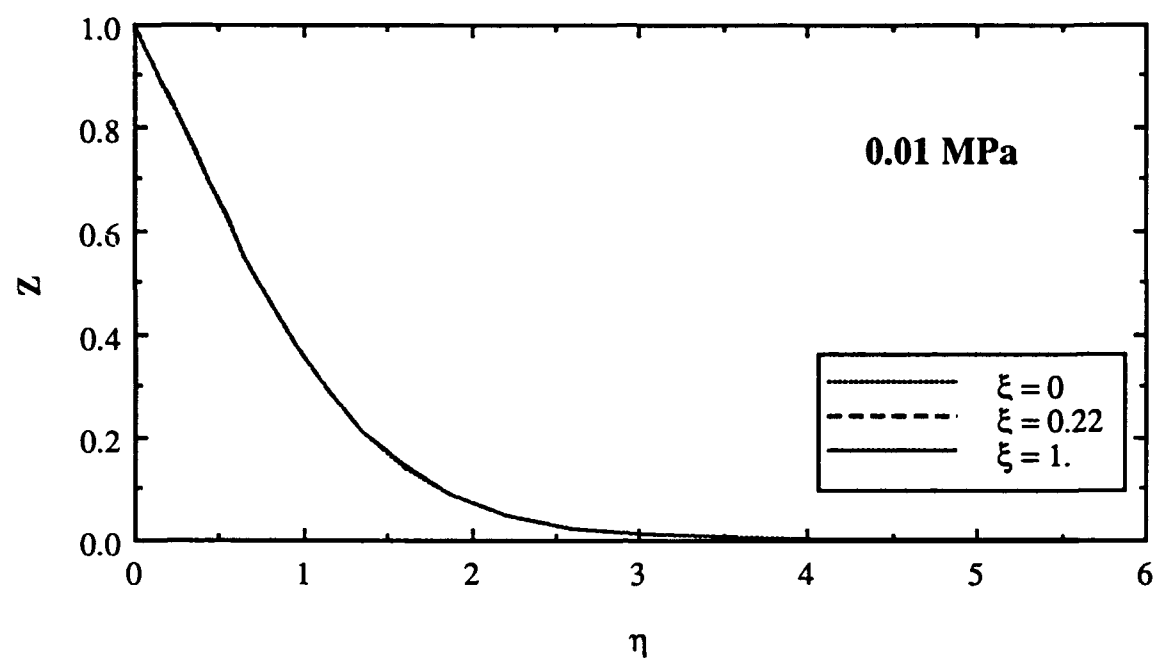


Figure 25. Similarity Mixture Fraction Profiles of Li-SF<sub>6</sub> Wick Combustion

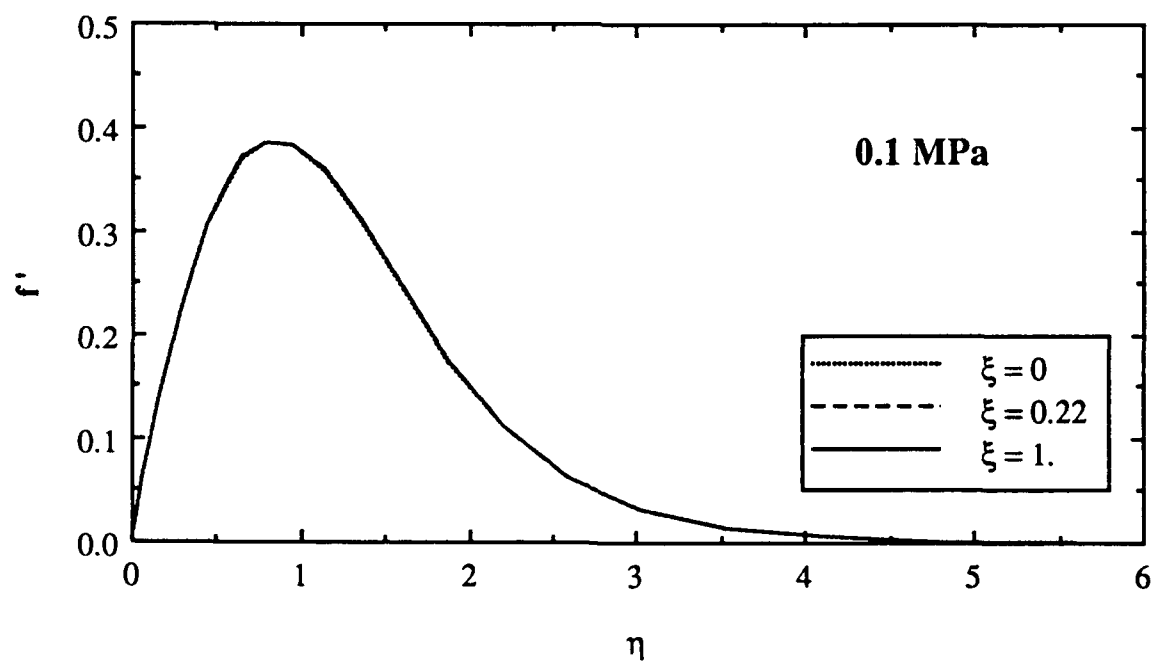
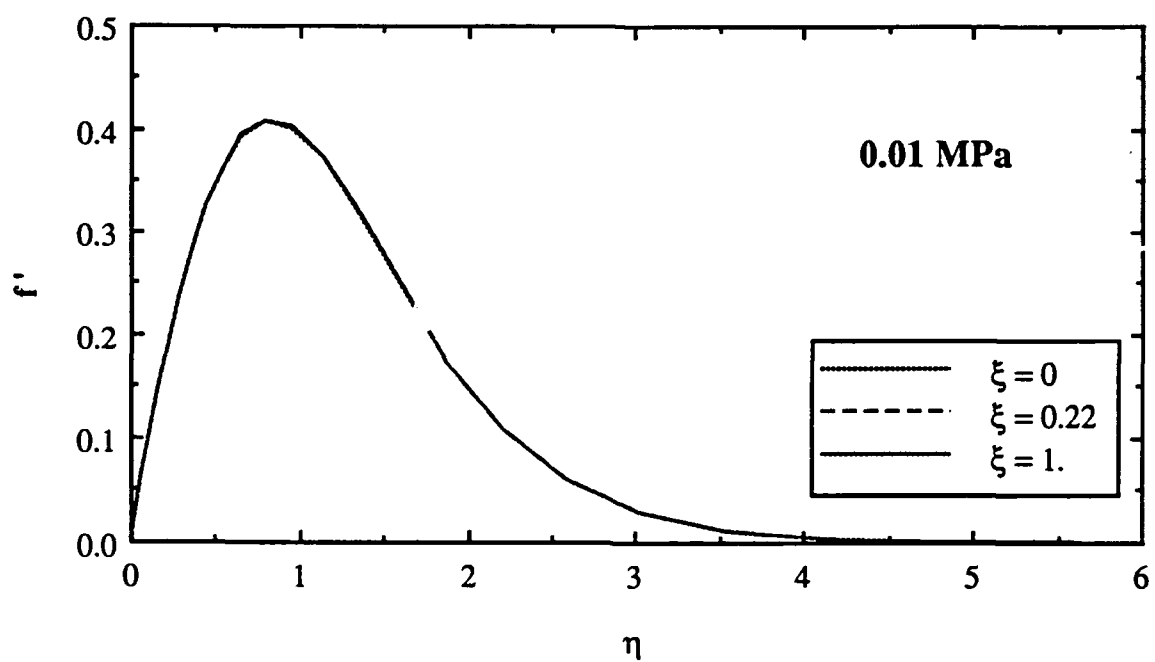


Figure 26. Similarity Velocity Profiles of Li-SF<sub>6</sub> Wick Combustion

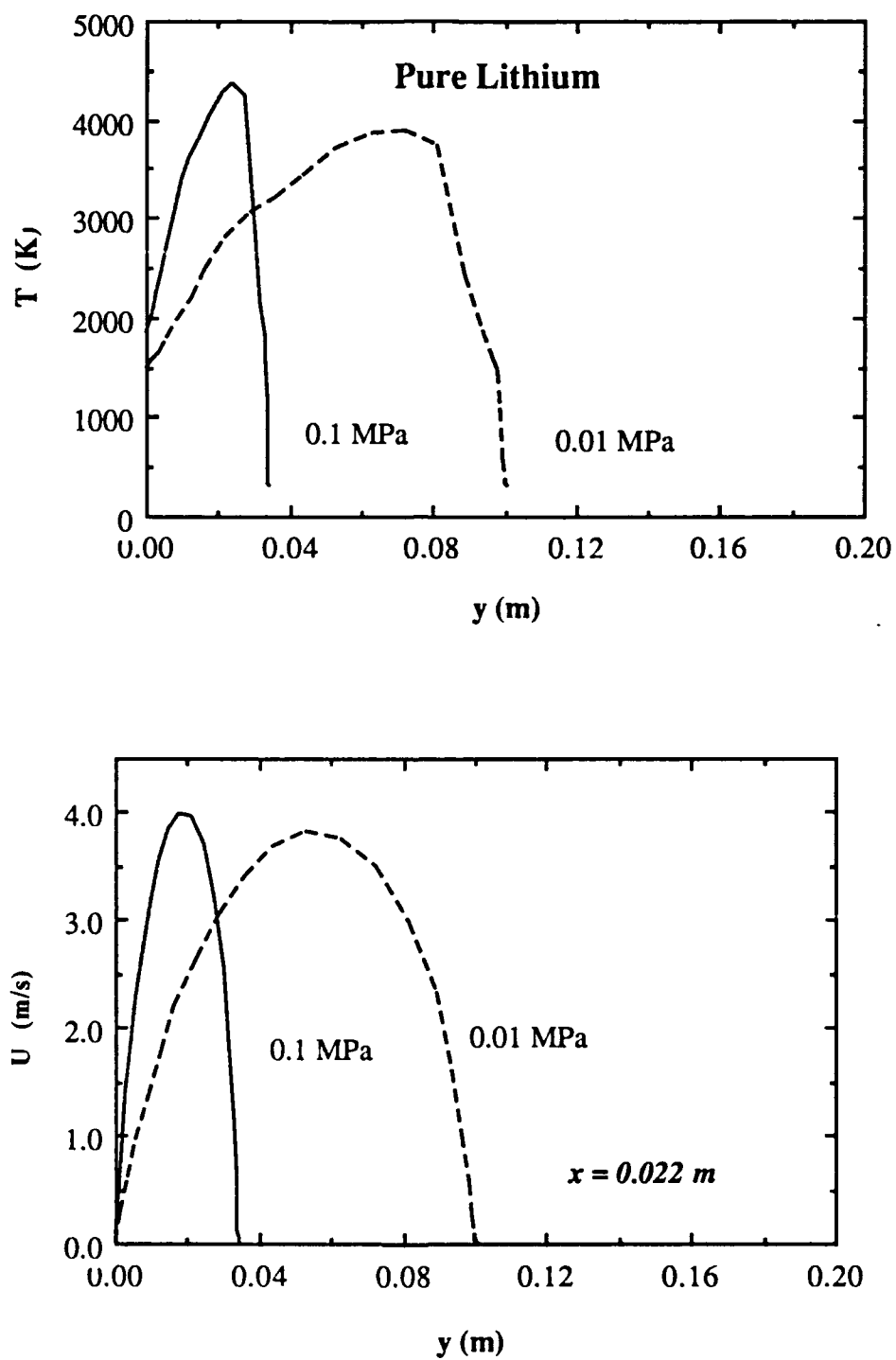


Figure 27. Temperature and Velocity Profiles of Li-SF<sub>6</sub> Wick Combustion at  $\xi = 0.22$



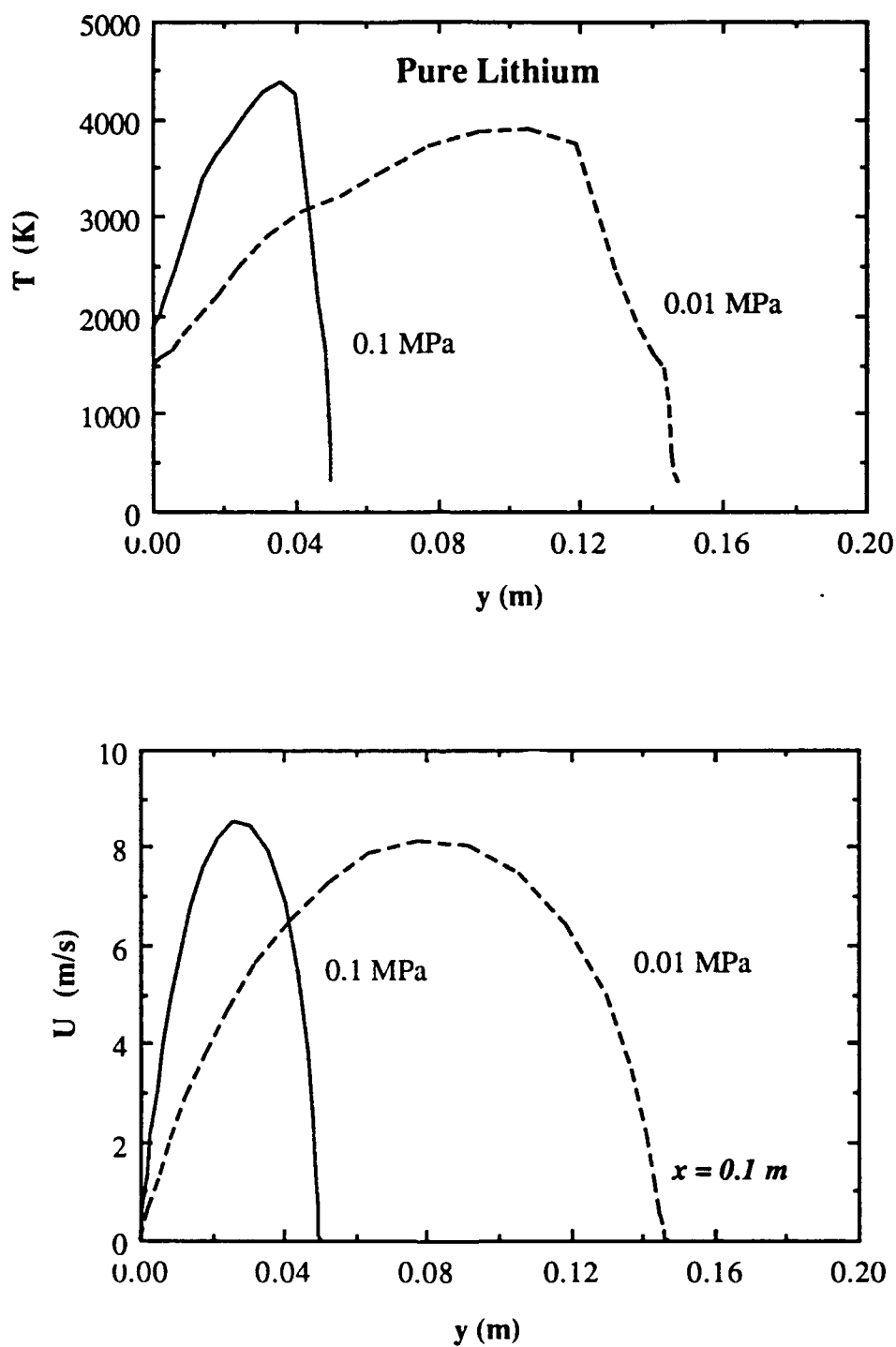


Figure 28. Temperature and Velocity Profiles of Li-SF<sub>5</sub> Wick Combustion at  $\xi = 1$

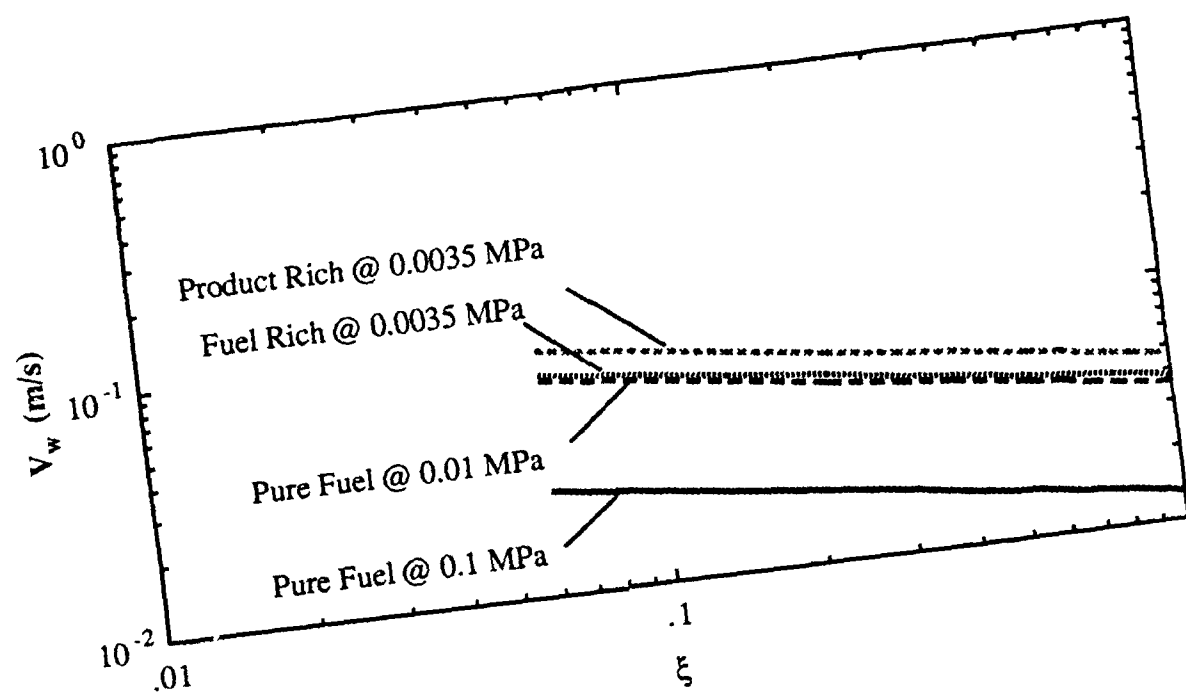


Figure 29. Local Wall Blowing Velocity

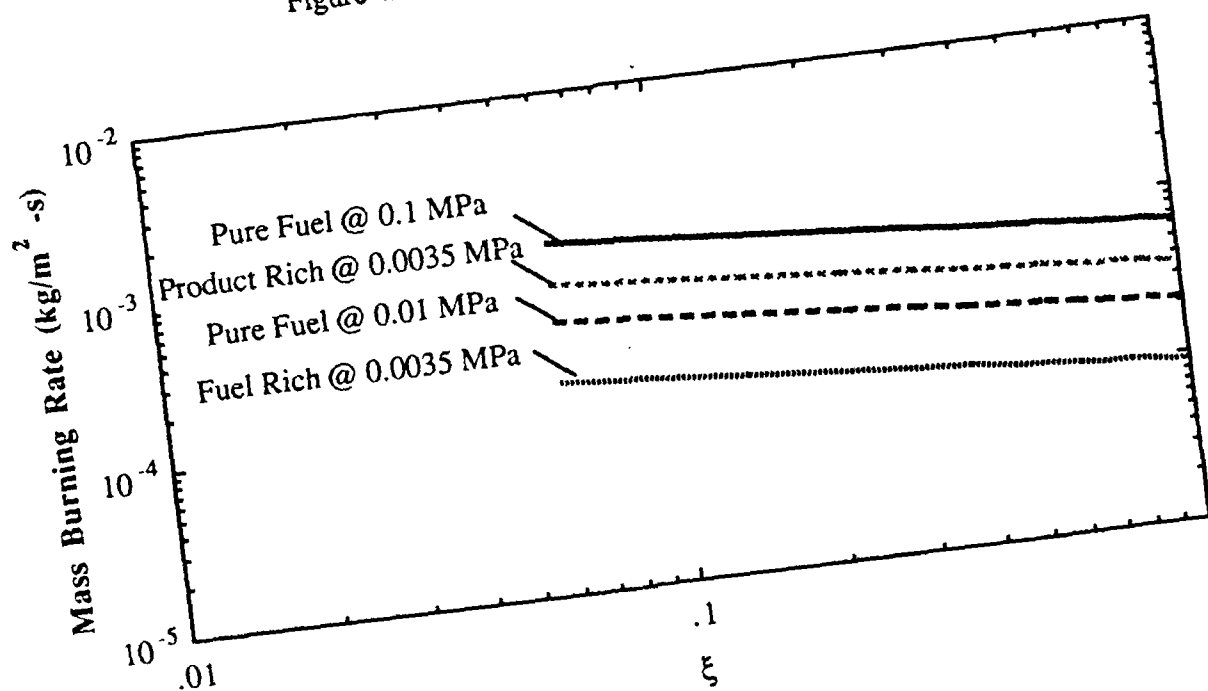


Figure 30. Local Fuel Mass Burning Rate

determined from Eq. (18) and the fuel mass burning rate ( $\dot{m}''$ ) was obtained by multiplying  $v_w$  with local gas density. Both  $v_w$  and  $\dot{m}''$  revealed a  $x^{-0.25}$  dependence, similar to the results obtained for ethanol-air wick diffusion flames, in agreement with the classical results of heat and mass transfer in natural convection laminar boundary layer flows.

Also shown in Figs. 29 and 30 are the results based on the equilibrium properties of fuel-rich and product-rich liquids as fuel. The species composition of the fuel was taken from Groff and Faeth (1978a) for the condition at 0.0035 MPa (1250 K), e.g. see Fig. 31. The enthalpy of gasification was estimated assuming an ideal solution at its proper composition. The predicted mass burning rate decreased as the system pressure was decreased when pure lithium and fuel-rich liquids were considered; it is, however, quite surprising to note that the product-rich condition at 0.0035 MPa yields a mass burning rate higher than that of the fuel-rich condition at 0.0035 MPa and that of pure lithium at 0.01 MPa (cf. Fig. 30). The higher mass burning rate is a result of the increased heat transfer from the flame to the wick surface as the flame stand-off distance decreases when the initial Li mass fraction was decreased. The higher mass burning rate is also a result of reduced enthalpy of gasification per unit mass of the liquid, e.g. 21228 kJ/kg for pure Li 1609 K, 21950 for pure Li at 1339 K, and 21631 kJ/kg for pure Li, 19572 kJ/kg for fuel-rich liquid and 8381 kJ/kg for product-rich liquid at 1250 K. The higher mass burning rate does not imply a higher Li consumption rate since only little Li was present in the product-rich fuel. The results, however, suggest that the wick configuration may have the potential to achieve a higher fuel utilization than the submerged jet operation.

An interface analysis is established (Lyu, 1991) which allows for polymerization of fuel and products and the presence of condensed phase products at the interface. The predicted interface temperature is in agreement with the liquid bath temperature of Li and SF<sub>6</sub> wick combustion (Lyu, 1991). The interface analysis also yields a high combined mole fraction of Li and Li<sub>2</sub> in the gas phase, suggesting that the liquid bath temperature is determined by the system pressure. This is in agreement with the experiments of Li-SF<sub>6</sub> wick and submerged jet combustion. The flow

calculation based on the complex interface condition is reported in Lyu (1991). The predicted flow characteristics are qualitatively similar to those assuming a pure lithium at the interface ( $Y_{\text{Li}} = 1$ ).

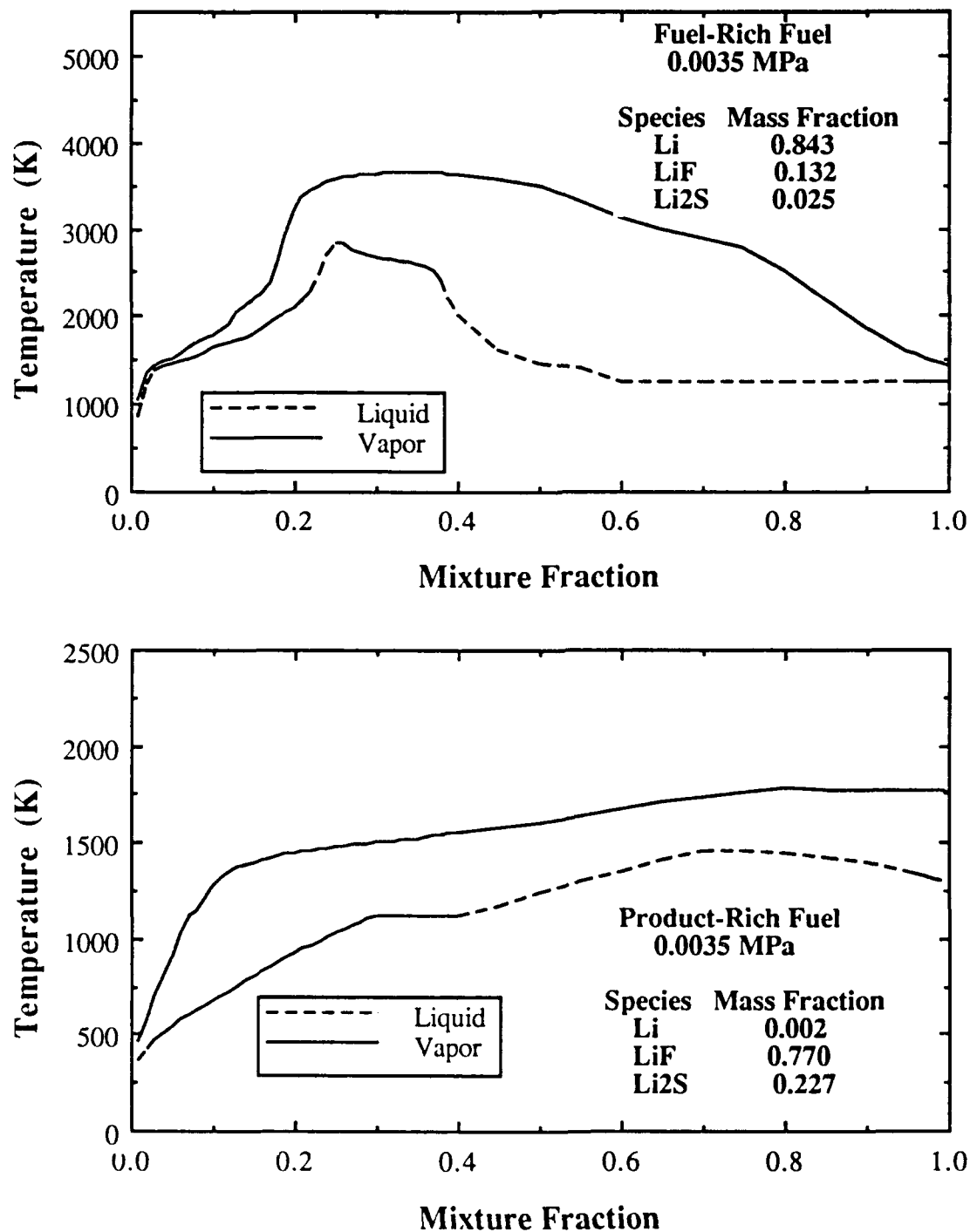


Figure 31. State Relationship of Fuel-Rich and Product Rich Fuels

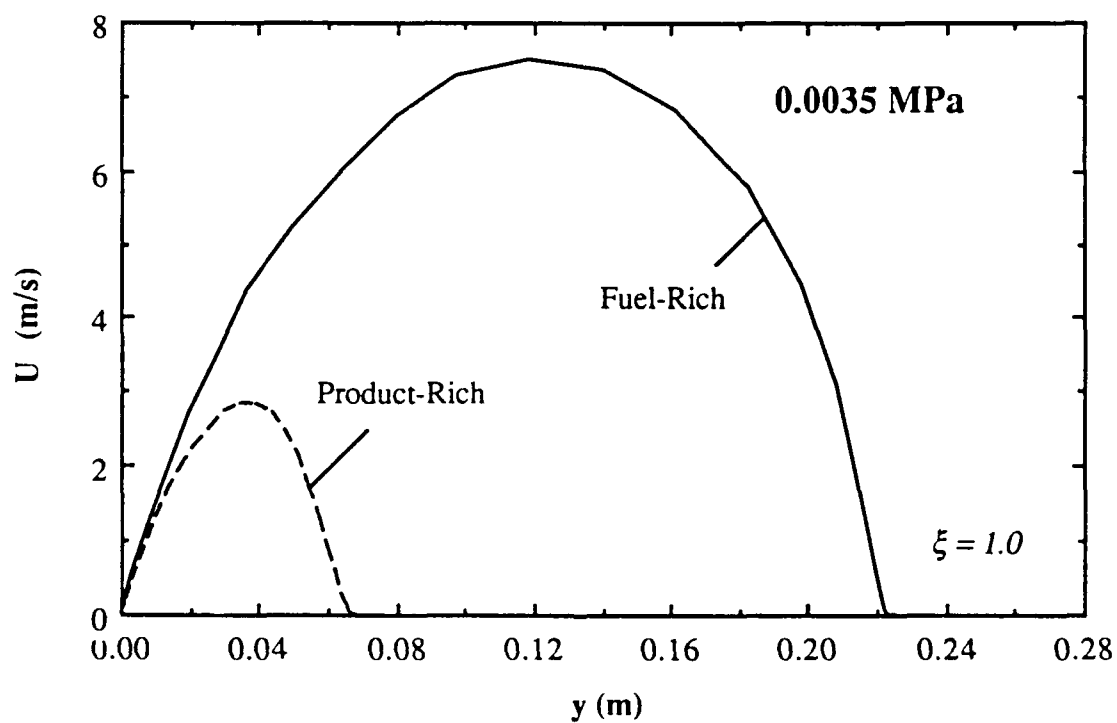
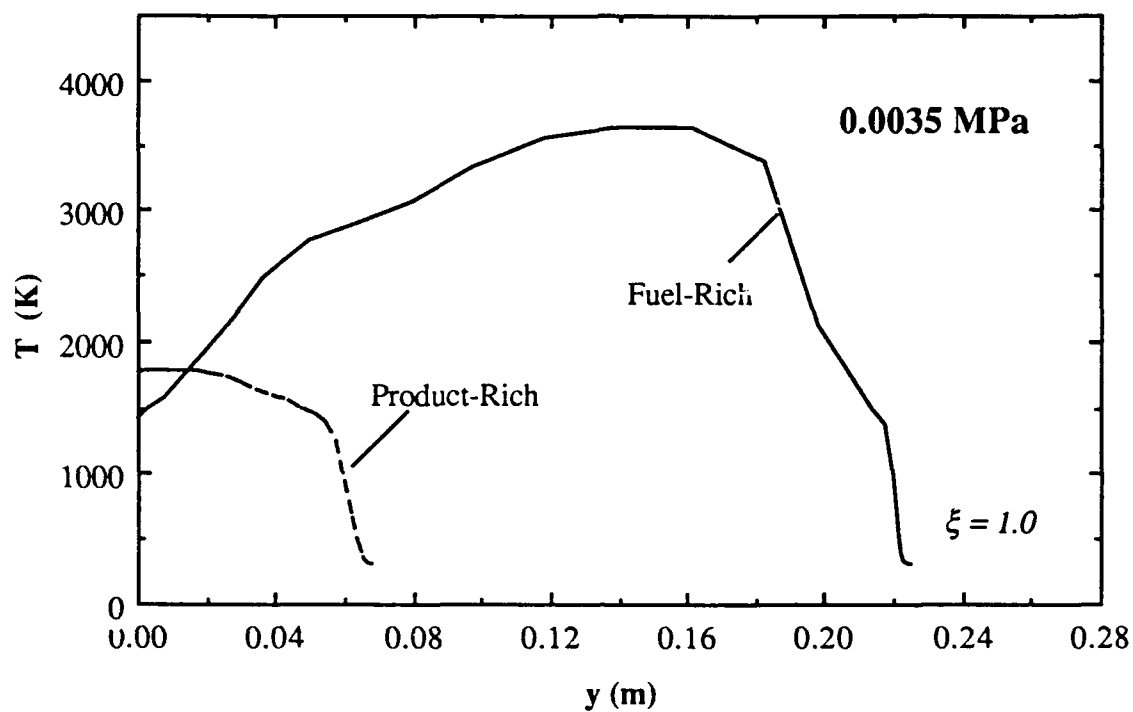


Figure 32. Li-SF<sub>6</sub> Wick Combustion of Fuel-Rich and Product-Rich Fuel at 0.0035 MPa.

#### 4.4 Emission Spectrum and Temperature Measurements

Scanning Spectrum Measurements. Wick combustion of Li and SF<sub>6</sub> yields a bright pinkish flame around the wick cylinder. The emission spectrum in the visible regime of 400 to 680 nm is summarized in Fig. 17. Six emission line are identified. It is believed that this is the first emission spectrum of Li-SF<sub>6</sub> combustion reported in the literature.

The six emission lines are centered at wavelengths of 413.26, 427.31, 460.29, 497.17, 610.36 and 670.78 nm, representing the electronic transitions of lithium atoms from states 5d to 2p, 5s to 2p, 4d to 2p, 4s to 2p, 3d to 2p, and 2p to 2s, respectively. The strongest emission line is the resonance doublet centered at 670.78 nm, due to ground state transitions. In fact, these emission lines represent all the emission lines of lithium atoms in the wavelength regime of 400 to 700 nm as identified, for example, by Herzberg (1944). There are eight emission lines of lithium atoms below 400 nm: 398.5 nm (6s-2p), 391.5 nm (6f-2p), 383.8 nm (7s-2p), 379.4 nm (7d-2p), 323.2 nm (3p-2s), 274.1 nm (4p-2s), 256.2 nm (5p-2s), and 247.5 nm (6p-2s), and three above 680 nm: 812.6 nm (3s-2p), 1278.2 nm (5f-3d), and 1869.7 nm (4f-3d), cf. Herzberg (1944).

Simultaneous Spectrum Measurements. There are five sets of spectrum images taken by the image intensified CCD camera for wick combustion of Li and SF<sub>6</sub>. Each set of the image consists of two sequential measurements as described earlier. The measured spectrum shows four spectral lines centered at 413, 427, 460 and 497 nm, resulting from the spontaneous emission of lithium atoms. The spectral lines centered at 460 nm and 497 nm are used to estimate the flame temperature. The other two lines, i.e. the ones centered at 413 and 427 nm, are rather weak and not used in the analysis for temperature measurements. A long-tailed wing was observed for the 460 nm line which may result from the diffuse band of lithium dimmers (cf., Bahns et al., 1988). The spatial profiles of the raw data (spatially integrated intensities) for the emission lines centered at 460 nm and 497 nm are shown in Figs. 33 to 37. In the figures, "460.x.y" and "497.x.y" denotes the spectral measurements for 460 nm and 497 nm, respectively, taken at event number *x* set and sequential number *y*. Even number 1 represents the first set of the spectrum taken after

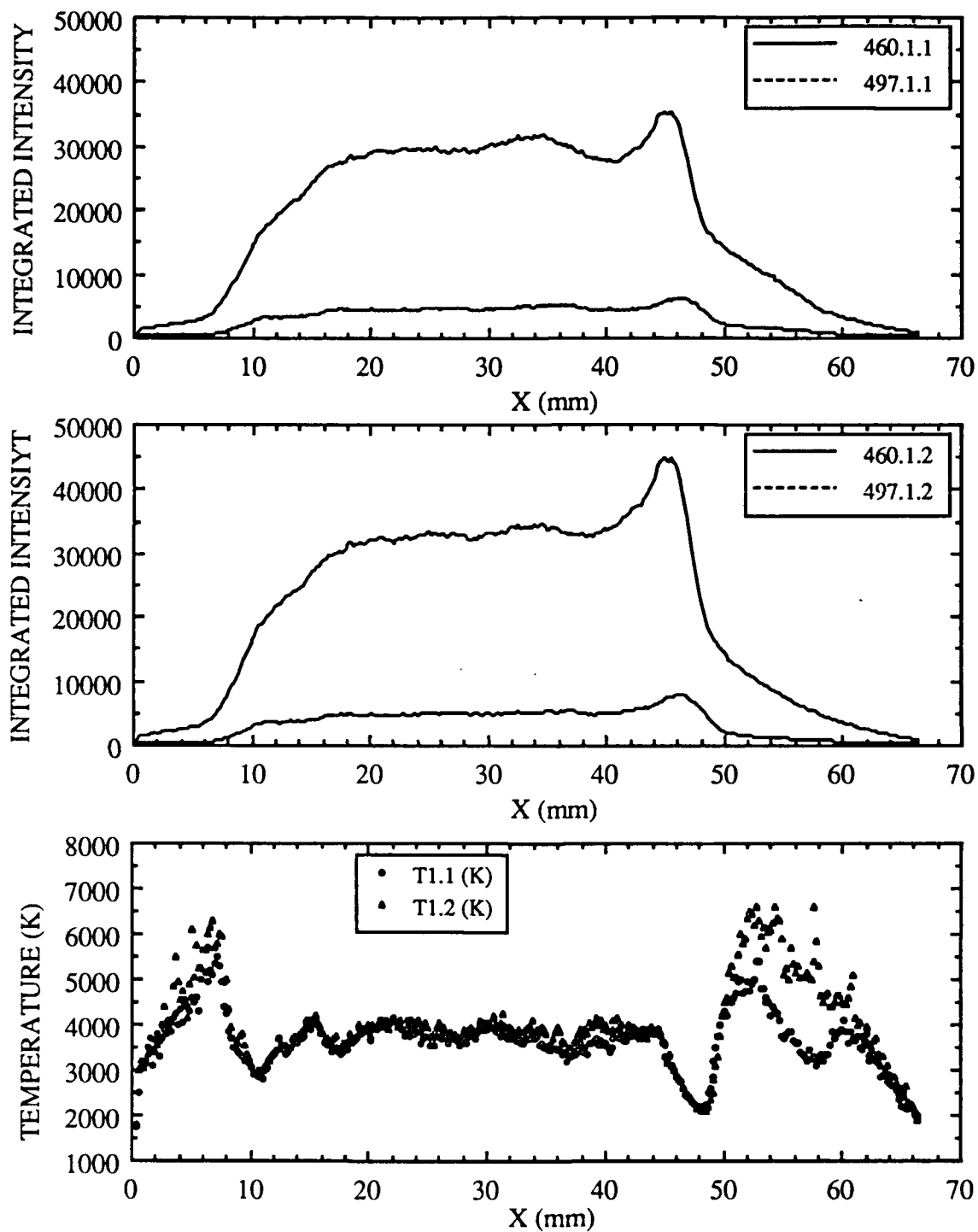


Figure 33. Spatial Profiles of Integrated Intensities, Event No. 1.

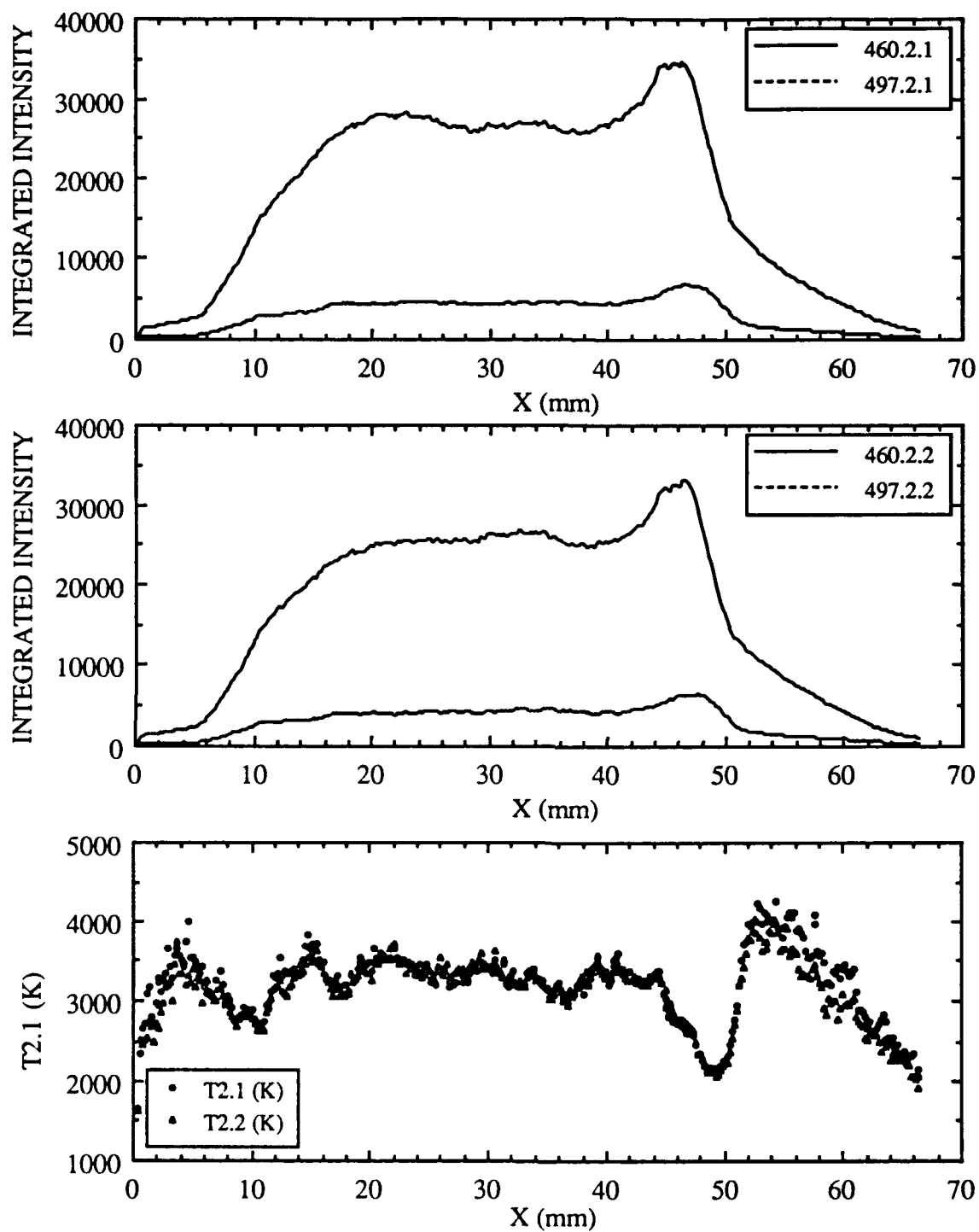


Figure 34. Spatial Profiles of Integrated Intensities, Event No. 2.



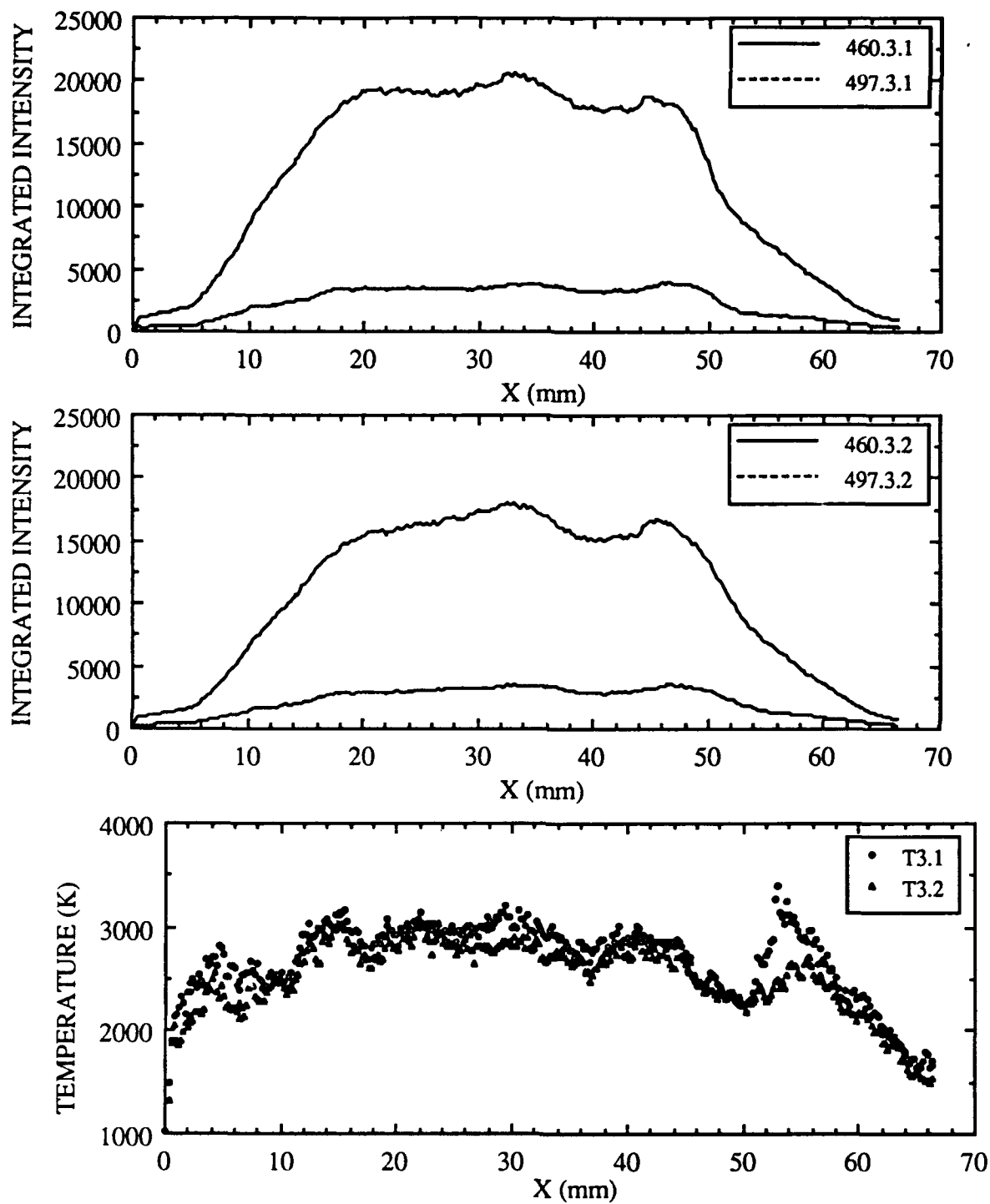


Figure 35. Spatial Profiles of Integrated Intensities, Event No. 3.

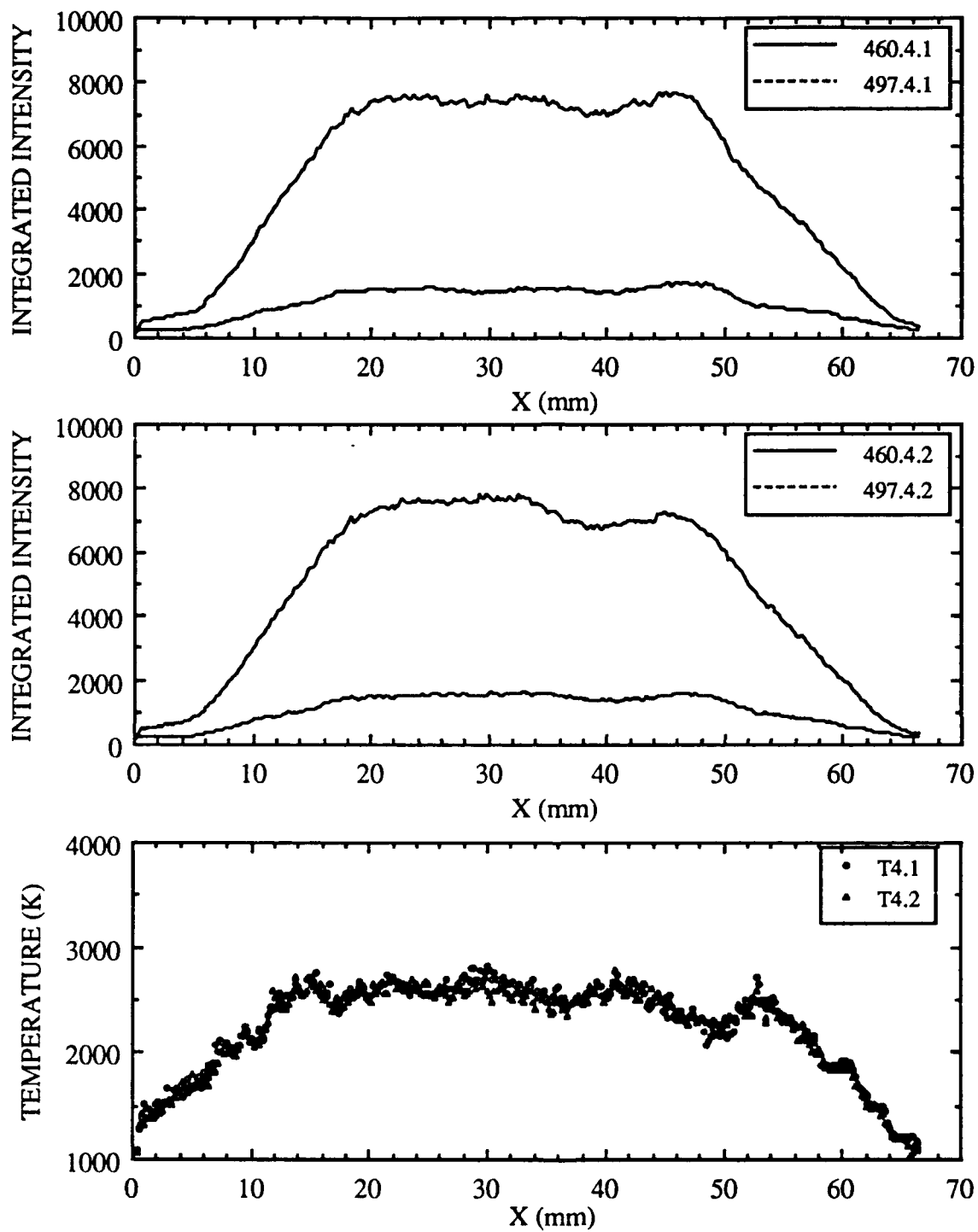


Figure 36. Spatial Profiles of Integrated Intensities, Event No. 4.

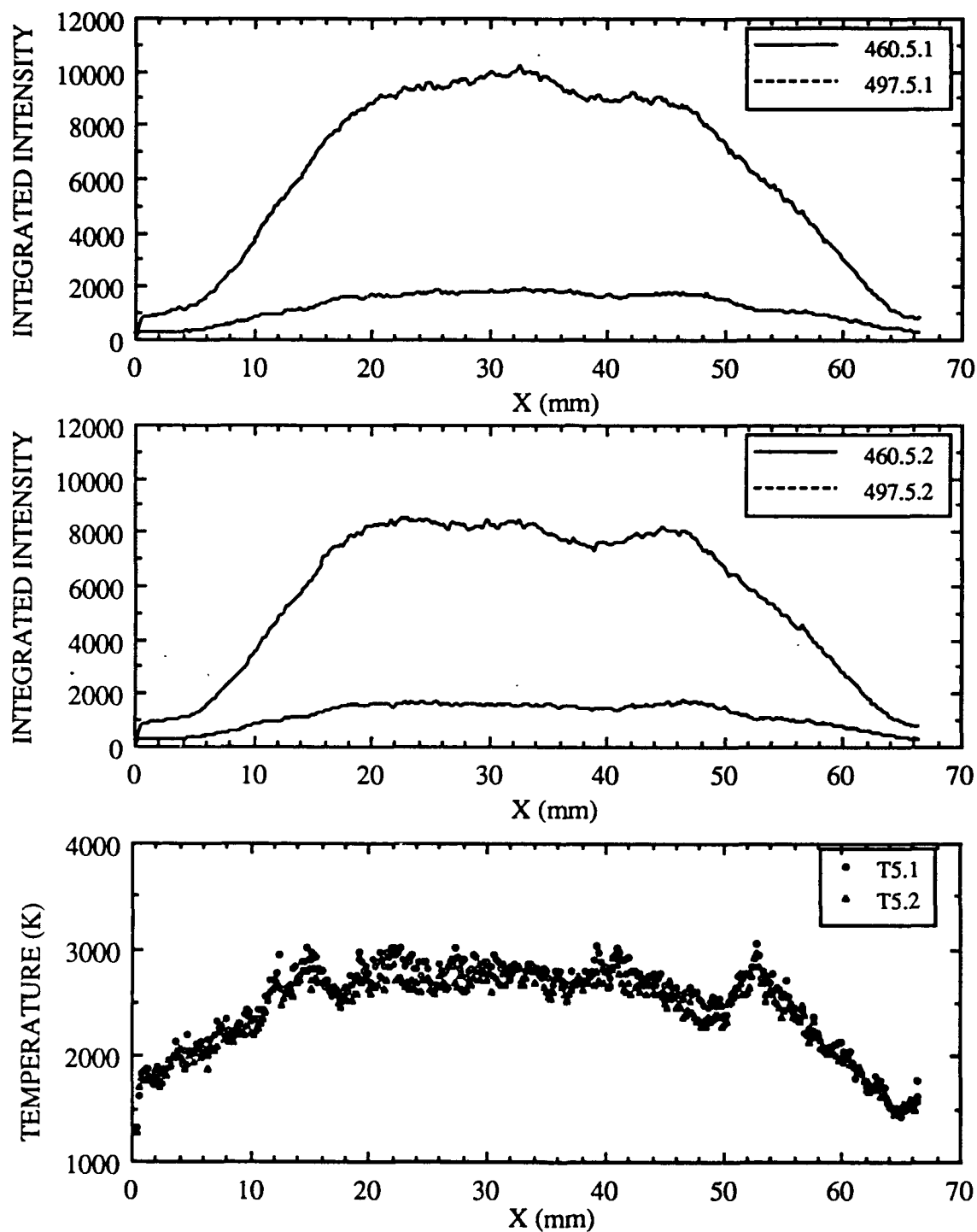


Figure 37. Spatial Profiles of Integrated Intensities, Event No. 5.

ignition. The intensity profiles became weaker when combustion proceeds; probably, a result of the attenuation due to formation of condensed products in the flow field. An asymmetry in intensity profiles is also observed, most evident in the results shown in Figs. 33 and 34. It should be noted that Figs. 33 and 34 are taken during the initial stage of combustion when a stable flame has not been established. The asymmetry is reduced as time proceeds, e.g. see Figs. 36-37.

The temperature profiles calculated by the ratio of integrated intensities centered at 460 nm and 497 nm are also shown in Figs. 33 to 37. The temperature profiles showed two dips located near the locations of 18 mm and 50 mm, respectively; coincidental with the wick diameter- recall that the wick diameter is 32 mm. The wick boundary can also be observed from the intensity profiles where the intensity starts to decrease toward both ends. The intensity varies within the wick boundary (18 mm to 50 mm). Several factors may attribute to this variation, for example, the asymmetry in the flame, and the reflection or emission from the wick surface. The temperature increases moving away from the wick surface and peaks at about 4 mm away from the wick surface. The luminous flame location, however, can not be accurately identified from the video image (Hsu and Chen, 1991). The peak temperature deviates from image to image. A peak temperature ranging from 2500 to 3500 K is obtained from the data summarized in Figs 38-42. An error of 500 K at a temperature of 3000 K is calculated, assuming a 10 % error in measurements and in estimating the constants for Eq. (35). It should be noted that a good signal-to-noise ratio is usually obtained for the intensity profiles in the region bounded by 8 mm and 60 mm.

The radial intensity profiles,  $I(r)$ , are also calculated from the raw data shown in Figs. 33-37. The temperature profiles are subsequently calculated from the curve-fitted radial intensities. Due to the complexities in data reduction, preliminary temperature measurements are reported in this report. More detailed description will appear in Hsu (1991). The temperature profiles based on the inversed radiance measurements of Events 3 and 4 are shown in Figs. 38 and 39 for the left and right sides of the wick, respectively. The radial location of  $r = 16$  mm is the boundary of the wick surface. The solid lines are best-fits of the temperature calculated from the inversed radiance

(shown as triangles); the temperatures based on the integrated radiance are also shown in the figures by the squares. It is evident that the peak temperature appears at 5 to 6 mm away from the wick surface, or  $21 \leq r \text{ (mm)} \leq 22$ . The peak temperature is around 3500 K for Event 3 and 3000 K for Event 4.

Work is in progress to obtain spatially-resolved temperature measurements by further examining the radiance and to apply the thermally-assisted two-photon LIF technique. Although the experimental set-up and instrumentation has been established for using the CCD camera in conjunction with a gated image intensifier. The LIF measurements are required for a definitive evaluation on the experimental uncertainties associated with the radiance measurements.

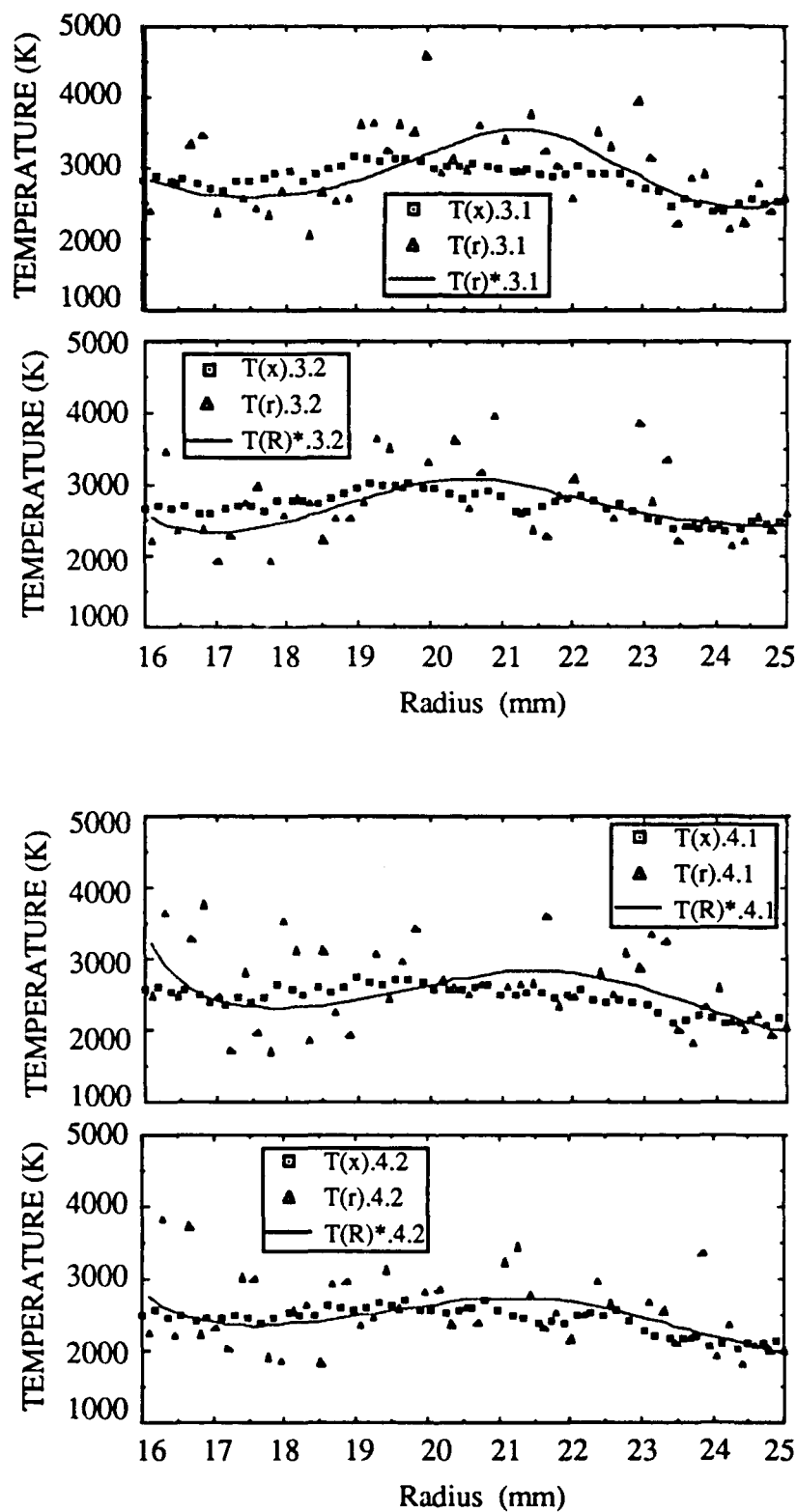


Figure 38. Temperature Profile Calculated from Inversed Intensity; Left-Side of the Wick.

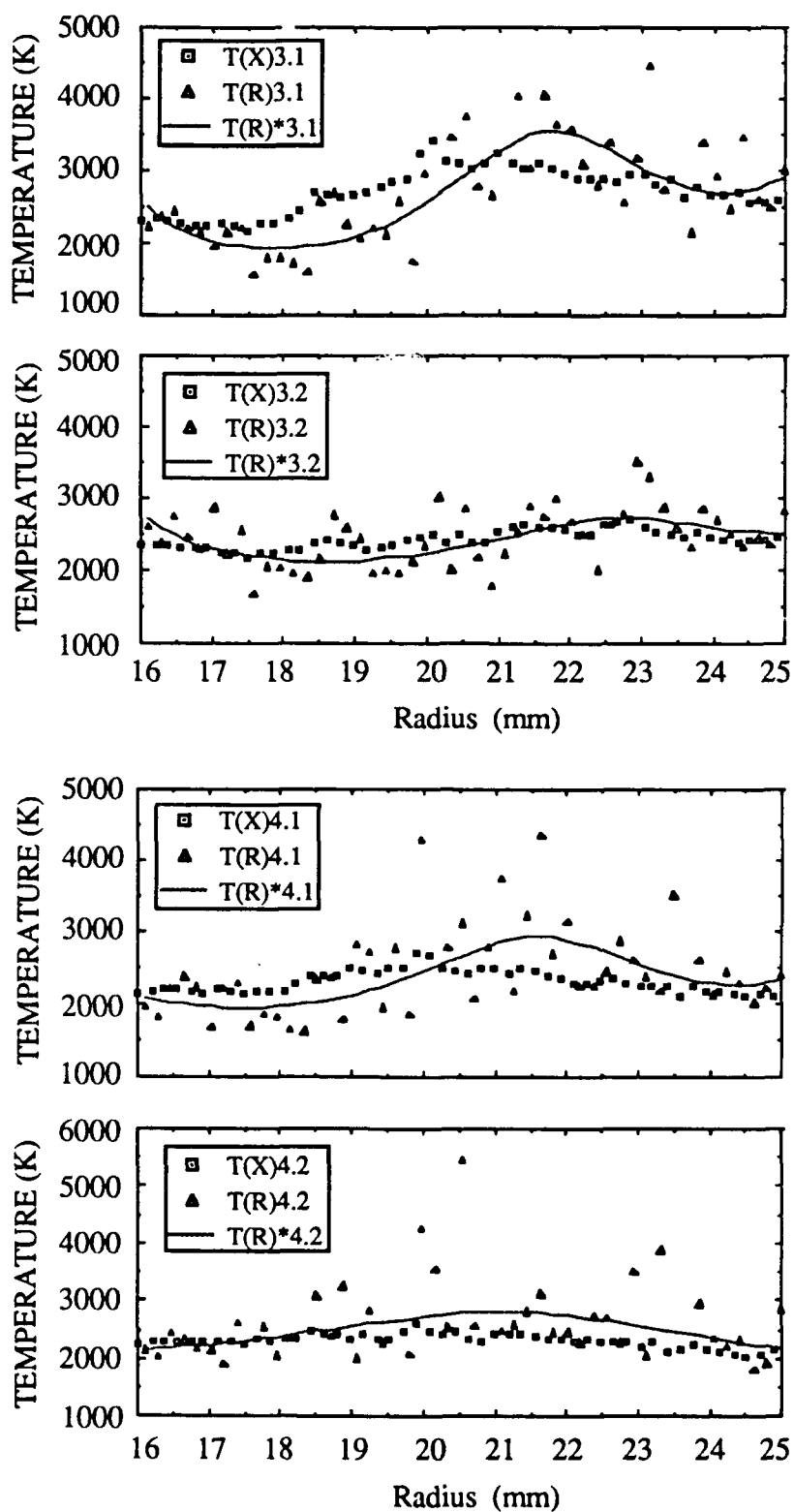


Figure 39. Temperature Profile Calculated from Inversed Intensity; Right-Side of the Wick.

## V. SUMMARY AND CONCLUSIONS

An experimental and theoretical investigation was conducted to study wick combustion of Li-SF<sub>6</sub>. A single-line laser induced fluorescence (LIF) thermometry technique with Li<sub>2</sub> as fluorescence species was developed and calibration experiments showed promising results. Refinements, however, are needed for combustion flame measurements. Wick combustion of ethanol and hexane in air as well as Li and SF<sub>6</sub> was conducted in a vacuum chamber at atmospheric and sub-atmospheric pressures. The ethanol and hexane wick diffusion flames showed flame oscillations, similar to flame flickers in buoyant jet diffusion flames. The oscillation frequency was estimated in the range of 5 to 8 Hz at the pressures examined. The flame stand-off distance was found to increase when the system pressure was decreased. The wick combustion of Li and SF<sub>6</sub> results in a bright pinkish flame. The spontaneous emission spectrum is determined for the first time in the literature. The emission spectrum shows that the flame luminosity is dominated by the resonance emission-line of Li atoms.

To model Li-SF<sub>6</sub> wick diffusion flames, Li<sub>2</sub>S thermochemical properties are established following Groff (1976). The Li<sub>2</sub>S thermodynamic properties are rearranged to the format employed in the NASA CEC equilibrium code (Gordon and McBride, 1976). The NASA CEC equilibrium code is employed to obtain the flame properties of Li-SF<sub>6</sub> wick combustion. An interface analysis is established which allows for polymerization of fuel and products and the presence of condensed phase products at the interface (Lyu, 1991 and Lyu et al., 1991). The predicted interface temperature is in agreement with the liquid bath temperature of Li and SF<sub>6</sub> wick combustion. The interface analysis also yields a high combined mole fraction of Li and Li<sub>2</sub> in the gas phase, suggesting that the liquid bath temperature is determined by the system pressure. This is in agreement with the experiments of Li-SF<sub>6</sub> wick and submerged jet combustion. Similarity solutions are obtained for flat-plate Li-SF<sub>6</sub> wick diffusion flames, analogous to that of flat-plate ethanol-air wick flames. Curvature effects, however, are more pronounced in the Li-SF<sub>6</sub> wick diffusion flames, suggesting that the curvature effects of reactive flows are flow dependent, or



being flame structure dependent. A parametric study on the property effects is conducted. The results showed that the property variation is extremely important to accurate estimates of the fuel burning rates and of the flame stand-off distance. The most severe assumption is the Chapman gas assumption. The effects on mass burning rates due to fuel composition variations were studied employing fuel-rich and product-rich liquids at 0.0035 MPa in the analysis. It was found that the product-rich fuel yields a much lower flame temperature; the mass burning rate, however, was higher than the pure lithium at 0.01 MPa. The findings on fuel mass burning rates are interesting, suggesting that the wick configuration may achieve a higher fuel utilization than the submerged jet, provided the product-rich liquid has a sufficient surface tension for capillary transport of the fuel.

Simultaneous spectrum measurements of the wick combustion of Li and SF<sub>6</sub> are obtained using an image intensified CCD camera. The flame temperature is determined from the inversion of the radiance registered by the CCD camera. A peak temperature of 3000 to 3500 K has been identified. Further work to refine the measurements is suggested; namely, the thermally assisted two-photon LIF measurements of Li atoms and the uncertainty analysis of radiance measurements.

## REFERENCES

- Alstadt, R. H. and Faeth, G. M., 1977, "An Investigation of Wick-Type Metal Combustors," Technical Report to DARPA (DARPA Contract No. N00600-74-C-0033), The Pennsylvania State University.
- Avery, J. F. and Faeth, G. M., 1975, "Combustion of a Submerged Gaseous Oxidizer Jet in a Liquid Metal", *15th Symp. Combust.(International)*, The Combustion Institute, pp. 501-512.
- Bilger, R. W., 1980, "Turbulent Flows with Non-premixed Reactants", in *Turbulent Reacting Flows* (P. A. Libby and F. A. Williams, Ed.), Springer-Verlag, pp. 65-114.
- Blakeslee, T. R., 1977, "Laminar Free-Convective Combustion of a Liquid Metal from a Wick", Ph.D. dissertation, The Pennsylvania State University.
- Chase, M. W., Jr., Davies, C. A. Downey, J. R., Jr., Frurip, D. J., McDonald, R. A. and Syverud, 1985, *JANAF Thermochemical Tables*, 3rd Ed., Part I and II, ACS/AIP.
- Chen, L.-D. and Faeth, G. M., 1981, "Ignition of a Combustible Gas along Heated Vertical Surfaces", *Combust. Flame*, Vol. 42, pp. 77-92.
- Chen, L.-D. and Faeth, G. M., 1982, "Ignition of Supercritical Fluids During Natural Convection from a Heated Vertical Surface," *Combust. Flame*, Vol. 44, pp. 169-183.
- Chen, L.-D. and Faeth, G. M., 1983, "Structure of Turbulent Reacting Gas Jets Submerged in Liquid Metals", *Combust. Sci. Technol.*, Vol. 31, pp. 277-296.
- Colodner, P., Winterfield, C., and Yablonovitch, Y., 1977, *Opt. Commun.*, Vol. 20, p. 119.
- Faeth, G. M., Groff, E. G., You, H-Z., Alstadt, R., and Icenhower, D., 1978, "A Reactive-Heat-Pipe for Combined Heat Generation and Transport", *Proceedings of 3rd International Heat Pipe Conference*, Palo Alto, CA, 22-24 May 1978.
- Flower, W. L. and Bowan, C. T., 1984, "Measurements of The Structures of Sooting Laminar Diffusion Flames at Elevated Pressures", *20th Symp. Combust.(International)*, The Combustion Institute, pp. 1035-1044..
- Gordon, S. and McBride, B. J., 1976, "Computer Program for Calculation of Complex Chemical Equilibrium," NASA SP-273, NASA.
- Ginzburg, I. P., Surin, V. A., Bagautdinov, A. A., Grigor'yants, A. S., and Shub, L. I., 1977, "Study of the Discharge Process into a Liquid of a Gas Stream from an Immersed Nozzle", *J. Engineering Physics*, Vol. 33, pp. 879-887.
- Groff, E. G., 1976, "Characteristics of a Steadily Operating Metal Combustor," Ph. D. Dissertation, Pennsylvania State University.
- Groff, E. G. and Faeth, G. M., 1978a, "Phase Equilibria in the Li-LiF-Li<sub>2</sub>S Systems", *Ind. Eng. Chem. Fundam.*, Vol. 17, pp. 326-330.
- Groff, E. G. and Faeth, G. M., 1978b, "Steady Metal Combustor as a Closed Thermal Energy Source", *J. Hydronautics*, Vol. 12, pp. 63-70.

Hanson, R. K., 1987, "Combustion Diagnostics: Planar Imaging Techniques," *21st Symp. (Int.) Combust.*, The Combustion Institute, in press.

Herzberg, G., *Atomic Spectra and Atomic Structure*, Dover, 1944

Hughes, T. G., Smith, R. B., and Kiley, D. H., 1983, "Stored Chemical Energy Propulsion Systems for Underwater Applications", *J. Energy*, Vol. 7, pp. 128-133.

Hsu, K.-Y., 1991, *An Experimental Investigation of Wick Combustion of Li and SF<sub>6</sub>*, Ph.D. Dissertation, Department of Mechanical Engineering, The University of Iowa (in preparation).

Hsu, K.-Y. and Chen, L.-D., 1991, "An Experimental Study of Li-SF<sub>6</sub> Wick Combustion and Morphology Analysis of Combustion Products," *AIAA/ASME/SAE/ASEE 27th Joint Propulsion Conference*, AIAA Paper No. 91-2447.

Koch, M. E., Verma, K. K., Bahns, J. T., and Stwalley, W. C., 1983, "Laser-Induced Plasmas in Alkali Metal Vapors," in *Proceedings on the International Conference on Lasers '82*, (R. C. Powell, Ed.), STS Press, McLean, VA, pp. 119-123.

Laurendeau, N. M., 1987, "Temperature Measurements by Light-Scattering Methods," in *Developments in Experimental Techniques in Heat Transfer and Combustion* (R. O. Warrington, Jr., Ed.), ASME HTD-Vol. 71, pp. 45-65.

Lebedev, A. D. and Sokolov, A. S., 1985, "Features of Bubble Ignition and Combustion of Condensed Products," *Combust. Explosion and Shock Wave*, Vol. 21, pp. 393-398.

Lewis, G. N. and Randall, M., 1961, *Thermodynamics*, 2nd E., McGraw-Hill, pp. 242-279.

Loth, E. and Faeth, G. M., 1989, "Structure of Underexpanded Round Air Jets Submerged in Water," *International J. Multiphase Flow*, Vol. 15, No. 4, pp. 589-603.

Lucht, R.P., Sweeney, D.W., and Laurendeau, N.M., 1980, "Balanced Cross-rate Model for Saturated Molecular Fluorescence in Flames Using a Nanosecond Pulse Length Laser," *Appl. Opt.*, Vol. 19, pp.3295-3300.

Lucht, R.P., Laurendeau, N.M., and Sweeney, D.W., 1982, "Temperature Measurement by Two-line Laser-saturated OH Fluorescence in Flames", *Appl. Opt.*, Vol. 21, pp.3729-3735.

Lyu, H.-Y., 1991, "Modeling of Liquid-Metal Wick Diffusion Flames," Ph.D. Dissertation, Department of Mechanical Engineering, The University of Iowa .

Lyu, H.-Y. and Chen, L.-D., 1991, "Numerical Modeling of Buoyant Ethanol-Air Wick Diffusion Flame," *Combustion and Flame* (in review).

Lyu, H.-Y., Chen, L.-D. and Hsu, K.-Y., 1991, "Wick-Type Liquid-Metal Combustion," *AIAA Journal of Propulsion and Power* (in review; a version of this paper is published as AIAA Paper No. 90-2477)

Mahaffy, J. H., 1986, in *The First ONR Workshop on Closed Liquid Metal Combustion*, 19-20 November 1986, University Park, Pennsylvania.

Maksimov, Yu. M., Kirdyashkin, A. I., Merzhanov, A. G., and Raskolenko, L. G., 1984,

"Influence of Ultrasonic Vibrations of the Combustion of Condensed Systems with Solid-Phase Reaction Products," *Combust. Explosion and Shock Wave*, Vol. 20, pp. 669-672.

McBride, B. J. and Zeleznik, F. J., 1984 "Computer Program for Calculation of Complex Chemical Equilibrium Compositions and Applications Supplement I," NASA TM 86885, NASA.

Michel, A., "Thermohydraulic Applications of Liquid Metals in the Non-nuclear Field", in *Thermohydraulics of Liquid Metals*, Lecture Series 1983-07, von Karman Institute, Belgium, 1983.

Okhotskii, V. B., 1984, "Hydrodynamics of Interaction of a Gas Jet and a Liquid," *J. of Engineering Physics*, Vol. 47, pp. 550-558 (pp. 1140-1146, 1985, Plenum Publishing Corp.).

Pan, C.-Z, Bruzzese, R., Solimeno, S., and Velotta, R., 1987, "Interferometric Studies of Nonlinear Relaxation Processes in Vibrationally Highly Excited SF<sub>6</sub> Molecules," *J. Opt. Soc. Am. B*, Vol. 4, pp. 452-461.

Parnell, L. A., 1987, in The Second ONR Workshop on Closed Liquid Metal Combustion, 14-15 October 1987, Pasadena, California.

Parnell, L. A., 1989, "Combustion Instabilities of Submerged Jets in Liquid Metal Fuels," AIAA/SAE/ASME/ASEE 25th Joint Propulsion Conference, July 10-13, 1989, Monterey, California, AIAA Paper No. 89-2825, AIAA.

Parsons, M. L., Smith, B. W., and Bentley, G. E., 1975, *Handbook of Flame Spectroscopy*, Plenum Press, NY, 1975.

Roquemore, W. M., Goss, L. P., Lynn, W. F., and Chen, L.-D., "A Study of the Structure of Jet Diffusion Flames," 1988 *AIAA Aerospace Sciences Meeting*, Reno, Nevada.

Salmon, J.T. and Laurendeau, N.M., 1985, "Analysis of Probe Volume Effects Associated with Laser-saturated Fluorescence Measurements", *Applied Optics*, Vol. 24, pp.1313-1321.

Simpson, M. E. and Chan, C. K., 1982, "Hydrodynamics of a Subsonic Vapor Jet in a Subcooled Liquid", *J. Heat Transfer*, Vol. 104, pp. 271-279.

Stunliger, E., 1964, *Ion Propulsion for Space Flight*, McGraw-Hill, p. 185.

Stwalley, W.C. and Koch, M.E., 1980, "Alkali Metal Vapors: Laser Spectroscopy and Applications", *Opt. Engineering*, Vol. 19, pp. 71-83.

Sukhov, G. S. and Yarin, L. P., 1981, "Combustion of a Jet of Immiscible Fluids", *Combust. Explosion and Shock Wave*, Vol. 17, pp. 146-151.

Surin, V. A., Evchenko, V. N., and Rubin, V. M., 1983, "Propagation of a Gas Jet in a Liquid," *J. of Engineering Physics*, Vol. 45, pp. 542-554 (pp. 1091-1101, 1984, Plenum Publishing Corp.).

Tsuji, H, 1982, "Counterflow Diffusion Flames," *Prog. Energy and Combust Sci.*, Vol. 8, pp. 93-119.

Vargafitik, N. B., Kapitonov, V. M., and Voshchinin, A. A., 1985, "Experimental Study of the Thermal Conductivity of Lithium Vapor," *J. Engineering Physics*, Vol. 49, No. 4, pp. 634-639

(pp. 1208-1212, 1986, Plenum Publishing Corp.).

Verma, K. K., Koch, M. E., and Stwalley, W. C., 1983, "Observation of Levels near Dissociation in the  $X^1\Sigma_g^+$  State of  $^7\text{Li}_2$ ," *J. Chemical Physics*, Vol. 78, Part II, pp. 3614-3622.

Verma, K. K. and Stwalley, W. C., 1981, "Assignment of the  $^7\text{Li}_2$  Optically Transitions Pumped by Ar+ and Kr+ Laser Lines," *J. Applied Physics*, Vol. 52, pp. 3821-3826.

Weimer, J. C., Faeth, G. M., and Olson, D. R., 1973, "Penetration of Vapor Jets in Subcooled Liquids", *AIChE J.*, Vol. 19, pp. 552-558.

Williams, F. A., 1985, *Combustion Theory*, 2nd Ed., Chapter 3, Benjamin/Cummings Publishing Co., pp. 38-91.

You, H-Z. and Faeth, G. M., 1977, "A Reactive-Heat-Pipe for Combined Heat Generation and Transport", Technical Report to DARPA (DARPA Contract No. N00600-74-C-0033), The Pennsylvania State University.